Universiteit Utrecht

NUMERICAL MODELLING OF THERMAL CONVECTION RELATED TO FRACTURE PERMEABILITY: IMPLICATIONS FOR GEOTHERMAL EXPLORATION AND BASIN MODELLING

MSc Thesis

Lindsay Cameron Lipsey

July 21, 2014

Supervised by:

prof. dr. J.D.A.M. van Wees – TNO/Utrecht University

prof. dr. S.A.P.L. Cloetingh – Utrecht University

Student:	Lindsay C. Lipsey
Student number:	3884198
Master's programme	Earth Structure and Dynamics
Utrecht University Supervisor:	prof. dr. S.A.P.L. Cloetingh
TNO Supervisor	prof. dr. J.D.A.M. van Wees
Credits:	60 ECTS
Period of time:	16 September 2013 – 15 July 2014

ABSTRACT

The presence of convective fluid flow can create areas of anomalously high temperatures at shallow depths, which can be exploited for geothermal energy. Previous thermal investigations of the Dutch subsurface revealed a thermal anomaly located at the Luttelgeest 01 Well (LTG-01) in Noordoostpolder, The Netherlands. At depths greater than 4000 m, there is a shift to higher temperatures. Subsequent studies by van Oversteeg (2013) show that the Dinantian carbonates encountered at Luttelgeest contain intervals of relatively high fracture permeability showing potential as a geothermal reservoir for electricity production. Van Oversteeg (2013) constrained the permeability of the 600 m interval of Dinantian carbonates encountered at 4500 m depth to be 60 mD (5.92×10^{-14} m^{-2}). Rayleigh number analysis estimates the minimum permeability for convective onset in the order of 30 mD (2.96×10^{-14} m^{-2}).

The temperature measurements at LTG-01 indicate variations in subsurface temperature that could be indicative of convection. Horner corrected temperatures determined by van Oversteeg (2013) reveals a 12°C temperature change (191 – 203°C) between the top and bottom of the 600 m interval (4550 – 5150 m) and a temperature gradient of 20°C/km across the permeable carbonate layer. This study aims to reproduce the thermal gradient at LTG-01 through three-dimensional numerical models in order to better understand the interplay between natural fracture permeability and temperature patterns. Numerical models of thermal convection are used to illustrate the role of permeability on the timing of convection onset, convection cell structure development and resulting temperature patterns.

Numerical simulations of convection in the Dinantian carbonate platform show that: (1) spacing of convective upwellings can be predicted from aquifer thickness, geothermal gradient, and permeability; (2) convective upwellings can create significant temperature enhancements relative to the conductive profile; (3) the best fit modelled temperature profile occur under the following conditions: a geothermal gradient of 39°C/km, aquifer thickness of 600 m and permeability of 80 mD (7.89×10^{-14} m^{-2}); (4) a pseudo-conductivity, determined for the 600 m convecting interval, is 2.61 W/m/K.

CONTENTS

Abstract 3

Contents 4

1. Introduction 6

1.1 Geothermal energy 6

1.2 Thermal anomalies in the Netherlands 7

1.3 Research objectives and outline 8

2. Theory of thermal convection 9

2.1 Rayleigh number analysis 9

2.2 Onset of convection in porous media 11

2.2.1 Homogeneous porous media 11

2.2.2 Heterogeneous porous media 13

2.2.3 Layered porous media 14

2.3 Onset of convection in a vertical fault zones 14

2.3.1 Convective regimes 15

2.4 Convection pattern development 16

2.5 Summary 18

3. Thermal convection and geology 20

3.1 Permeability in carbonates 20

3.2 Crustal heat transport 21

3.3 Spatial variations of temperature 22

3.3.1 Vertical variations in gradient associated with fluid flow 23

3.3.2 Linking temperature anomalies to geological structures 24

3.4 Geological setting of study area 26

3.4.1 Thermal investigations – evidence for convection 28

4. Methods 31

4.1 Governing equations 31

4.1.1 Fluid properties 31

4.2 Model geometry and boundary conditions 33

4.3 Numerical approach, setup and procedure 34
4.3.1 Rayleigh number analysis 35
4.4 Numerical approach, setup and procedure 35
5. Results 38
5.1 Preliminary tests and 3D models 38
5.1.1 Rayleigh number analysis 38
5.1.2 3D Model results 40
5.2 Scenario 2 – the role of geothermal gradient increase 44
5.2.1 Rayleigh number analysis 44
5.2.2 36°C/km results 45
5.2.3 39°C/km 48
5.3 Scenario 3 – the role of thickness increase 51
5.3.1 Rayleigh number analysis 51
5.3.2 H=900 m 51
5.3.3 H=1200 m 53
5.3.4 Temperature distribution for both H=900 m and H=1200 m 54
5.4 Summary 57
6. Discussion 58
6.1 Summary 58
6.1.1 Effects of permeability 59
6.1.2 Rayleigh number analyses 59
6.1.3 Convection cell structure 60
6.1.4 Temperature patterns 60
6.2 Pseudo conductivity for the permeable layer 65
6.3 Heat flow 66
7. Conclusion 67
Acknowledgements 68
References 69
Appendix I – Symbols used 74

1. INTRODUCTION

1.1 Geothermal energy

In a world where demand for energy is rising and fossil fuels continue to decline rapidly, emphasis is shifting towards the development of renewable energy alternatives. Geothermal energy is an environmentally friendly, sustainable and economical natural source of energy. It is a steady and predictable source of base load heat and energy, not to mention the useable geothermal energy in the earth is nearly unlimited.

The concept of geothermal energy is based on exploiting the natural heat that is found within the earth, which mainly originates from radioactive elements in the earth's crust and the heat from the core. Until recently geothermal energy has been restricted to areas where thermal water or steam is found at relatively shallow depths less than 4km (volcanic areas); however, the advancement of exploitation techniques has broadened the geographic extent of geothermal utilization, whether it be in the form of electricity production or direct heat application (Tester et al., 2007). Geothermal energy can be used directly, i.e. without any further conversion, as heat. Direct use exploits the resource most efficiently; however, heat cannot be transmitted over distances of more than a few kilometres without a notable reduction of efficiency due to heat losses. Alternatively, heat can be converted into electricity generation, but this requires high temperatures that are generally found at depths greater than 5 kilometres. Enhanced geothermal systems (EGS) are targeted at producing electricity from water circulating through high temperature rocks at depths between 3 and 6 km.

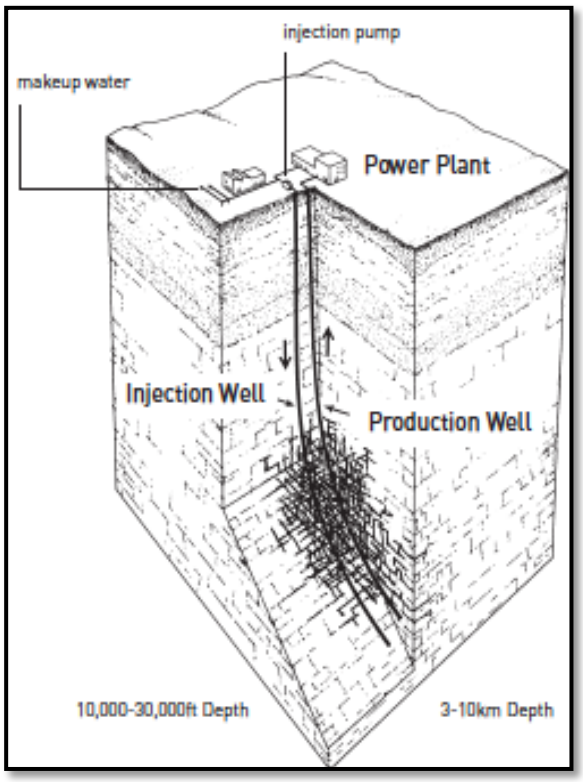

Figure 1.1: Schematic two-well Enhanced Geothermal System in low-permeability crystalline basement

A natural geothermal reservoir generally exhibits the following two physical parameters: (1) hydrothermal fluid at high temperature and (2) sufficient permeability. Shallow geological systems may contain highly permeable layers wherein convection of groundwater in aquifers can create areas of anomalously high temperatures at relatively shallow depths (Sheldon et al., 2014). Thermal convection is an extremely efficient mechanism for the transfer of heat between different geological units in the earth. It can strongly affect the subsurface

temperature field, particularly when convection arises from unstable density variations due to uneven temperature distribution (Dogan, 2013).

Geothermal development comes with numerous economic obstacles that must be addressed. A primary goal of geothermal exploration is to identify areas where higher temperatures are attained at relatively shallow depth as a result of an increased geothermal gradient. Also, naturally fractured reservoirs are a prime target for the development of enhanced geothermal power production in deep sediments and basement rocks. The first step towards identifying favourable regions is to interpolate borehole temperature measurements to create 3D thermal models. Thermal models reveal spatial variations in the geothermal gradient that could be the result of convective fluid flow. However, this requires details on the spatial and temporal variability of convection. Detailed thermal modelling and temperature profiling must be carried out to determine the locations and temporal variability of thermal hot spots.

1.2 Thermal anomalies in the Netherlands

Recent 3D thermal models have been generated for the onshore Netherlands, which reveal a number of thermal anomalies within the Dutch subsurface. Luttelgeest-01 (LTG-01) well is one example of where higher than average temperatures appear at depths greater than 4000m, corresponding to an interval of Dinantian (Carboniferous) carbonates. Three-dimensional thermal modelling where heat transfer was assumed to be controlled by only conduction could not reproduce this temperature anomaly. Even more compelling evidence for convective fluid flow is seen in the 1D temperature profile for LTG-01. The temperature gradient strongly resembles a pattern that has been linked to convective fluid flow (Figure 1.2).

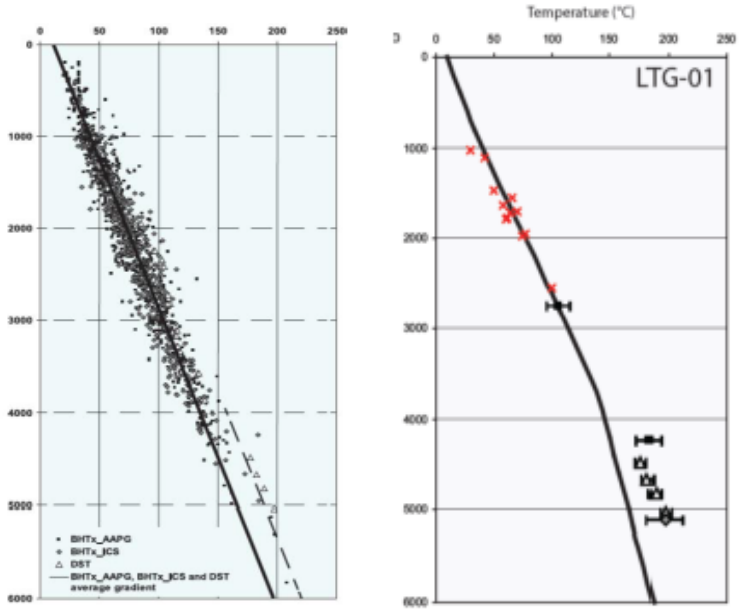

Figure 1.2: (a) The temperature dataset for the Netherlands. The solid line represents the average thermal gradient. **(b)** 1D temperature profile for LTG-01 well. The black line represents modelled temperatures and black squares/red crosses are calibration data. Note the misfit at depths below 4 km (Bonté et al., 2012).

To further investigate, Van Oversteeg (2013) explored whether thermal convection in the carbonate layer could explain the observed LTG-01 thermal anomaly and the local geothermal gradient pattern. Van Oversteeg (2013) used well data from LTG-01 to constrain the natural fracture permeability of the carbonate layer, supplemented with a Rayleigh number analysis to determine the theoretical minimum permeability required for the onset of convection. A 600 m interval showed signs of increased fracture permeability, estimated at 60 mD (5.92×10^{-14} m^{-2}). Rayleigh number analysis constrains the minimum permeability for convective onset at 30 mD (2.96×10^{-14} m^{-2}).

1.3 Research objectives and outline

This study is a first effort to reproduce the thermal gradient at LTG-01 through three-dimensional numerical models in order to better understand the interplay between natural fracture permeability and temperature patterns. The specific features that characterize the LTG-01 anomaly suggest that zones of increased fracture permeability within the Dinantian carbonate layer may host thermal convection. As fluid circulation patterns are largely controlled by the permeability structure, several different permeability structures are tested and the resulting convective patterns assessed.

The work in this thesis focuses on the geothermal potential of deeply buried carbonate layers in the Netherlands. Though a number of different processes can cause non-vertical geothermal heat flow patterns (i.e. lithological heterogeneities or anisotropy in thermal conductivity), this study focuses on the role of fluid circulation in restricted permeable carbonate layers. Numerical models of thermal convection are used to illustrate the role of permeability on the timing of convection onset, convection cell structure development and resulting temperature patterns. Further simulations are carried out where the aquifer thickness and applied geothermal gradient are varied.

This report is divided into chapters, wherein the following questions are addressed:

Chapter 2: *What are the conditions necessary for the onset of convection and how do convective cell patterns develop?*

Chapter 3: *How do deep temperature patterns relate with geological structures and what does this mean in the context of Luttelgeest?*

Chapter 4: *What are the methods used to produce the numerical models in this study?*

Chapter 5: *What information can be determined from the interplay between permeability and thermal anomalies in terms of convective pattern development and the spatial variation of temperature?*

Chapters 6 and 7 provide a discussion and conclusion of results, respectively.

2. THEORY OF THERMAL CONVECTION

There is an extensive amount of literature on density-driven convection. These studies are of fundamental importance, as they identify the factors that affect convective heat transfer in porous media. A thorough review of the relevant literature will provide a framework within which the current problem of this study can be constructed. To that end, literature on convection in homogeneous porous media heated from uniformly from below is reviewed first, followed by that for heterogeneous and layered porous media. Thereafter, studies on convection in vertical fault planes are discussed. When combined, these studies make it possible to identify the factors that are likely to play a role in the present study of thermal convection in deep carbonate layers.

2.1 Rayleigh number analysis

Studies of density-dependent flow in homogeneous unfractured porous media date back almost a century to Lord Rayleigh (1916), who derived mathematical expressions for thermally induced density variations and the onset of free convection. In his scenario, he considered a pure fluid layer heated from below and cooled from above, so that a temperature difference existed between top and bottom boundaries. These conditions yield an adverse linear temperature gradient, which Lord Rayleigh (1916) used to determine the thermal instability criterion for the onset of convection. He introduced a dimensionless indicator, later termed the Rayleigh number, to indicate whether a system is in a diffusive state and stable, or in an unstable state with convection occurring. Accordingly, the Rayleigh number is considered to represent the overall fundamental physical characteristic of the fluid system (Rayleigh, 1916; Zhao, 2006).

Following the procedure introduced by Lord Rayleigh (1916), Horton & Roger (1945) and Lapwood (1948) were the first to quantitatively address the problem of convective instability in the case of a porous medium; hence, it has been termed the Horton-Rogers-Lapwood (HRL) problem (Holzbecher, 1988). The benchmark of the HRL problem considers a homogenous porous layer heated from below, where upper and lower boundaries are considered isothermal and impermeable and horizontal boundaries infinite (Figure 2.1). Cool dense fluid at the top and hot less dense fluid at the bottom causes the system to become gravitationally unstable (Figure 2.1). Natural convection will occur if the buoyant forces driving thermal convection are sufficient enough to overcome the viscous forces inhibiting fluid movement. This is represented by the dimensionless Rayleigh number, which is defined as the ratio of buoyant forces ($\alpha g \Delta T$) upon viscous forces ($\mu\lambda$) in the following formula (Rayleigh, 1916):

$$Ra = \frac{k\alpha\rho_0^2 c_p g H \Delta T}{\mu\lambda} \qquad \textbf{(2.1)}$$

where k is permeability (m^2), α is the volumetric thermal expansion coefficient of the pore fluid (K^{-1}), ρ is the fluid density (kg/m^3), c_p is the specific heat capacity of the pore fluid (J/kg/K), g is gravity (ms^{-2}), H is the thickness of the layer (m), ΔT is the temperature difference between top and bottom of the layer (K), μ is the fluid viscosity (Pa·s), and λ is the effective thermal conductivity of the fluid saturated rock (W/m/K).

Formula 2.1 shows that the Rayleigh number is dependent on the hydrodynamic and thermodynamic properties of the system, but not on the specific boundary conditions. It is linearly proportional to permeability and quadratically proportional to the thickness of the layer (Zhao et al., 2006), suggesting that the permeability and thickness of the layer are the principal factors controlling the onset of convection. This relationship plays an essential role when assessing the conditions that facilitate convective flow (Zhao et al., 2006). Accordingly, the Rayleigh number can be considered an accurate representation of the overall physical characteristic of a given hydrothermal system.

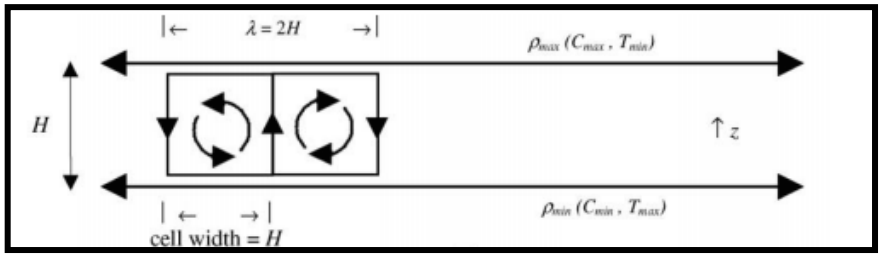

Figure 2.1: The Horton-Rogers-Lapwood problem of an infinite horizontal box, defined by an initial density gradient over layer thickness, H. Convection cells develop of wavelength λ=2H (Weatherill et al., 2004).

Once the Rayleigh number has been calculated, it is necessary to determine its corresponding critical threshold value, above which the system is no longer stable and convective flow occurs. This threshold value, termed the critical Rayleigh number (Ra^*), is dependent on the specific boundary conditions, therefore constraining the conditions that are necessary for the onset of convection. In other words, Ra^* is the minimum Rayleigh number that can trigger convection, thus corresponding to the fundamental convective mode of the hydrothermal system. If known, then the convection pattern development can be predicted for the given system (Holzbecher, 1988; Zhao et al., 2006).

The condition for the onset of convection can be found by the linear instability theory, also known as the principle of exchange of stabilities (Lapwood, 1978). Nield & Bejan (2006) have summarized the conditions for the onset of thermal convection in porous media based on linear stability analysis of the governing equations. The principle is based on the idea that an infinitesimal perturbation of the initial state leads to a state of thermal convection. In a given system (with a specific set of boundary conditions) small perturbations are introduced to the pressure, velocity, and temperature fields. The equations are made dimensionless and then

linearized between initial state and perturbed state. The stable solutions of the linearized equations will give the critical Rayleigh number.

Every critical Rayleigh number has a corresponding convection cell aspect ratio, termed the wavenumber. The wavenumber also depends on the thermal and hydrologic boundary conditions applied to the permeable layer (Simms and Garven, 2004). It can be defined as:

$$a = \frac{\pi H}{L} \quad \textbf{(2.2)}$$

where L is the cell width. The wavenumber can also be defined in terms of the wavelength of convection:

$$a = \frac{2\pi H}{\lambda} \quad \textbf{(2.3)}$$

where λ is the width of two adjacent convection cells. At the onset of convection, as well as for Ra numbers above Ra^*, the critical wave number characterizes the cell width in a homogenous medium (Figure 2.1). Higher values of Ra result in a greater complexity in cell structure. The aspect ratio (length: height) of convection cells in the traditional HRL problem is 1. It is controlled by the critical wave number of the system (Simms and Garven, 2004). If the HRL problem is represented as a rectangular box provided that the length of the box, L, is an integer multiple of the height of the box, H, the aspect ratio, A, can be defined as:

$$A = \frac{L}{H} \quad \textbf{(2.4)}$$

2.2 Onset of convection in porous media

The onset of convection in porous media is discussed in the following sections. Homogeneous porous media is first presented, followed by heterogeneous porous media and layered porous media.

2.2.1 Homogeneous porous media

The Rayleigh number equation shows that convective instability is favoured by large values of ΔT, α, H and ρ_0 and small values of μ and λ. For the case of an infinitely long and homogeneous vertical 2D system with impermeable boundaries of constant temperature and a linear initial thermal gradient across the layer (HRL problem), the critical Rayleigh number is $4\pi^2$ (39.5). The corresponding critical wave number is 1. The aspect ratio, A, must be an even integer if this value is to apply as Ra^*. If A is, in fact, an even integer, then the central vertical plane of an upwelling or downwelling will coincide with a boundary and the critical Rayleigh number is $4\pi^2$. If values of A are not even integers, convection will still occur; however, Ra^* will be some value larger than $4\pi^2$.

When the Rayleigh number exceeds this value, convection is expected to occur within the system. Figure 2.2 shows an example of temperature for the HPL problem for Ra = 39, Ra = 40 and Ra = 200 given a rectangle where the length of the box is 8 times the height (Dausman et al., 2009).

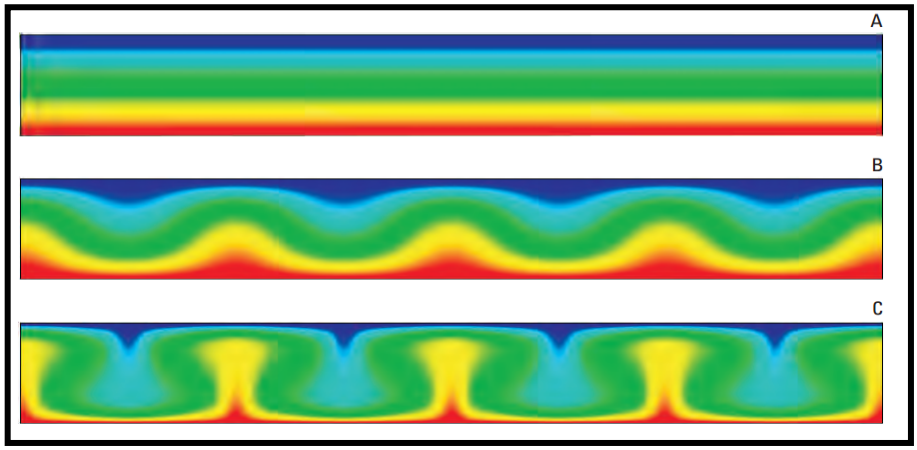

Figure 2.2: Temperature results for the HPL problem. (A) Simulation with Ra = 39 (B) Simulation with Ra = 40. (C) Simulation with Ra = 200. The colours represent 0°C to 100°C (Dausman et al., 2009)

A Ra^* of $4\pi^2$ is only applicable to a problem with impermeable boundaries and fixed temperatures at both top and bottom. If, for example, the top boundary is permeable, the corresponding critical Rayleigh number is reduced to 27.1. Convection in this instance occurs easier than the same system with an impermeable top boundary. To put this into a geological context, for a permeable sandstone aquifer within a sedimentary basin that is embedded in impermeable shale, the critical Rayleigh number is $4\pi^2$ (or approximately 39), which corresponds to an aquifer thickness of 330m with permeability of 1 Darcy under a geothermal gradient of 30°C/km (Souche et al., 2014).

Convection will only occur in a porous medium if the temperature difference between the upper and lower boundaries is sufficiently high. Large aquifer thickness also facilitates the occurrence of convection. Table 2.1 lists the wavenumber and critical Rayleigh number for different boundary conditions.

Table 2.1: Wavenumber and critical Rayleigh number for different boundary conditions (Holzbecher, 1998).

Top surface	Bottom Surface	Wave Number	Ra^*
Fixed temperature Impermeable	Fixed temperature Impermeable	π	39.5 ($4\pi^2$)
Fixed temperature Permeable	Fixed temperature Impermeable	2.30	27.1
Fixed temperature Impermeable	Non-fixed temperature Impermeable	2.30	27.1
Fixed temperature Permeable	Non-fixed temperature Impermeable	1.75	27.1

Lapwood (1978) investigated the effect of conducting vertical boundaries on the critical Rayleigh number, cell pattern development and critical wave number. The aim was to emphasize fracture and fault like geometries by adjusting one box dimension. A change in the box dimensions results in significantly different Ra^* and convective cell structure. Large box dimensions induce negligible wall conditions, therefore Ra^* approaches the value for the HRL case ($4\pi^2$). If the conducting walls are far apart, three-dimensional motion is preferred over two dimensional at convection onset. Furthermore, Lapwood (1978) shows that for fracture/fault systems, the critical Rayleigh number is several orders of magnitudes greater than $4\pi^2$, and the cells take the form of rolls with axis parallel to the long horizontal dimension of the box.

2.2.2 Heterogeneous porous media

Geological systems are often complex and display a high degree of heterogeneity. Fractured porous media are commonly found in many hydrogeological systems, with heterogeneity occurring across many spatial and temporal scales (Holzbecher, 1998). The onset of instability in such an environment is controlled by the local conditions and is generally characterized by large amplitude thermal perturbations and unsteady flows. Predicting an accurate critical Rayleigh number for a heterogeneous porous medium becomes problematic. If an average Rayleigh number is applied, it removes structural controls that are important in governing the onset and growth of convective instability (Zhao et al., 2003).

Sharp et al. (2014) conclude that permeability heterogeneity controls the onset and development of free convection and instabilities and the onset is sensitive to the boundary conditions. Critical Rayleigh numbers are strongly dependent on anisotropy of permeability. If a system is characterized by horizontal heterogeneity, a larger temperature gradient is required for the onset of convection, especially as the permeability contrast increases. If a thin permeable layer impedes a homogeneous medium, there is a sudden transition from square flow cells to a flow pattern with strong flow taking place up/down in the permeable fault. Narrower faults necessitate greater permeability contrasts for this transition to occur.

In porous media with anisotropic permeability, McKibbin (1986) has performed linear stability analysis incorporating an anisotropy ratio (ξ) defined as:

$$\xi = \frac{\kappa^v}{\kappa^h} \qquad \textbf{(2.5)}$$

where $\kappa^v$and κ^h are the vertical and horizontal permeability, respectively. The vertical permeability is generally much smaller than the horizontal permeability in geological porous media. By increasing ξ, the vertical permeability decreases slightly, while the horizontal permeability must increase greatly (McKibbin, 1986).

2.2.3 Layered porous media

Convection in layered porous media has been widely studied. McKibbin (1980) considered a multi-layered system with isothermal and impermeable lower and upper boundaries. His results show that significant permeability differences within the layered system are required for convection to occur. With increasing permeability contrasts, the system shifts from system-wide convection to localized convection confined to a few layers.

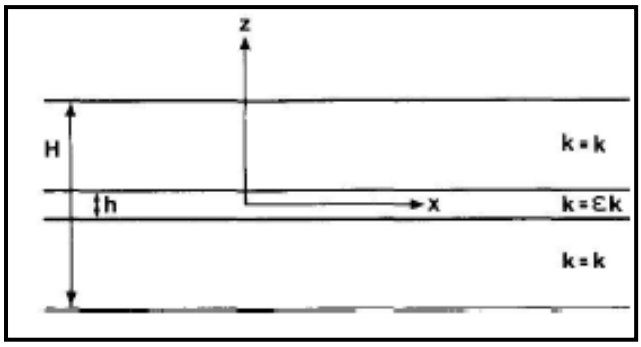

Figure 2.3: Model setup for convection with a low permeability sublayer present (3 layer model) (Bjørlykke et al., 1988).

Large permeability differences between individual layers may exist. Bjørlykke et al. (1988) investigated the effect of impeding low permeability sub layers on the presence of local convection within higher permeability layers. In their 3-layer model, the central layer has a contrasting permeability with respect to the layers above and below (Figure 2.3). Results show that significant permeability differences and thick layers are necessary to cause a system to shift to layered convection. The critical Rayleigh number increases when a low permeability layer is introduced into the system. A transition to local convection will not occur when the layers are very thin and have low permeability, and when there is a gradual change in the permeability.

2.3 Onset of convection in a vertical fault zones

Up until this point, discussion has been limited to homogeneous porous media, wherein the horizontal layer is assumed to extend beyond the frame of reference thus making vertical wall boundary conditions irrelevant. What happens if vertical boundary conditions are applied in such a way that it represents a vertical fault?

Murphy (1979) was the first to consider the onset of convection in a vertical fault plane. His model considers a vertical fault or fracture of porous material that is imbedded in impermeable rock extending infinitely in the horizontal direction. The surrounding impermeable rock is considered a conductive medium imposing a constant vertical temperature gradient along the fault or fracture boundary. In this situation, two heat

transport processes are occurring simultaneously. Geometry and reference system used for modelling is shown in Figure 2.4. As it will soon be shown, the added heat transfer between fracture/fault and surrounding rock will affect considerably affect the linear stability analysis and thus, the conditions required for the onset of convection (Murphy, 1979; Tournier et al., 2000).

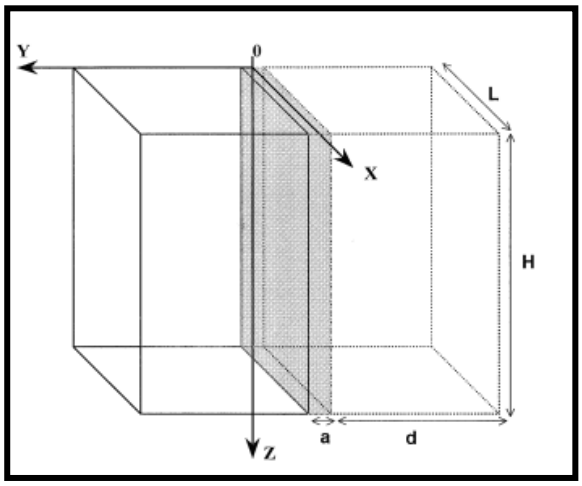

Figure 2.4: Geometry and reference system used for modelling in Murphy (1979) and Tournier et al. (2000). The fault is located in the middle represented by the grey

The low thickness-to-height aspect ratio of the fault/fracture suggests that conductive lateral heat transfer may have a dominating effect, whereby causing the lateral thermal gradients to supersede the vertical gradients. To assess this problem, Murphy (1979) introduced a modified Rayleigh number scaled by fracture aperture (as opposed to height), which can be used to characterize convection in thin vertical fractures:

$$R^* = \frac{Ra^2}{H^2} \qquad \textbf{(2.6)}$$

Murphy (1979) found that the critical Rayleigh number for the conditions in his model greatly exceed $4\pi^2$ (value for HPL problem). In fact, a 1-meter wide and 100 meter high fracture zone has a critical Rayleigh number of 10^5, because of the heat transfer between the fracture and the surrounding rock. His models show the proportionality between strength of convective flow and Rayleigh number. Conditions above the critical value of $4\pi^2$ drive the convection pattern from stable to unstable, with a more complicated spatial and temporal behaviour. In constant permeability models, Bächler et al. (2003) show that the onset of convection within a fault needed fault permeability greater than $5x10^{-13}$.

2.3.1 Convective regimes

The onset of convection occurs at different fault permeability for different fault heights and widths. Tournier et al. (2000) investigate the conditions necessary for the development of

density-driven convection in a thin fault by assessing various initial temperature distributions in the fractured medium. The same reference system is used as show in Figure 2.3. Top and bottom temperature boundaries remain fixed, which focuses the heat exchange to occur perpendicular to the fracture plane. Additionally, no flow conditions are imposed on the fracture boundaries.

Both Murphy (1979) and Tournier et al. (2000) show that variations of the perturbation amplitude and initial conditions results in the development of three convective domains: (1) spontaneous convection, (2) delayed convection and (3) conduction. For the case of spontaneous convection, it is found that for thin fractures a minimum wavenumber occurs broadly near m = 7, which corresponds to vertically elongated convective cells of aspect ratio 7. For wider fractures, the minimum is towards that for an infinite horizontal porous medium, with a sharp minimum around $4\pi^2$ and thus, aspect ratio 1 (m = 1). The varying characteristics are due to a change in heat transfer mode of the system. Heat is exchanged during horizontal flow at the top and bottom boundaries in the case of an infinite horizontal porous medium, where a/H = ∞. This corresponds to the fastest growth convective mode. For thin fractures where a/H << 1, the main heat transfer occurs between fracture wall and surrounding rock, resulting in shower-wavelength modes.

For delayed convection domain, the shape of the initial perturbing thermal field controls the behaviour of the thermal instability. Initially, heat escapes from the fracture towards the wall causing the perturbation to decrease. Progressive smoothing of the thermal field across the fracture by conduction causes a blanketing effect of the fracture zone to occur, resulting in a delayed onset of convection. Eventually this allows for the perturbation to increase again after the delay (Murphy, 1979). Tournier et al. (2000) find that the critical Rayleigh number for delayed onset of convection is approximately 10-20 percent of that for spontaneous onset of convection (both cases the value larger than $4\pi^2$). At reservoir scale, convective circulations in individual fractures will experience thermal coupling after a time delay of d^2/k, where d is the distance between fractures and k is the thermal diffusivity.

2.4 Convection pattern development

As discussed in the previous sections, convection begins at some threshold value Ra^*, below which convection flow does not occur, and heat is purely transmitted by conduction through the fluid. This is the case whether there is a homogeneous medium or vertical fault plane in the system. Given the presence of horizontal boundaries and no specific initial conditions imposed, the first spatial pattern above R^* is in the form of a stationary system of parallel rolls. The velocity field of the convection rolls is nearly two-dimensional.

While two-dimensional studies of convection in a rectangle box reveal oscillatory convection, the three-dimensional case reveals the development of different structures with time. The final structural form is dependent on the initial conditions. When Ra is above Ra*, a stable free convection pattern results. The following two types of plan form are mostly found:

1. Two-dimensional rolls: A relatively simple pattern, in which all amounts depend on one of the horizontal directions. Cells are infinitely elongated in the form of rolls. They have a pattern given the function:

$$\mathrm{w(x)} = \cos\ \mathbf{kx} \tag{2.7}$$

2. Hexagonal cells: wave vectors have the same modulus k, directed at angle of 2π/3 to one another. Hexagons are favoured in conditions with significant asymmetry, which could be due to variations in system properties, different boundary conditions, etc.

While the instability of disturbances for the onset of convection is characterised by a particular wavenumber, the pattern of convection cells is unspecified. Through numerical experiments, distinctive convective patterns can be obtained at a given Rayleigh number where box size differs or where initial stable regime differs (Zhao et al., 2004; Tournier et al., 2000; Garibaldi et al., 2010). Holzbecher (1998) provides a comprehensive overview of convection pattern development. Assuming perturbation variables, $\Psi^*$and θ^*, and a system of infinite length, steady state cells are assumed to have the form:

$$\Psi^* = \Psi_0\ \sin\left(\frac{r\pi x}{L}\right)\sin(\mathrm{s\pi z}) \tag{2.8}$$

$$\theta^* = \theta_0 \cos(\frac{r\pi x}{L})\sin(\mathrm{s\pi z}) \tag{2.9}$$

where Ψ_0 and θ^* are the amplitudes of the mode characterized by the numbers r and s. The number of cells in the horizontal direction with length L is r, and the number of layers of convection cells is s. Therefore, the aspect ratio is denoted by:

$$\vartheta = \frac{H}{s}\frac{\mathrm{r}}{L} \tag{2.10}$$

Steady state solutions yield two linear solutions, which gives a relationship between Ra, s and r (assuming the determinant condition that there are nonzero solutions (Ψ_0 , θ^*):

$$\pi^4\left[s^2 + \left(\frac{r^2}{L^2}\right)\right]^2 - \frac{Ra(r\pi)^2}{L^2} = 0 \tag{2.11}$$

Therefore, the critical Rayleigh number for the values r and s for a given L can be defined as:

$$Ra_{crit}^{r,s} = \left\{\frac{\pi L}{r}\left[s^2 + \left(\frac{r}{L}\right)^2\right]\right\}^2 \tag{2.12}$$

For the case of a homogeneous porous layer with infinite length (critical Ra = $4\pi^2$), which also

corresponds to the lowest critical value (s=1=r/L), it can be expected that there will be one layer of rolls, and if the length of the box is a multiple of the height, the cells will be quadratic. The ratio of r/L will be different for all values of r and s, with the lowest critical Rayleigh number being slightly higher than $4\pi^2$ (for example, when L>H but no a multiple of H).

As stated before, Ra^* is dependent on the physical properties of the porous medium and the types of thermal and hydrologic boundary conditions applied to the medium. The critical Rayleigh number controls the convection cell pattern that will form in the given situation/environment. Based on the linear stability theory discussed above, Table 2.2 lists critical values considering a system with H=1 and L=2.

Table 2.2: Critical values for a system with H=1 and L=2 (Holzbecher, 1998).

No of cells	2	3	4	5	6
Aspect ratio	1	1.5	2	2.5	3
Critical Ra	39.5	46	62	83	110

Garibaldi et al. (2010) show that permeable zones of constant permeability results in single convective cells of small width/height ratios. If a depth-dependent permeability is introduced, the Rayleigh number is now different from top and bottom and stable convective wavelengths must adapt to the local representative permeability. For horizontal layers, the presence of anisotropy affects both the critical Rayleigh number and the critical wavenumber. However, it does not lead to new flow patterns at the onset of convection.

2.5 Summary

To summarize, when $Ra < Ra^*$, there is no convection. For $Ra > Ra^*$, but not too large, a regular structure of convection rolls forms, with hot fluid rising and cold fluid falling (Figure 2.5). A bifurcation diagram shows the stable states of convection for various Ra/Ra* combinations. Imagine placing a probe that measures the vertical component of velocity somewhere in the box midway between the top and bottom boundaries. A plot of v(Ra) looks like that shown in Figure 2.6. The stable states are in bold, while the unstable states are dashes. Since we cannot predict whether the velocity will be up or down, it is termed symmetry breaking (Holzbecher, 1998).

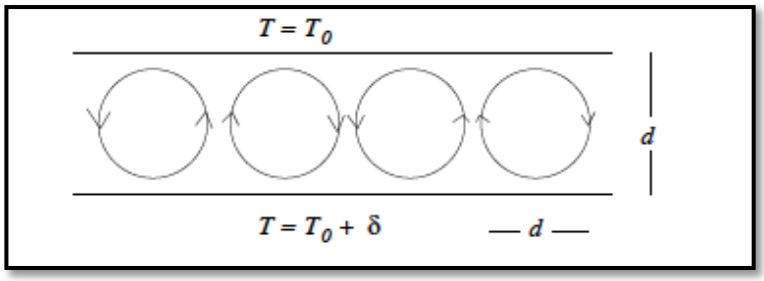

Figure 2.5: Convection rolls resulting from Ra > Ra*. Note that the system Ra is only slightly larger than Ra*.

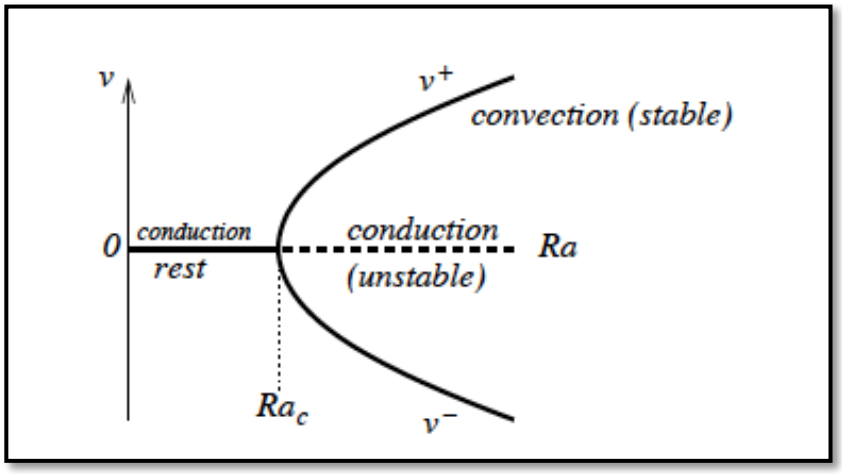

Figure 2.6: Bifurcation diagram showing the stable states of convection for Ra/Ra* combinations (Holzbecher, 1998).

3. THERMAL CONVECTION AND GEOLOGY

The economic viability of geothermal applications depends primarily on the depth at which the required temperature is attained, as greater depths mean higher drilling costs. Therefore, geothermal exploration aims at identifying areas where anomalously high temperatures occur at relatively shallow depths. Temperature measurements from boreholes provide the first step in understanding the temperature distribution in the subsurface. In addition, an understanding of the mechanisms of heat transport in the subsurface is required. This chapter provides an overview of permeability in carbonates, crustal heat transport and finally spatial variations of temperature.

3.1 Permeability in carbonates

Permeability (k) is a critical parameter in geothermal reservoir characterization, as it plays a fundamental role in heat and mass transfer. Permeability is defined as the capacity of a certain [geological] medium to transmit fluid. It is expressed as either m^2 (SI unit) or in units of Darcy, where 1 Darcy is equal to 10^{-12} m^2 (Saar, 2011). In this study, permeability values are always given in both unit forms.

Permeability is directly related to two rock properties: (1) intrinsic permeability and (2) fracture permeability. Porosity, defined as the ratio of pore volume to total volume, is directly correlated to the intrinsic permeability, which is the measure of the fluid flow through the existing pore network of the rock. The second property, fracture permeability, relates to the discontinuities present within the rock along which fluid circulation can occur (Saar, 2011).

Geologic materials exhibit a wide range of permeabilities between 10^{-21} and 10^{-7} m^2. Geothermal reservoirs are characterized by large permeability, which many have suggested to be higher than 10^{-13} m^2. Nevertheless, several studies suggest that minimum permeabilities between $5x10^{-17}$ to 10^{-14} m^2 are required to observe convective fluid flow and heat transfer, and reservoirs with a lower permeability are thereby largely dominated by heat conduction.

Permeability exhibits great variation within geologic media; therefore, it is necessary to understand the geometry of the geologic layers and their physical parameters, which affects the permeability. For example, permeability decreases with increasing depth (pressure) or effective stress. For carbonate rocks, the permeability structure is transient, heterogeneous and anisotropic in nature. Primary porosity is low, especially in fine-grained carbonate rocks. Fracturing and successive dissolution enhances permeability. Competing mechanisms such a secondary dissolution and precipitation processes will dominate faults cutting through carbonate rocks, therefore continuously altering the permeability structure (Sharp et al., 2009).

3.2 Crustal heat transport

Heat transport in the earth is governed by three mechanisms: conduction, radiation and convection. In the shallow lithosphere, heat transfer is generally dominated by conduction, which is a diffusive process in which molecules pass on their kinetic energy to other molecules (Turcotte and Schubert, 2002).

The geothermal gradient is the rate of increase in temperature per unit depth. In a purely conductive environment where there is no lateral variation in thermal conductivity, no radiogenic heat production, then the vertical temperature gradient can be calculated using Fourier's law. Fourier's law of heat conduction states that the thermal conductivity (λ) is a constant of proportionality between heat-flow (q) and the temperature gradient (dT/dz):

$$q = -\lambda \frac{dT}{dz} \qquad \textbf{(3.1)}$$

where q is considered the amount of heat flow through a unit area per unit time (Wm^{-2}) and λ is expressed in W/m/K. The minus sign is an indicator that the flow of heat occurs from high to low temperatures. Note that equation 3.1 is based on the assumption that radiogenic heat does not affect the temperature distribution with depth, as calculations show that the error is negligible for depth intervals of several hundred meters.

Crustal geothermal gradients are strongly affected by basal heat flow, which has a positive effect on temperature values, while thermal conductivity has a negative effect on temperature (van Oversteeg, 2013). In general, topographic relief, climatic changes, or sedimentation and uplift can affect the temperature gradient in a given region (Saar, 2011; Guillou-Frottier et al., 2013). Anisotropy and heterogeneity in thermal conductivity between rock layers can also cause non-linear geothermal heat patterns. Heterogeneity causes the temperature gradient to refract at boundaries separating different thermal conductivities. In Figure 3.1 four possible causes for shallow thermal anomalies are shown and their effect on the geothermal gradient.

If the rock hydraulic permeability is sufficiently large, convection driven heat transfer may occur. Fluid flow is mainly driven by the natural thermal gradient that exists within the earth. The subsurface temperature field is highly sensitive to fluid density instabilities that arise from uneven temperature or salinity distributions. As density driven convective flow develops, the temperature field is further perturbed. Figure 3.2 shows the temperature profiles indicative of a convective system.

Finally, it is important to remember that measured temperature gradients represent a snapshot in time. In reality, geotherms are transient in nature. The existence of transient processes, such as heat-transfer processes, occur over long time scales.

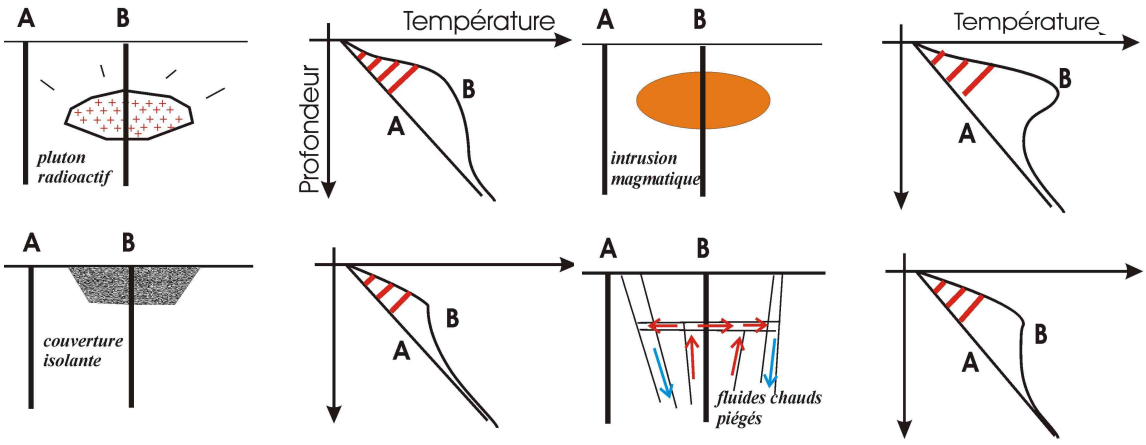

Figure 3.1: The temperature gradient shape reflecting four different cases: (a) high heat producing granite, (b) insulating cover, (c) magma reservoir and (d) hot fluids at shallow depths.

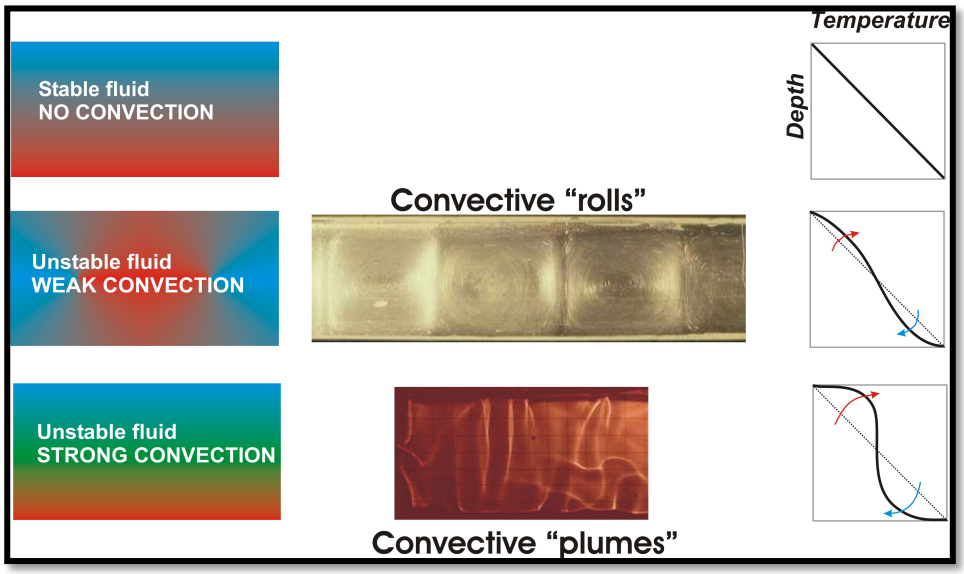

Figure 3.2: Laboratory experiments by Guillou-Frottier and Jaupart, 1995.

3.3 Spatial variations of temperature

Temperature-depth measurements are a commonly used tool in geothermal exploration. Interpretations are primarily made based on the assumption that conductive heat transport is occurring, and that temperatures increase linearly with depth. However, temperature-depth profiles don't always show this characteristic pattern, as seen in the previous section. Temperatures may decrease or remain isothermal with increasing depth, and at great depth, the geothermal gradient may revert back to positive causing temperatures to increase with depth. Distinguishing between these temperature-depth patterns and temperature inversions is key when determining the fluid flow and thermal structure within a given region.

Furthermore, though the critical Rayleigh number can shed light on potential theoretical convection patterns for a system with a given set of boundary conditions, it provides no constraint on the spatial or temporal variability of convective fluid flow itself. In fact, the varying nature of fluid and rock properties in natural systems limits the applicability of Rayleigh number analyses. Convection shows considerable spatial variability, which poses as a major problem in geothermal related applications, one that remains the center of many studies. Many turn to detailed thermal and convection modelling in order to understand better both the spatial and temporal variability of positive and negative thermal anomalies within the Earth's crust.

3.3.1 Vertical variations in gradient associated with fluid flow

Owing to oil and gas exploration, the accessibility of subsurface temperature data has facilitated in our understanding of deep temperature patterns. Temperature dataset analyses in Europe have revealed significant thermal anomalies located in graben systems and sedimentary basins, which have been linked to convective fluid flow and neighbouring brittle deformational structures. In fact, several studies have demonstrated that geothermal anomalies in sedimentary basins are strongly controlled by fluid flow in permeable layers (Pasquale et al., 2013; Guillou-Frottier et al., 2013, Garibaldi et al., 2010). The study of groundwater circulation has revealed that convective fluid flow leaves a distinct pattern on the local geothermal gradient.

In the Po Plain, Italy, Pasquale et al. (2013) argue that the deep aquifer in the carbonate may host thermal convection, which would explain the observed low geothermal gradient within the deep carbonate layer and the higher gradient in the overlying layers. Pasquale et al. (2013) investigated the thermal regime of sedimentary sequences in the eastern region of the Po Plain in Italy, during which a deep carbonate layer with an unusually low thermal gradient (14°C/km) was discovered (Figure 3.3a). In the low-permeability overlying layers, a much larger gradient of 53°C/km is present. This particular thermal signature is thought to be characteristic of convective processes that are occurring within the carbonate layer. They quantified the potential for thermal convection to take place within the carbonate layers by performing Rayleigh number analyses. They present a formula that can be used to calculate the minimum thermal gradient that is required for convection to occur. This is mostly based on the permeability and thickness of the layer (Figure 3.3b).

This unique pattern on the temperature gradient is also observed at Soultz geothermal site in the Upper Rhine Graben. A low geothermal gradient characterizes the interval from 1500 – 4000m, which is believed to be the direct result of hydrothermal convection along faults in the horst and graben system (Baillieux et al., 2013; Guillou-Frottier et al., 2013). This thermal signature appears in many localities where a layer of increased permeability, possibly due to the presence of faults and fracture networks, is linked to fluid flow.

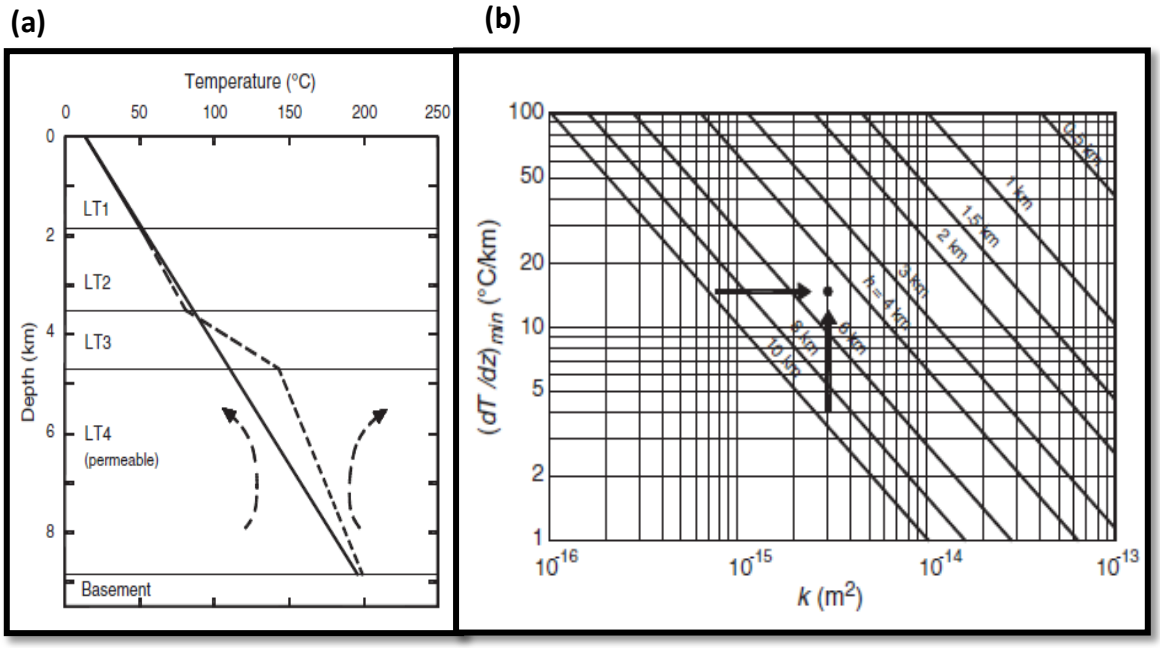

Figure 3.3: (a) Temperature vs. depth inferred from thermal gradient estimated by extrapolating the regional thermal gradient. Arrows indicate likely thermal convection (b) Thermal gradient as a function of the permeability (k) and thickness (h) of the carbonate unit found in the Po Plain, Italy (Pasquale et al., 2013).

3.3.2 Linking temperature anomalies to geological structures

The identified thermal anomalies in Europe have been the center of widespread studies. Several different approaches and techniques have been implemented in studies, most of which aim to link local structural features with thermal convection in order to explain the observed deep temperature variations (Guillou-Frottier et al., 2013). Petrophysical properties obtained from boreholes have been used to compare theoretical and measured temperature gradients in regions where fluid flow could be localized in fault zones (Haffen et al., 2013; Siffert et al., 2013). The role of depth-dependent permeability on convective fluid flow patterns in permeable fault zones has been intensely investigated within the Provence basin (Garibaldi et al., 2010) as well as the Upper Rhine Graben (Guillou-Frottier et al., 2013). Both reservoir and basin scale numerical modelling are used to address signature thermal features that have been linked to convective fluid flow as deep as 5km.

Bächler et al. (2003) studied the Landau geothermal anomaly that coincides with two predominant faults of high permeability. Temperature data for the region shows temperature undulations at 1km depth, with temperature anomalies close to 12°C. They were able to reproduce these thermal anomalies by using transient 3D numerical models. Following a similar approach, Garibaldi et al. (2010) attempt to link the Vistrenque graben thermal anomaly to the numerous faults that are associated with the Nimes fault, producing a hydraulic conductive system. They argue that fluid circulation is enhanced by the presence of the permeable fault system, which is dependent on the fracture aperture and stress

regime. Garibaldi et al. (2010) considered a depth-dependent permeability for both the host rock and fault zone. They were able to produce thermal anomalies of more than 10°C, given a sufficiently wide and permeable fault zone (Figure 3.4). The incorporation of depth dependent permeability resulted in the juxtaposition of several layers of convective cells. The implications this has on the spatial variation of high permeability zones within a fault zone means that neighbouring convective cells may control each other, favouring spatial variation in thermal anomalies when considering depth-dependent permeability. When host rock permeability is low, overlying layers of convective cells (alternation of thermal ups and downs) are favoured (Garibaldi et al., 2010).

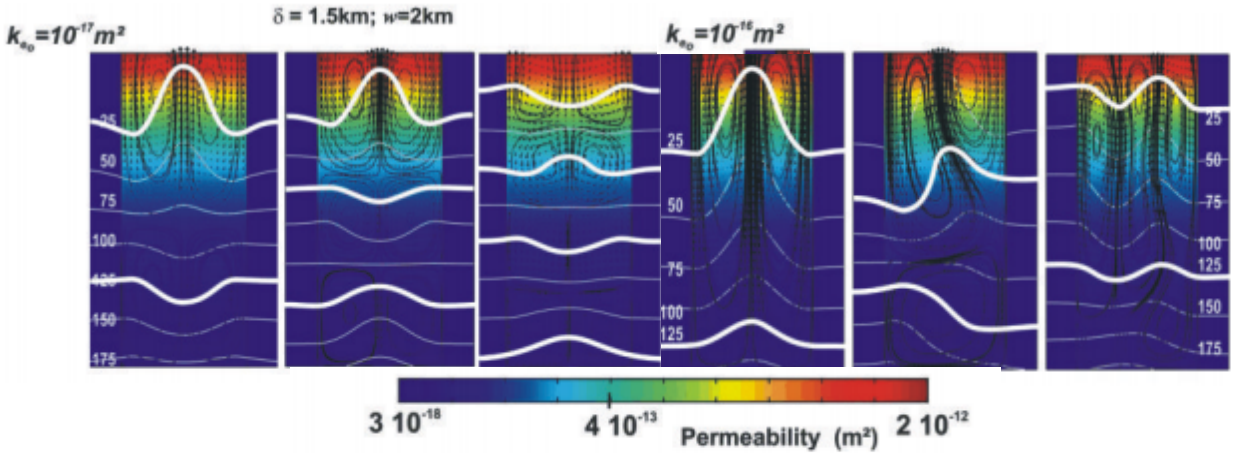

Figure 3.4: A 2km wide permeable zone with depth-dependent permeability (δ = 1.5km). The first three figures have host rock permeability at the surface of $10^{-17}m^2$, and the second three figures have host rock permeability at the surface of $10^{-16}m^2$. Lateral temperature differences of 10°C are observed (Garibaldi et al., 2010).

For the Upper Rhine Graben, Guillou-Frottier et al. (2013) also investigates the role of depth-dependent permeability on the structure of hydrothermal convection (Figure 3.5). They find that the thickest zones of permeable fractured layers preferentially host thermal anomalies. Moreover, depth dependent permeability, the inclination of the interface between permeable and impermeable layers and fixed heat flow at the base can reproduce the presence of only a few dominant upwellings where the Soultz temperature anomaly is located. A similar temperature-depth profile is reproduced by considering a fault permeability of 10^{-14} m^2.

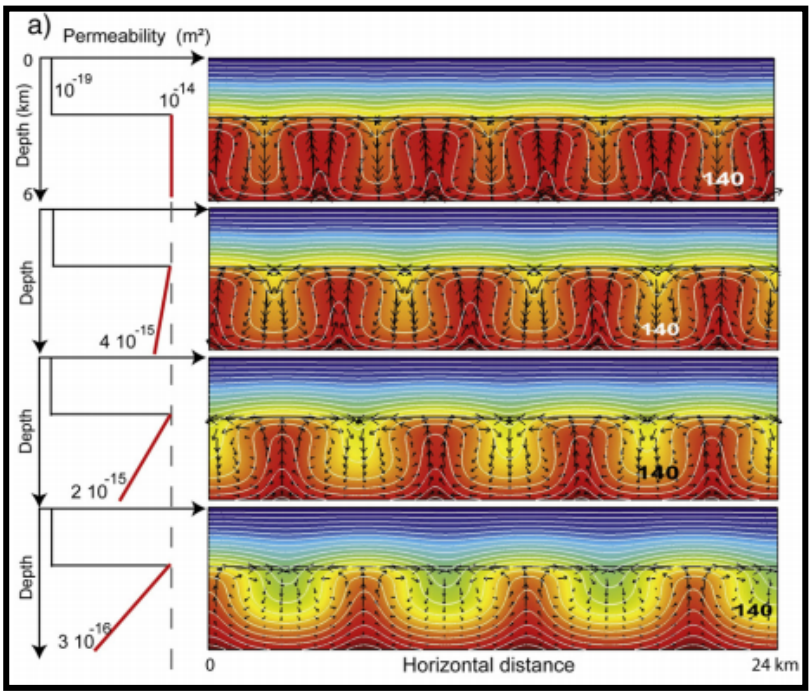

Figure 3.5: Effect of depth-decrease of permeability on convective patterns. The permeability decrease is intensified from top to bottom. Isotherms are separated by 10°C (white lines) (Guillou-Frottier et al., 2013).

3.4 Geological setting of study area

Though the Netherlands has more than 5000 oil and gas wells, relatively few studies have focused below the first two to three kilometres, because it is below the major petroleum target for the country (van Hulten, 2012). Deposition during the Carboniferous is poorly constrained due to the lack of wells that have penetrated the Mississippian or Devonian formations. Generally, detailed information from the UK and Belgium is used to determine the sedimentological setting of the Carboniferous.

Recently in 2004 a new well, Luttelgeest-01 (LTG-01), was drilled providing information on the existence of a Mississippian carbonate platform at the top of the Devonian. The LTG-01 well is located in Noordoostpolder in the north central region of the Netherlands. During the Carboniferous, the northern Netherlands was part of the North West European Carboniferous Basin (NWECB) (van Oversteeg et al., 2014). It strikes east-to-west and extends from present day Poland to Great Britain (Kombrink et al., 2008). The basin formed during the Devonian at the end of the Caledonian triple continental plate collision. At this time, extension caused a WNW-ESE trending fault bounded half graben to form, which is believed to have played a key role on Carboniferous sedimentation. Carbonate platforms developed on structural highs during the Dinantian period, while shales filled the basins (van Hulten, 2012).

The Luttelgeest Well is located on the Texel-Ijsselmeer structural high, which is a NW-SE striking tilted fault block. Its southern boundary is characterized by a steep fault system, and to the north the structural high gradually moves into the Friesland platform (van Oversteeg et al., 2014). At LTG-01, Cenozoic, Mesozoic and Paleozoic sediments are found, which overly a poorly known Caledonian basement. Large erosional periods took place during the Jurassic

and Early Cretaceous, represented by major unconformities (Kombrink et al., 2010) (Figure 3.6).

Little is known about the Dinantian carbonates, as the majority of carbonate platforms are found at great depth in the Netherlands. Several interpretations have been made of the paleogeography, most recently by Van Hulten (2012), who includes recent well data from Uithuizermeden-02 and Luttelgeest-01 and new seismic data. In his interpretation, several 10km reef trends extend over large parts of the north (Van Oversteeg et al., 2014). Luttelgeest, in particular has a horizontal extent of 18km, which includes both the platform and slope. The Luttelgeest-01 Well is located at the southern end of a N-S trending carbonate platform. Dinantian limestone deposits are encountered from 4335 to 5123.5 meters in the well. In figure 3.7, the Dinantian carbonate build-up can be clearly seen.

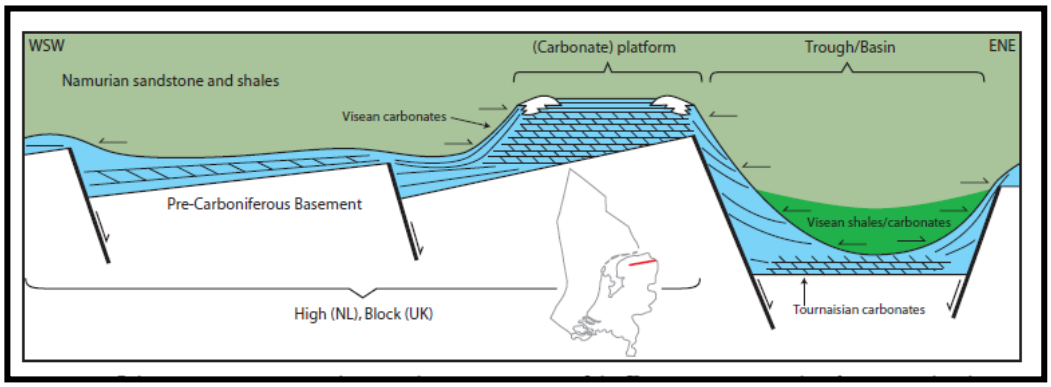

Figure 3.6: Schematic cross section along a Dinantian carbonate build-up in the Dutch onshore (Kombrink, 2010).

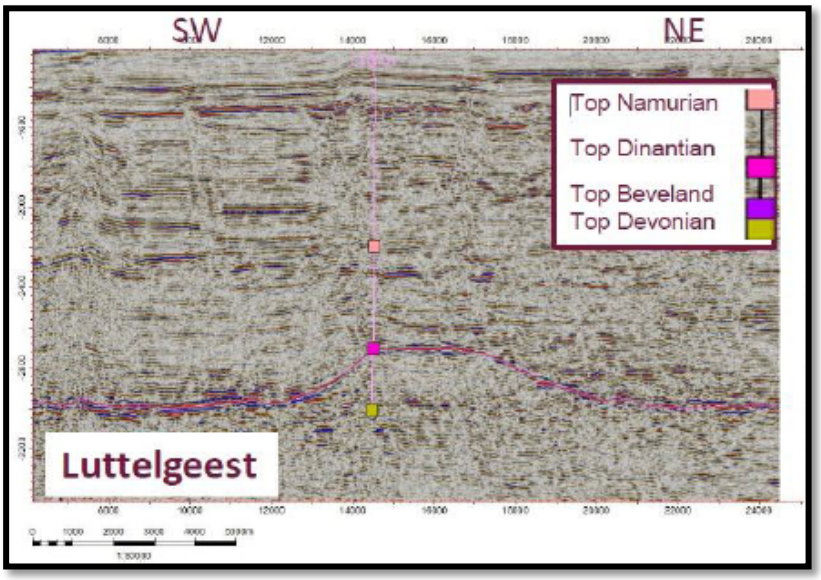

Figure 3.7: Seismic interpretation of the Dinantian carbonate build-up at LTG-01 (EBN, 2013).

The platform dimensions are compared with internationally known examples in Figure 3.8, along with the vertical dimensions of the same reefs.

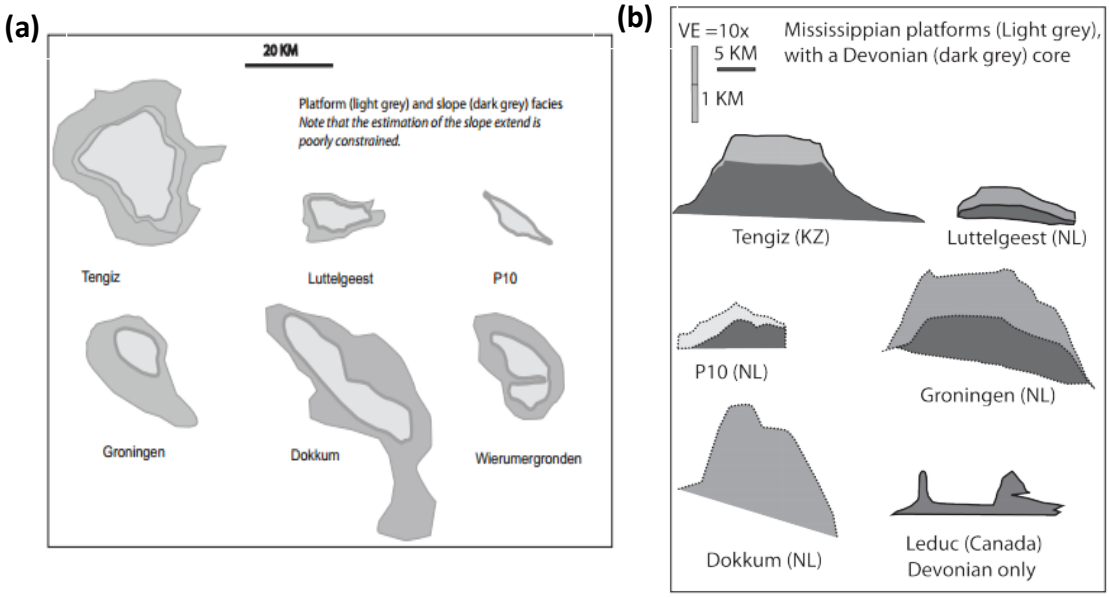

Figure 3.8: (a) Horizontal dimensions of the reefs in the Netherlands and Tengiz, including that found at Luttelgeest (b) Vertical dimensions of the same reefs shown in (a) (van Hulten, 2012).

3.4.1 Thermal investigations – evidence for convection

Analysis of bottom-hole temperature (BHT) data obtained in wells drilled mostly for hydrocarbon exploration has been the main informational source, and has revealed a number of deep thermal perturbations, potentially induced by fluid flow. However, with depth comes an increase in geological uncertainties, making it more challenging to model fluid flow. Temperature measurements from boreholes can be used to estimate the average vertical temperature gradient at its location, providing insight on the local spatial variation in temperature.

Bonté et al. (2012) were unable to reproduce the anomaly in 3D thermal models of the onshore Netherlands, which incorporated the effects of variations in thermal conductivity and radiogenic heat production, as well as the effects of vertical tectonic motions. The LTG-01 temperature-depth profile resulting from thermal modelling reveals two noteworthy occurrences: (1) the existence of two distinguishable gradient deviations that can be attributed to lithological heterogeneities occurring at 1700m and 3700m, which roughly corresponds to the upper layer of the Carboniferous characterized by a low conductivity interval of shale associated with coal, and (2) anomalously high temperatures at depths greater than 4000 m. At Luttelgeest, the temperature gradient from 0 to 1700 m is 31°C/km,

the average for the Netherlands. From 1800 m to 3700 m, the gradient is about 13°C/km higher than average due to the low conductivity of the interval. The gradient from 3700 m to 5500 m is significantly lower, at approximately 20°C/km.

Van Oversteeg et al. (2014) performed Horner corrections for the available formation temperature evaluations recorded during logging operations. The corrected temperatures were plotted against corrected depth, allowing for the geothermal gradient to be analysed at Luttelgeest. Results revealed a positive anomaly of 45°C at the top of the Dinantian carbonate platform. A temperature of 187 is observed at the upper boundary of the layer. Within the Dinantian interval, the geothermal gradient shifts to 20°C/km, which is 10°C/km lower than the Netherlands average (Bonté et al., 2012). The temperature at the base of the Dinantian carbonates is 203°C. For the complete dataset, including a surface temperature of 10°C as determined by Bonté et al. (2012) for the Netherlands, the average geothermal gradient at LTG-01 is 39°C/km (Figure 3.9).

To determine whether the range of temperature gradients constrained by van Oversteeg (2014) is consistent with convection, the variation in temperature gradient is compared with an analytical solution for temperature in a convecting layer. The vertical temperature gradient for the case of convection in a horizontal homogenous layer with fixed temperature and impermeable boundaries at the top and base is given by:

$$\frac{\delta T}{\delta z} = \frac{\Delta T}{H}\left(4\pi\frac{\sqrt{Ra - Ra^*}}{Ra}\cos\left(\pi\frac{z}{H}\right)\cos\left(\pi\frac{x}{H}\right) - 1\right) \qquad \textbf{(3.2)}$$

where ΔT is the temperature difference across the layer, z=0 at the base of the layer and z=H at the top of the layer. The equation has minima (0) and maxima ($\Delta T/H$) at Ra = 2Ra*. The vertical temperature gradient within a convective layer can only be twice the temperature gradient across the whole layer. The gradients for LTG-01 fall within range of this.

To explain the misfit of the thermal data, Bonté et al. (2012) suggests the possibility of a magmatic intrusion that formed during the collapse of the Variscan orogeny. This study argues that the deep carbonate layer encountered at LTG-01 may host convective heat transport, assuming the layer has sufficient permeability and thickness.

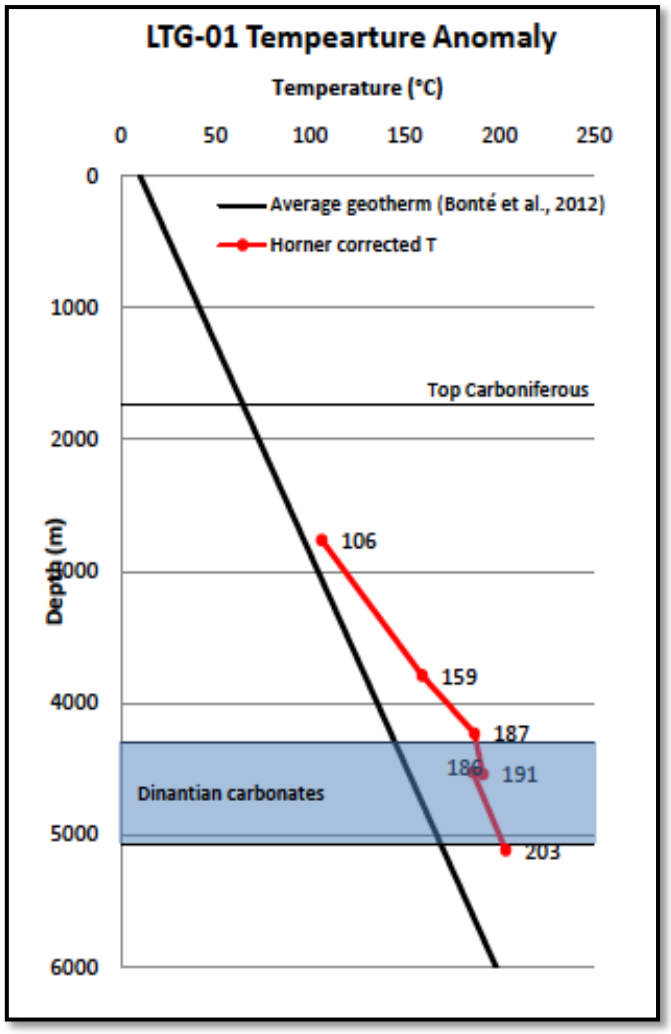

Temperature gradient from the LTG-01 data set	°C/km
Complete data set	42.6
Complete data set with T_0 at 10.1°C	39.0
Data points above Dinantian interval	54.3
Data points in the Dinantian interval	20.0
Average Netherlands for reference	31.1

Figure 3.9: Temperature vs. depth showing the Horner corrected temperatures for LTG-01 (red line) from van Oversteeg (2013). The black line shows the average gradient for the Netherlands. The shaded blue area represents the Dinantian carbonate interval

4. METHODS

4.1 Governing equations

The numerical study of thermal convection in porous media involves the coupling of heat transfer and fluid flow equations that incorporate realistic fluid and rock properties (Guillou-Frottier et al., 2013). Fluid flow through fractured or porous media can be described by Darcy's law. The fluid motion in porous and fractured media is driven by buoyancy and pressure gradients; therefore the infiltration velocity, u, can be written as:

$$u = -\frac{k}{\mu}(\nabla P - \rho_L g) \tag{4.1}$$

where k, μ, P, ρ, and g are the permeability, fluid dynamic viscosity, pressure, density and gravitational acceleration, respectively. Fluid is assumed incompressible, and the velocity, u, satisfies the mass conservation equation:

$$u \cdot \nabla = 0 \tag{4.2}$$

The temperature field is governed by the following:

$$\rho C_p \frac{\partial T}{\partial t} = \nabla(\lambda \cdot \nabla \mathrm{T}) - \rho_L C_L u \cdot \nabla \mathrm{T} \tag{4.3}$$

where λ is the thermal conductivity of the saturated porous medium, C_p is the specific heat capacity of the saturated porous medium, ρ_L the fluid density and C_L the fluid specific heat. It is assumed that properties of the saturated porous medium obey the simple mixing rule between fluid (L) and solid (s):

$$\rho C_p = \phi(\rho C_p)_L + (1-\phi)(\rho C_p)_s \tag{4.4}$$

$$\lambda = \phi(\lambda)_L + (1-\phi)(\lambda)_s \tag{4.5}$$

where ϕ is porosity (Holzbecher, 1998).

4.1.1 Fluid properties

For both the Rayleigh number analysis and numerical modelling, it is necessary to consider the effects of temperature, pressure and salinity on fluid properties. Van Oversteeg (2014) performed a parameter sensitivity study to determine a range of permeability values for the Dinantian carbonates at LTG-01. She considered multiple temperature and pressure relationships for density, specific heat, dynamic viscosity, thermal expansion and thermal conductivity and provides an overview of observed trends. The main conclusions are that thermal expansion has the greatest effect on the permeability, with density, specific heat and conductivity having an intermediate effect and viscosity only a minor effect. Similarly, van

Oversteeg (2013) investigated the effect of salinity on water properties and found that for salinity dependent density, specific heat capacity and viscosity, the permeability value increases slightly but not enough to affect the magnitude of the transmissivity. Therefore, this study only considers the temperature dependence of fluid properties.

The following properties are considered temperature dependent and have been defined here:

1. Density
2. Thermal expansion coefficient
3. Viscosity
4. Specific heat capacity
5. Thermal conductivity

Note that for all equations the input temperature must be specified in K.

Density

Yusa and Oishi (1989) determined a formula to predict the density of fresh water for temperatures ranging from 100°C to 300°C. Under single-phase conditions, the following equation provides the temperature dependent density:

$$\rho = 1758.4 + 10^3\mathbf{T} - \left(4.8434 * 10^{-3} + \mathbf{T}(1.0907 * 10^{-5} - 9.8467 * 10^{-9}\mathbf{T})\right) \quad \textbf{(4.6)}$$

The answer is given in the SI unit kg/m^3. Density decreases with increasing temperature.

Viscosity

For temperatures ranging from 100°C to 300°C, temperature dependent viscosity can be calculated using the following equation (Holzbecher, 1989):

$$\mu = 2.4141 * 10^{-5} * 10^{\frac{247.8}{\mathbf{T}-140}} \quad \textbf{(4.7)}$$

The unit for viscosity is kg/m/s or Pa·s.

Specific heat capacity

The specific heat capacity is the storage capacity for heat energy per unit mass. The ratio of heat capacity and thermal conductivity is the measure of the transient effect. As it determines how much stored heat can be moved together with a moving body, it controls the magnitude of convection. The temperature dependent specific heat capacity of both fluid and matrix increases with temperature. The specific heat capacity for temperatures ranging from 100 to 300°C is given by (Holzbecher, 1989):

$$C_p = 3.3774 - 1.12665 * 10^{-2} * \mathbf{T} + 1.31687 * 10^{-5}\mathbf{T}^{-2} \quad \textbf{(4.8)}$$

The unit for specific heat capacity is cal/g/K, which can be multiplied by 4187.6 to obtain the

SI unit of J/kg/K.

Thermal conductivity

Thermal conductivity measures the ability to transport thermal energy via conduction. Layers with a low conductivity will show steep temperature gradients. For a given system, the bulk thermal conductivity can be defined that includes both rock and fluid conductivity components. In a steady-state thermal regime, thermal conductivity expresses how early heat is transported due to a spatial variation in temperature. Temperature dependent thermal conductivity can be calculated using the following equation:

(4.9)

$$\lambda = 922.47 + 2839.5\left(\frac{\boldsymbol{T}}{273.15}\right) - 1800.7 * \left(\frac{\boldsymbol{T}}{273.15}\right)^2 + 524.77 * \left(\frac{\boldsymbol{T}}{273.15}\right)^3 - 73.44 * \left(\frac{\boldsymbol{T}}{273.15}\right)^4$$

The answer is given in W/m/K. Thermal conductivity maximizes around 140°C.

Thermal expansion

Under the assumption of zero changes in pressure and salinity, the thermal expansion coefficient can be calculated by the following formula:

$$\alpha = -\frac{1}{\rho}\frac{\partial \rho}{\partial T} \qquad \textbf{(4.10)}$$

Density input values are derived using the equations by Wooding (1957) and Yusa and Oishi (1989) given in the previous section. The thermal expansion coefficient shows a linear increase with temperature between 140°C and 220°C. Above this, it shows an exponential increase up to 300°C.

4.2 Model geometry and boundary conditions

The geometry of the model is shown in figure 4.1. The height of the domain is chosen to be 6000 m in order to observe the depth of perturbation caused by thermal convection in the convective layer. The domain extends in the x and y direction by 5000 m each. A permeable layer is placed between 4550 and 5150 m, giving it the dimensions of 600 x 5000 x 5000m.

The initial surface temperature is set to 10°C, the average surface temperature found in the Netherlands. The aquifer boundaries are no flow, representing an aquifer bounded by an underlying impermeable basement and an overlying impermeable bed such as shale. Thermal boundaries on the side are thermally insulating, meaning there is no heat flow. The heat flow boundary is set to maintain the geothermal gradient, assuming no thermal convection is taking place.

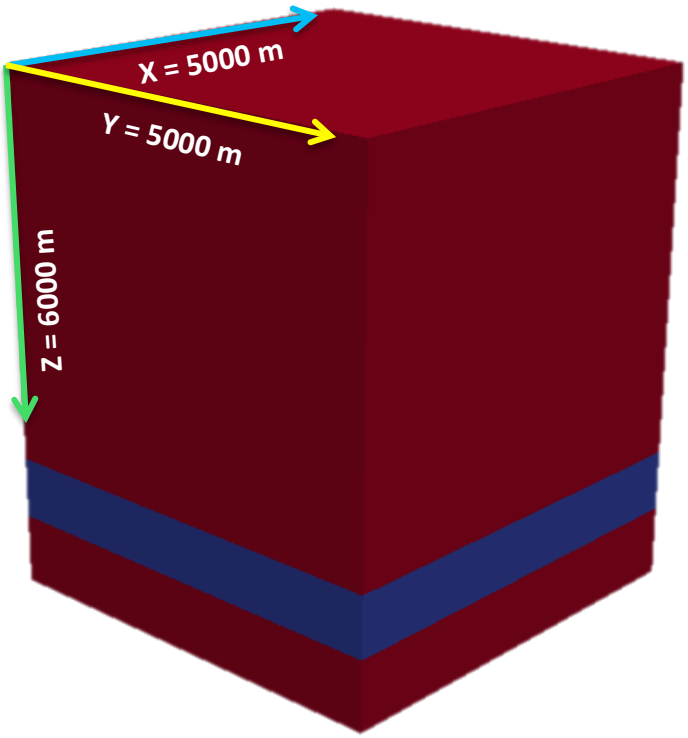

Figure 4.1: Model geometry

Simulations are initiated with the conductive temperature field perturbed by the injection of cold fluid (30°C) the centre of the domain. Without a trigger, instabilities would only form after a long time. A sensitivity analysis was carried out on the method of perturbation (temperature of fluid and location of injection), whether it affects the resultant steady state solution. Altering the location of injection of cold fluid influenced the position of upwellings and downwellings, however it did not have an effect on Ra* at which onset of instabilities occurs, nor the convective wavelength of the unstable system. Furthermore, simulations are run for 200,000 years to insure the system reaches steady state convection.

4.3 Numerical approach, setup and procedure

Numerical flow simulations are carried out using Java IDE Eclipse. Preliminary tests of free convection in porous media are presented in the form of two-dimensional models. A permeable layer with a thickness of 600 m is placed between 4500 and 5200 m, confined above and below by no flow boundaries. By testing a range of permeability values, an assessment can be made on the state of the system and the convective rigor. In order to increase the intensity of convective flows, the Ra value for the system must increase. This can be accomplished through heat source enhancement or increasing the permeability of the permeable layer. Therefore, simulations have been carried out for a wide range of permeability values, and results for permeability of 60 mD, 80 mD and 100 mD are presented.

4.3.1 Rayleigh number analysis

As discussed in section 2.1, the Rayleigh number is a classical instrument used to describe density dependent flow regimes. It characterizes the stability of the system and can predict the onset of convection. Above some Ra^*, a system is unstable and free convection occurs. The Ra^* and the critical wave number depend on the thermal and hydrologic boundary conditions exerted on the porous media (Simms and Garven, 2004). Horton and Rogers (1945) showed that Ra^* is $4\pi^2$ for a homogenous porous layer of infinite length and impervious upper and lower boundaries with fixed temperatures. Lowell (1978) considered the effect of conducting vertical boundaries, and determined Ra^* for different box dimensions and boundary conditions. The following equation applies to the model setup in this study, and will be used to determine Ra^* for the specific scenarios considered in this study (see section 2.2):

$$Ra^* = 4\pi^2 \left[1 + \left(\frac{H^2}{L^2}\right)\right] \quad \textbf{(4.11)}$$

where H is the height of the porous layer and L is the horizontal length of the layer.

Once Ra^* is known, the Rayleigh number equation can be rearranged to calculate the corresponding minimum permeability required for the onset of convection:

$$K_{min} = \frac{Ra^* \mu \lambda_e}{(\rho C_p) \rho g \alpha \Delta T H} \quad \textbf{(4.12)}$$

Site-specific values are used for ΔT and H. Temperature dependent fluid and rock parameters $(\rho, C_p, \alpha, \mu, \lambda_e)$ are determined using the equations found in section 4.1.1.

4.4 Numerical approach, setup and procedure

Scenario 1 – Preliminary tests & 3D models

Preliminary tests of free convection in porous media are first presented in the form of two-dimensional models. This is followed by three-dimensional models with the same model setup. This study refers to the work by van Oversteeg (2013), who identified the interval of Dinantian carbonates with increased fracture permeability at well LTG-01 between 4550 and 5150m measured depth. The initial temperature field is set to the average geothermal gradient for the Netherlands, 31°C/km, thereby corresponding to temperatures of 151 – 169°C within the permeable layer. Once temperature is constrained, temperature-dependent fluid properties can be determined using the equations in section 4.1.1. The final variable to determine is Ra^*. For a 3D rectangular box with H=600 and L=5000:

$$4\pi^2\left[1+\left(\frac{H^2}{L^2}\right)\right]=4\pi^2\left[1+\left(\frac{600^2}{5000^2}\right)\right]=40.05 \quad \textbf{(4.13)}$$

By testing a range of permeability values, an assessment can be made on the state of the system and the convective rigor. In order to increase the intensity of convective flows, the Ra value for the system must increase. This can be accomplished through heat source enhancement or increasing the permeability of the layer. Therefore, simulations have been carried out for a permeabilities ranging between 10 and 200 mD. Table 4.1 lists all relevant parameters.

Table 4.1: All parameters used in Scenario 1

Parameter	31°C/km	Units
T range	151 - 169	°C
ΔT	18	°C
H	600	m
ρ	906	kg/m3
α	$1x10^{-3}$	1/°C
μ	$1.85x10^{-4}$	kg/m/s
C_p	4289	J/kg/K
λ_e	2.78	W/m/K
Ra*	40.05	----

Scenario 2 – Temperature

In scenario 2, the geothermal gradient is increased to assess the effects it has on the conditions necessary for the onset of convection. Two different cases are considered: (1) 36°C/km and (2) 39°C/km. The first case of 36°C/km has been chosen to investigate the overall effects of increasing the gradient by 15%. The second case of 39°C/km has been chosen based on the work by Van Oversteeg (2013), who used Horner corrected temperatures from LTG-01 to calculate the temperature gradients for different depth intervals. The complete data set, with a surface temperature set at 10°C, was determined to be 39°C/km. Therefore, this is considered to be an average gradient, which includes various effects from lithological conductivities.

The corresponding temperature ranges for the 600 m layer are 173 – 195°C and 187 – 210 °C for 36°C/km and 39°C/km, respectively. All additional conditions are the same as scenario 1, therefore Ra^* remains 40.05. All temperature-dependent fluid properties have been determined for each case and are listed in Table 4.2

Table 4.2: All parameters used in Scenario 2

Parameter	36°C/km	39°C/km	Units
T range	173 – 195	187 – 210	°C
ΔT	22	23	°C
H	600	600	m
ρ	882	866	kg/m3
α	$1.2x10^{-3}$	$1.3x10^{-3}$	1/°C
μ	$1.45x10^{-4}$	$1.34x10^{-4}$	kg/m/s
C_p	4365	4497	J/kg/K
λ_e	2.78	2.78	W/m/K
Ra*	40.05	40.05	----

Scenario 3– Thickness

Fluid circulation depends on not only the permeability of the layer, but also the thickness. In scenario 4, the thickness of the layer is increased to assess the effect the layer thickness has on convection cell development and temperature distribution. Two cases are considered: (1) 15% increase to H=900 (4300 – 5200m) and (2) 25% increase to H=1200 (4000 – 5200m). The depth locations have been chosen to represent possible realistic situations for the Dinantian carbonate platform encountered at LTG-01. In this way, temperature-dependent properties can be accurately approximated to represent conditions. The corresponding temperature ranges for H=900 m and H=1200 m are 165 – 183°C and 159 – 183°C, respectively. As the layer dimensions have changed, a new Ra^* must be calculated. For a 3D rectangular box with H=900 and L=5000:

$$4\pi^2\left[1+\left(\frac{H^2}{L^2}\right)\right]=4\pi^2\left[1+\left(\frac{900^2}{5000^2}\right)\right]=40.75 \quad \textbf{(4.14)}$$

$$4\pi^2\left[1+\left(\frac{H^2}{L^2}\right)\right]=4\pi^2\left[1+\left(\frac{1200^2}{5000^2}\right)\right]=40.75 \quad \textbf{(4.15)}$$

Table 4.3 lists the temperate-dependent properties for both cases in scenario 3.

Table 4.3: All parameters used in Scenario 3

Parameter	900m	1200m	Units
T range	143 – 171	134 – 171	°C
ΔT	28	37	°C
H	900	1200	m
ρ	913	909	kg/m^3
α	$1.01x10^{-3}$	$1x10^{-3}$	1/°C
μ	$1.72x10^{-4}$	$1.77x10^{-4}$	kg/m/s
Cp	4285	4280	J/kg/K
λe	2.78	2.78	W/m/K
Ra*	40.75	40.75	----

5. RESULTS

5.1 Preliminary tests and 3D models

5.1.1 Rayleigh number analysis

For the given boundary conditions, we assume Ra* is 40.05 based on the work by Lowell (1978). The minimum permeability for the onset of convection is calculated using equation 4.13 and the parameters listed in table 4.1. The resulting minimum permeability is 5.52×10^{-14} (55 mD). Consequently, convection is expected to occur if the permeability is greater than 55 mD, assuming all other conditions remain constant.

Several simulations been carried out where permeability is varied between 10 mD to 200 mD. In simulations, convective fluid motion did not occur when permeability was below 58 mD (5.72×10^{-14}). To illustrate the role of permeability on the timing of convection onset, the development and structure of convective patterns and the resulting temperature patterns, results for (a) 60 mD (b) 80 mD and (c) 100 mD permeability are presented. As the permeability is not equal to 55 mD in all cases, the system will have an Ra that is different from Ra^*. Table 5.1 lists the system Ra for each case presented.

Table 5.1: The theoretical and modelled k_{min} as well as the system Ra for cases of 60 mD, 80 mD and 100 mD.

k_{min} (theoretical)	k_{min} (modelled)	Ra - 60 mD	Ra - 80 mD	Ra - 100 mD
55 mD	58 mD	43	57	71

Preliminary tests

Results of the two-dimensional preliminary numerical simulations are illustrated in Figure 5.1, which shows the temperature distribution and vertical velocity at mid-depth of the permeable layer (z=4800 m). Convection cell width has been determined by halving the distance between thermal highs, and then taking the average. Once steady state has been reached, the pattern of thermal highs and lows and the average cell width are identical between scenarios of different permeability. Each case presents 5 full convection cells with an average width of 900m, along with 2 half cells at each side of the domain. However, the timing of convective onset and the effect of convective fluid flow on temperature is different from case to case.

For a permeability of 60mD, steady state is reached at t=50,000 years and the fluid velocity at mid-depth is between 2×10^{-17} and 4×10^{-7} ms^{-1}. For 80 mD permeability, the system reaches steady state sooner at t=40,000 years and fluid velocity at mid-depth is between 2×10^{-7} and 4×10^{-7} ms^{-1}. When the permeability is increased to 100 mD, steady state is reached considerably earlier at t=35,000 years and steady state fluid velocity within the permeable

layer remains between $2x10^{-17}$ and $4x10^{-7}$ ms^{-1}. The modelled temperature inside the two ascending plumes, just below the top boundary layer, reaches 155°C, 157°C and 161°C for a permeability of 80 mD, 100 mD and 200 mD, respectively. These findings indicate that permeability has a large influence on the temperature distribution and the time it takes to reach steady state. The lower the permeability, the longer it takes to reach steady-state, whereupon a more diffusive dominated system results leading to lower temperatures (Bächler et al., 2003) (Figure 5.1)

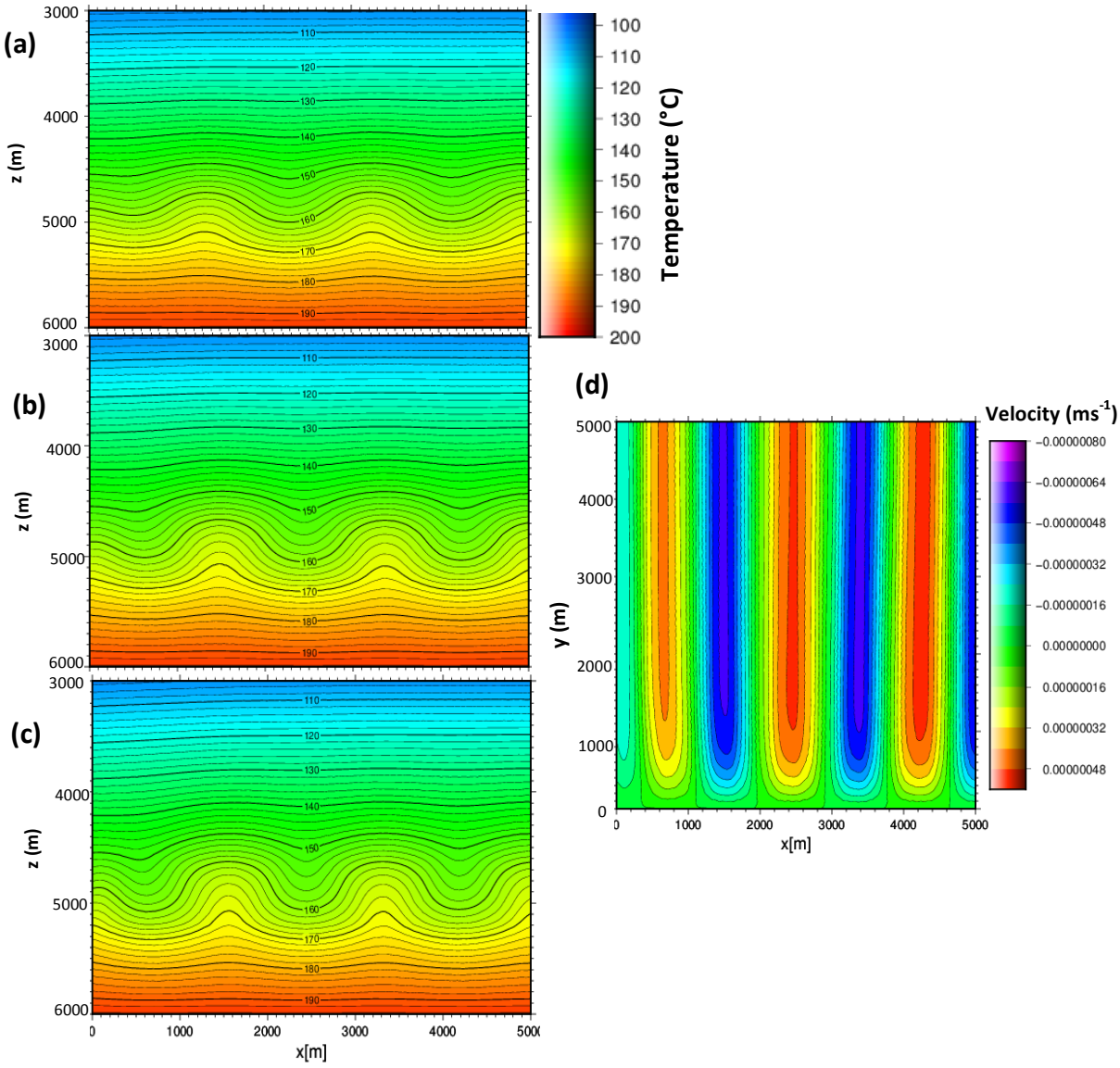

Figure 5.1: (a–c) Temperature distribution in 2D numerical models at the end of simulation (t=200,000 years), corresponding to 60 mD, 80mD and 100 mD permeability, respectively. **(d)** vertical velocity at mid-depth of the permeable layer (z=4800 m).

The results from the simple 2D numerical models with varying permeability agree with analytical solutions, furthermore providing insight on the role of permeability during convection cell development.

5.1.2 3D Model results

Convection structure and pattern development

Simulations all reveal that the development and number of convection cells is very much a time dependent process. In the beginning of simulations, many convection cells may develop but seem to gradually converge until steady state is reached. Van Oversteeg (2013) estimated that the permeability of the 600 m carbonate interval at LTG-01 is 60 mD; therefore, results for 60 mD permeability are presented first.

During the initial stages of simulation, the system gradually develops into a distinct convective pattern of alternating up-flows and down-flows, and reaches steady state at t=170,000 years. The convection shape is roughly circular or hexagonal in plan view, comprised of downwellings surrounded by a circle of upwelling fluid (Figure 5.2a). The fluid velocity is between $1x10^{-7}$ and $6.5x10^{-7}$ ms^{-1}. Figure 5.2 (b)-(c) shows a temperature slice of the vertical plane at coordinate y=2500 m and temperature difference at mid-depth of the permeable layer (z=4800m) at t=200,000 years. A positive anomaly of 7° and a negative anomaly of 6°C is observed.

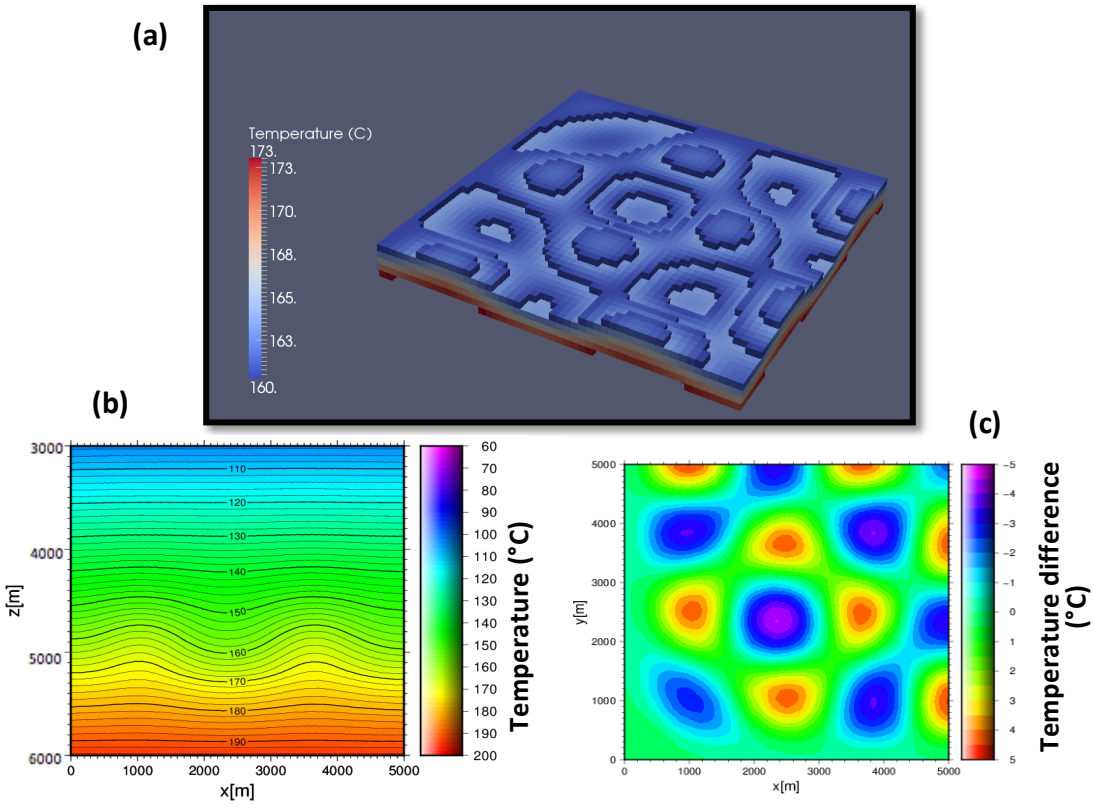

Figure 5.2: Results for 60 mD at the end of simulation (t=200,000 years). **(a)** Temperature distribution in 3D **(b)** Temperature slice of the vertical plane at coordinate y=2500 m **(c)** Temperature difference at mid-depth of the permeable layer (z=4800 m).

When the permeability is increased to 80 mD, steady state is reached earlier, at t=150,000 years. The fluid velocity is between $1x10^{-7}$ and $7x10^{-7}$ ms^{-1}, approximately the same as seen

for 60 mD. Figure 5.3b compares the temperature of the vertical plane at coordinate y=2500 m at (a) 50,000 years and (b) 200,000 years. Initially, 2 fully developed upwelling plumes develop in addition to two half plumes at the edges. The system is still in a state of transition. From t=50,000 years and t=150,000 years, convection cells slowly migrate until reaching a steady state position, seen in 5.3b by the convergence of cells at the left of the domain into one upwelling plume. Motion takes the form of 8 convection cells with widths averaging between 500 and 600 m, corresponding to an aspect ratio of 1. The structural change during convection cell development is clearly depicted in Figure 5.3c, where mid-depth (z=4800) temperature differences are shown for t=50,000 and t=200,000 years. At t=50,000 years, the convection cell type is a 2D roll, characterized by elongate upwellings and downwellings. At t=200,000 years, the two dimensional rolls and circular/hexagonal type with a central upwelling surrounded by a circle of downwelling fluid merges together to create complex three dimensional polyhedral cells.

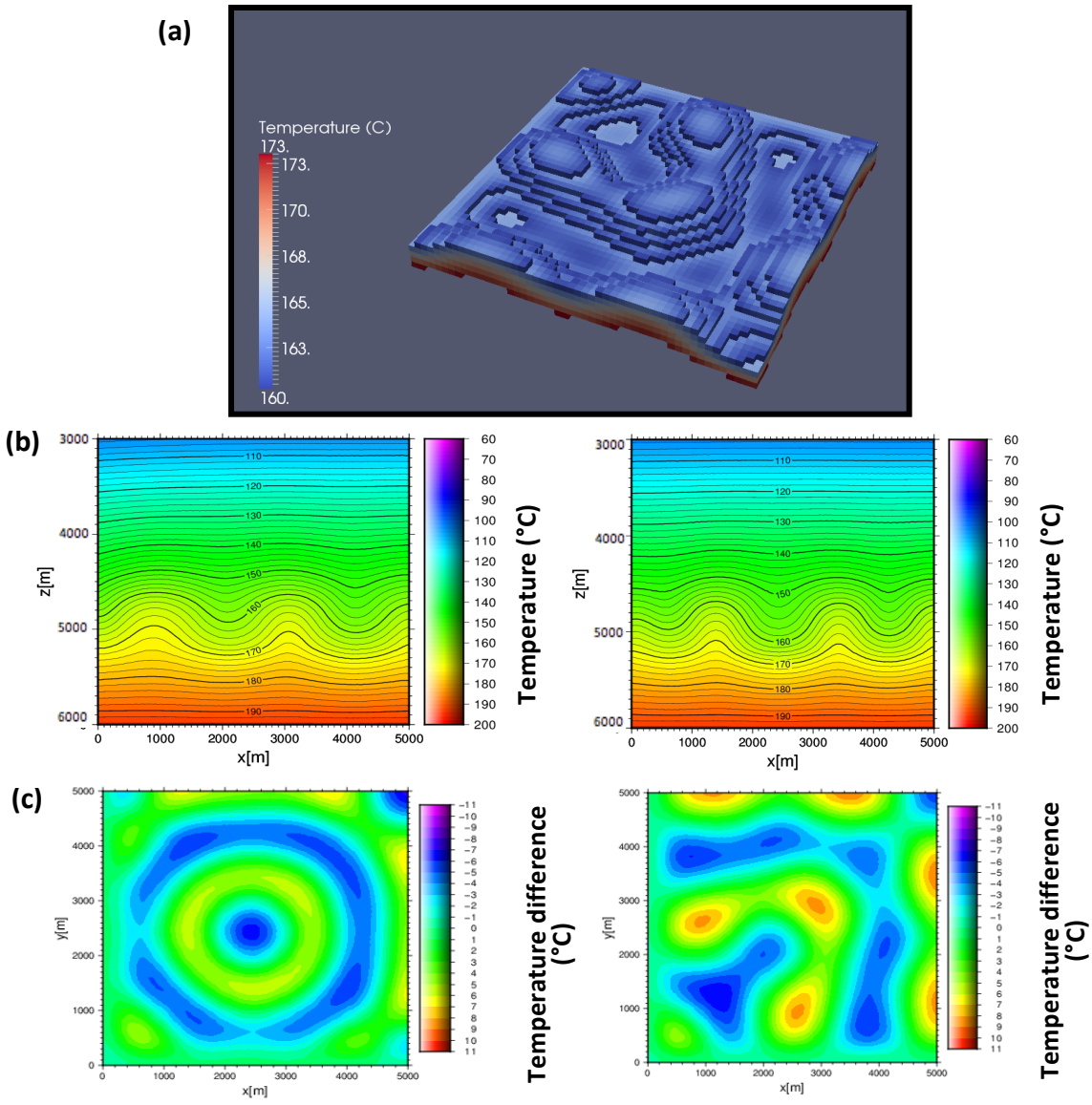

Figure 5.3: Results for 80 mD **(a)** Temperature distribution in 3D at the end of simulation (t=200,000 years). **(b)** Temperature slice of the vertical plane at coordinate y=2500 m at t=50,000 years (left) and t=200,000 years (right). **(c)** Temperature difference at mid-depth of the permeable layer (z=4800 m) at t=50,000 years (left) and t=200,000 years (right).

A similar pattern development occurs when the permeability is increased an additional 20 mD to 100 mD, however the timing of pattern development differs. Figure 5.4b shows the temperature slice at coordinate y=2500 m at t=50,000 and t=200,000 years. At t=50,000 years, the convection pattern shows a striking resemblance to that of 80 mD in the form of elongate upwellings and downwellings; however, the temperature at mid depth of the convective layer oscillates around 162 degrees, which is 4 degrees higher than seen for 80 mD. This suggests that an increase in permeability does not necessary effect the development of cell patterns, but it will result in higher temperatures within the permeable layer. The fluid velocity at t=200,000 years is between $1x10^{-7}$ and $7x10^{-7}$ ms^{-1}, the same as observed for 60 mD and 80 mD.

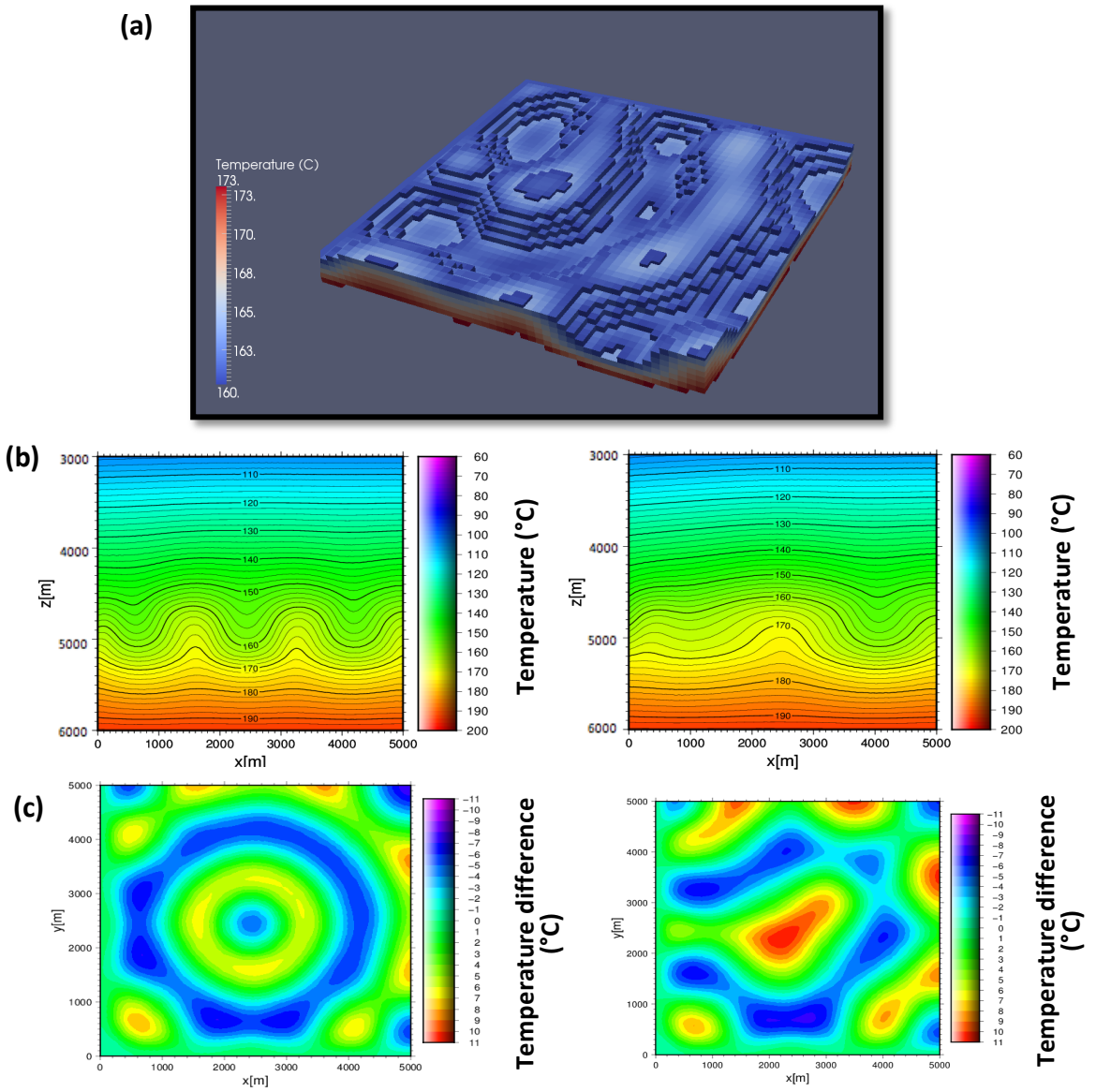

Figure 5.4: Results for 100 mD **(a)** Temperature distribution in 3D at the end of simulation (t=200,000 years). **(b)** Temperature slice of the vertical plane at coordinate y=2500 m at t=50,000 years (left) and t=200,000 years (right). **(c)** Temperature difference at mid-depth of the permeable layer (z=4800 m) at t=50,000 years (left) and t=200,000 years (right).

Temperature distribution

The temperature difference just below the top flow boundary (z=4500) is observed. For 60 mD, the temperature within ascending plumes reaches 155°C, a positive anomaly of 6°C. For 80mD, temperature reaches 158°C, a positive anomaly of 9°C. Lastly for 100 mD, temperature within ascending plumes reaches 160°C, a positive anomaly of 11°C. The observed positive anomaly nearly doubles when the permeability is increased from 60 to 100 mD.

To understand how permeability effects the temperature distribution with depth, temperature gradients have been determined for 60 mD, 80 mD, 100 mD and 200 mD by averaging the temperature observed at each depth. The gradients obtained from modelled temperatures have then been compared with the linear geothermal gradient of 31°C/km in Figure 5.4.

Although lateral positive and negative anomalies are observed for all cases at both the top and mid-depth of the permeable layer, the temperature gradient does not appear to be significantly affected by convective fluid flow until the permeability is 80 mD. In this case, the gradient steadily increases at 3000 m continuing to 4500 m (the top of the permeable layer) at which point the deviation is +2.5°C. Through the layer, the gradient decreases below 31°C /km reaching a deviation of -1.2°C at the base of the layer. When the permeability is increased to 100 mD, the effects of fluid flow are more prevalent. Like for the case of 80 mD, the largest deviation (+3.4°C) is observed at the top of the permeable layer. The gradient decreases through the layer and reaches a deviation of -1.9°C at the base. Doubling the permeability to 200 mD causes the gradient to deviate away from 31°C /km at a shallower depth. Both the positive (+6.8°C) and negative (-3.3°C) nearly double between 100 and 200 mD.

Table 5.2 lists the temperature change and resulting gradient for 60, 80, 100 and 200 mD. The results suggest that the higher the deviation away from 31°C/km at the top of the convective layer, the smaller the temperature change within the layer, and thus the lower the average gradient through the layer. Initially, an increase in permeability has a larger effect on the average gradient, which can be seen by comparing 60 mD to 100 mD. Furthermore, it shows that from 100 to 200 mD the gradient within the convective layer is less sensitive to a permeability increase.

Table 5.2: Modelled temperature change and resulting geothermal gradient within the permeable layer for 60 – 200 mD permeability.

Permeability	Temperature change	Temperature gradient
60 mD	18.4 °C	30 °C/km
80 mD	15.2 °C	25 °C/km
100 mD	12.9 °C	21 °C/km
200 mD	11.6 °C	19 °C/km

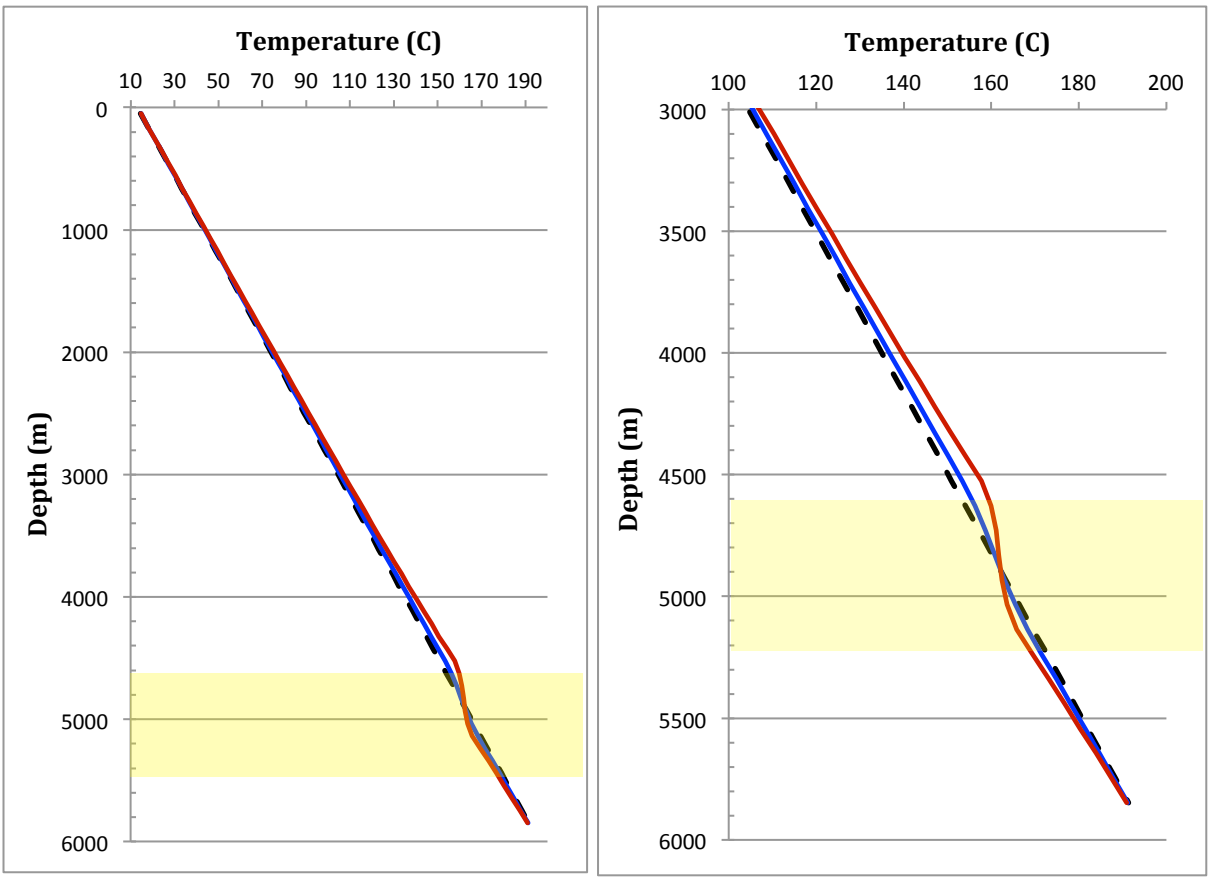

Figure 5.5: Temperature vs. depth for modelled temperature in the cases of 80 mD (blue line) and 100 mD (red line) permeability. The linear gradient has been added for comparison (black dashed line). The graph on the right is a zoomed in version of the graph on the left.

5.2 Scenario 2 – the role of geothermal gradient increase

Scenario 2 addresses the geothermal gradient and its effect on the timing of convective onset, convection cell pattern development and modeled temperature distribution with depth. Initially, the gradient is increased by 15% to 36km/°C, followed by a 25% increase to 39°C/km.

5.2.1 Rayleigh number analysis

As the boundary conditions remain the same as scenario 1, Ra^* is assumed to be 40.05. The minimum permeability for the onset of convection is calculated for each temperature gradient using equation () and the parameters listed in table (). The resulting minimum permeability is $3x10^{-14}$ (31mD) and $2.5x10^{-14}$ (25mD) for 36°C/km and 39°C/km, respectively. Consequently, convection is expected to occur if the permeability is greater than 31 mD and 25 mD for the appropriate temperature gradient.

As in scenario 1, several simulations been carried out where permeability is varied between 10 mD to 200 mD. Convective fluid motion did not occur when permeability was below 30 mD ($3.5x10^{-14}$) for 36°C/km and 30 mD ($3x10^{-14}$) for 39°C/km. For each case, results for (a) 80

mD and (b) 100 mD permeability are presented. The system Ra for each case is listed in table 5.3.

Table 5.3: The theoretical and modelled k_{min} as well as the system Ra for cases of 80 and 100 mD permeability.

Temperature gradient - 36°C/km			
k_{min} (theoretical)	**k_{min} (modelled)**	**Ra - 80 mD**	**Ra - 100 mD**
$3x10^{-14}$ (31mD)	$3.5\ x10^{-14}$ (35mD)	108	135
Temperature gradient - 39°C/km			
k_{min} (theoretical)	**k_{min} (modelled)**	**Ra - 80 mD**	**Ra - 100 mD**
$2.5x10^{-14}$ (25mD)	$3x10^{-14}$ (30mD)	127	159

5.2.2 36°C/km results

Convection structure and pattern development

For a permeability of 60 mD, steady state is reached at t=175,000 years, which is 5000 years after that for 60 mD in Scenario 1. The convection cell shape is the same as in Scenario 1, thus the convection shape can be described as roughly circular or hexagonal in planview. However this time, an upwelling is seen in the middle of the domain instead of a downwelling plume. Fluid velocity is between $2x10^{-7}$ and $7x10^{-7}$ ms^{-1}.

Figure 5.6 shows the results for 80 mD permeability. The system reaches steady state sooner than for 60 mD at t=160,000 years, which 10,000 years after that for 80 mD in Scenario 1. A downwelling plume occupies the center of the domain, and both two dimensional rolls and circular/hexagonal type convection shapes are seen. Figure 5.6b shows a vertical plane at coordinate y=2500, in which 2 fully-developed upwelling plumes are seen, corresponding to 6 cells of convective motion. The average width of the cells is 700m. For a permeability of 100 mD, an upwelling plume is appears in the middle of the domain again when the system reaches steady state at t=158,000 years (Figure 5.7). The convection cell shape takes the form of a complex 3D shape of polyhedral cells. For both 80 mD and 100 mD, the fluid velocity is between $5x10^{-7}$ and $1x10^{-6}$ ms^{-1}.

(a)

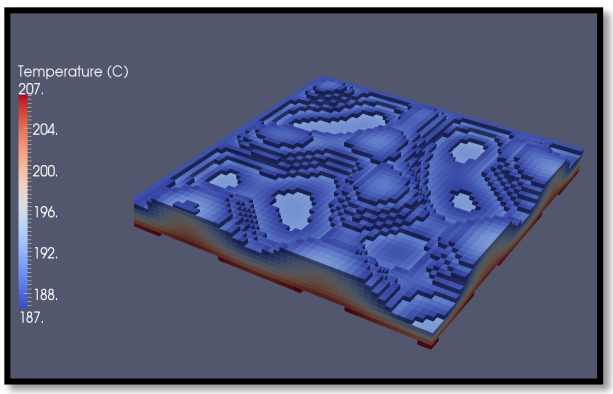

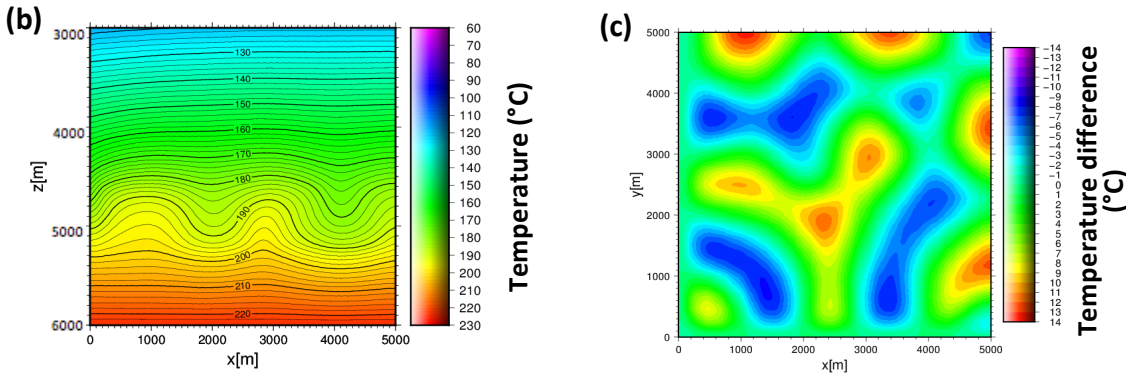

Figure 5.6: Results for 80 mD at the end of simulation (t=200,000 years). **(a)** Temperature distribution in 3D **(b)** Temperature slice of the vertical plane at coordinate y=2500 m **(c)** Temperature difference at mid-depth of the permeable layer (z=4800 m).

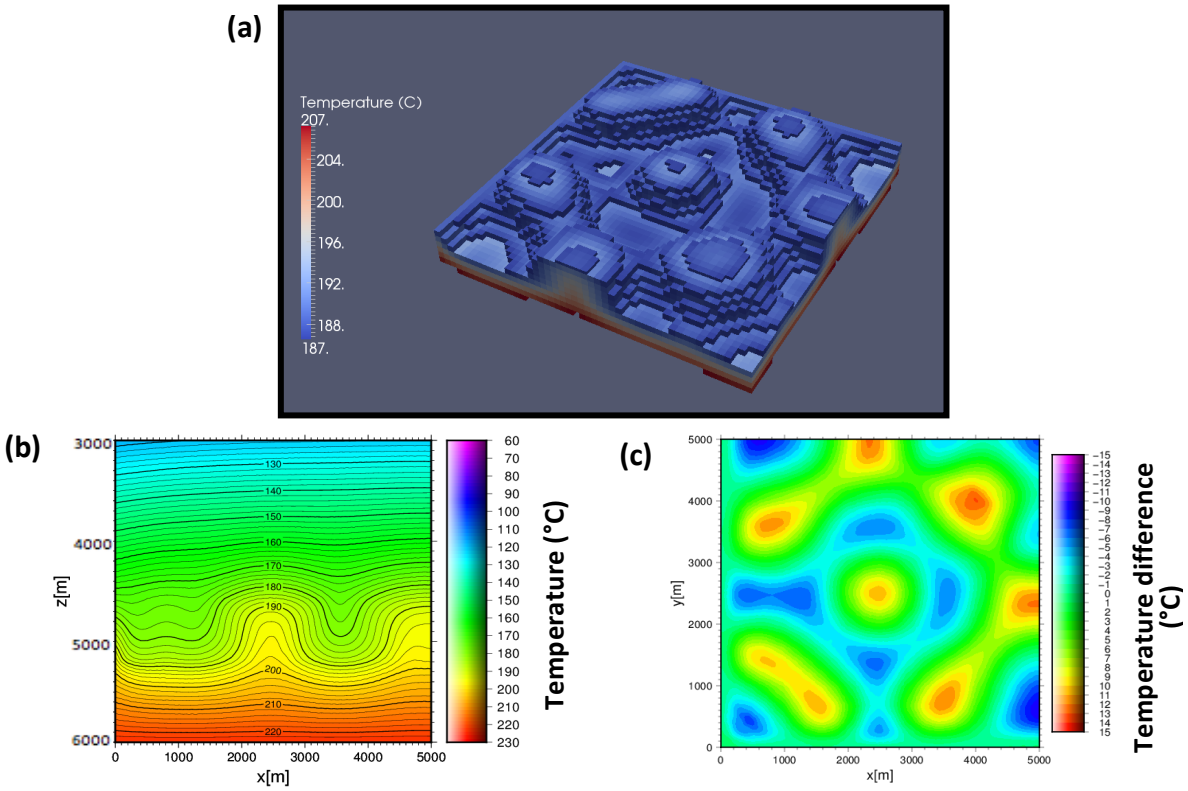

Figure 5.7: Results for 100 mD at the end of simulation (t=200,000 years). **(a)** Temperature distribution in 3D **(b)** Temperature slice of the vertical plane at coordinate y=2500 m **(c)** Temperature difference at mid-depth of the permeable layer (z=4800 m).

Temperature distribution

The temperature difference just below the top flow boundary (z=4500) is observed. For 60 mD, the temperature within ascending plumes reaches 183°C, a positive anomaly of 11°C. For 80 mD, the temperature reaches 187°C, a positive anomaly of 13°C. Lastly for 100 mD, temperature within ascending plumes reaches 189°C, a positive anomaly of 15°C.

The geothermal gradient has been determined for the modelled temperatures for each permeability. The results are presented in Figure 5.8. For a permeability of 60 mD, the gradient steadily increases from 3800 m to the top of the permeable layer at 4500 m, at

which point a deviation of +3.4°C is observed. The gradient decreases through the layer, reaching a negative deviation of -1.7°C. As seen in the previous scenario, when the permeability is increased to 80 mD, the effects of fluid circulation on the gradient are stronger. The gradient deviates +5.3°C and -2.7°C, observed at the top and bottom of the permeable layer. A permeability of 100 mD causes the gradient to reach a deviation of +6.8°C and -3.1°C at the upper and lower boundary of the permeable layer. In comparing the shape of the gradients between different permeability, the layers directly above the layer appear to be more sensitive to fluid circulation, as the positive deviation increases more strongly with increasing permeability than the negative deviations. This is also the case when comparing the temperature difference at the base of the layer for each permeability, which is -9 (60 mD), -11 (80 mD) and -13 (100 mD).

Table 5.4 lists the temperature change and resulting gradient for 60, 80, 100 and 200 mD. The linear unperturbed gradient is also included for comparison.

Table 5.4: Modelled temperature change and resulting geothermal gradient within the permeable layer for 60 – 200 mD permeability.

Permeability	Temperature change	Temperature gradient
Linear	21.6°C	36°C/km
60 mD	16.4 °C	27 °C/km
80 mD	13.4 °C	22 °C/km
100 mD	11.9 °C	20 °C/km
200 mD	7.1 °C	12 °C/km

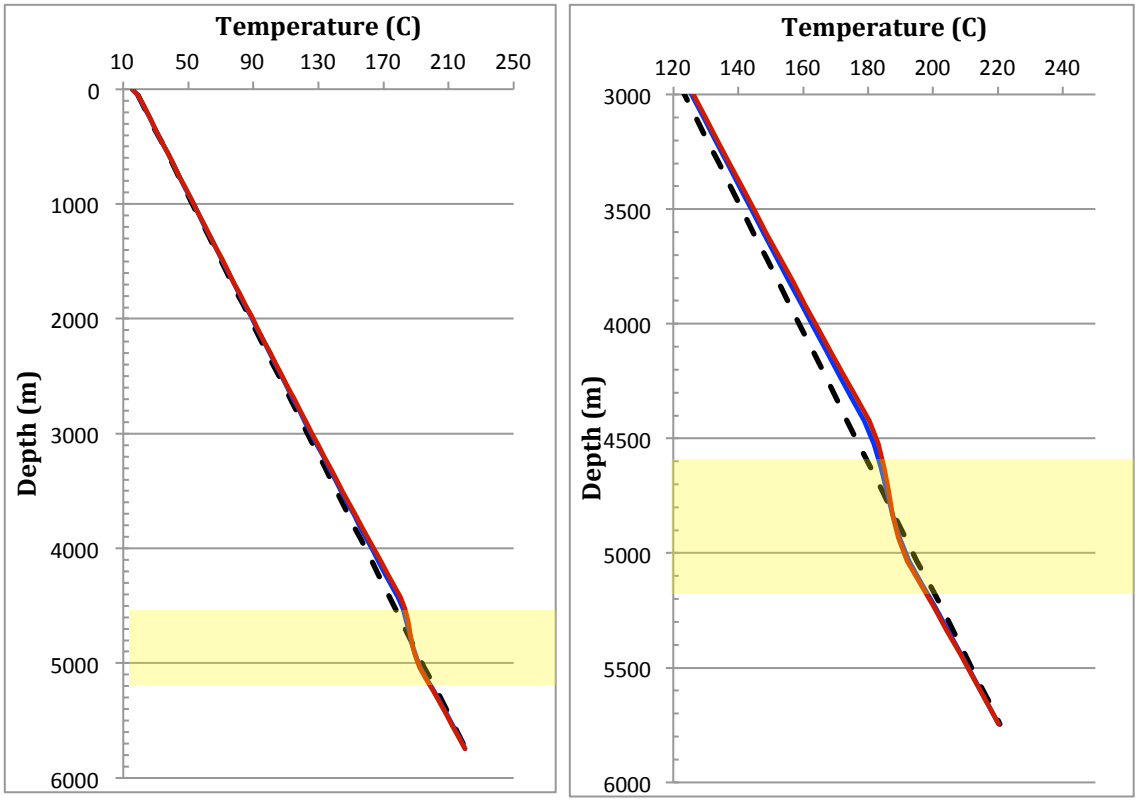

Figure 5.8: Temperature vs. depth for modelled temperature in the cases of 80 mD (blue line) and 100 mD (red line) permeability. The linear gradient has been added for comparison (black dashed line).

5.2.3 39°C/km

For a permeability of 60 mD, steady state is reached at t=175,000 years, which is 5000 years after that for 60 mD in Scenario 1. The convection cell shape is the same as in Scenario 1, thus the convection shape can be described as roughly circular or hexagonal in planview. However this time, an upwelling is seen in the middle of the domain instead of a downwelling plume. Fluid velocity is between $2x10^{-7}$ and $7x10^{-7}$ ms^{-1}.

For a permeability of 60 mD, steady state is reached at t=170,000 years. The system develops a convection cell structure identical to the one seen in the previous case of 36°C/km. However, a higher geothermal gradient results in higher temperatures observed within and directly above the permeable layer. The same trend is seen for 80 mD, in that convection cells develop the same structure as for 80 mD permeability and a gradient of 36°C/km (Figure 5.9).

When the permeability is increased to 100 mD, the system differs from the structure seen for 100 mD permeability with a gradient of 36°C/km. Figure 5.10b shows the progression of pattern development, with snapshots at t=50,000, t=100,000 and t=200,000 years. Initially 3 upwelling plumes develop as show by the vertical plane at coordinate y=2500 m at t=50,000 years. With an additional 50, 000 years, the system undergoes a considerable degree of change, seen by a transition from 3 to 2 upwelling plumes. The system reaches a steady state by t=200,000 years, at which point 2 fully developed upwelling plumes, are seen. Though the system may be in a state of transition for the first 150,000 years, the isotherms through time indicate that the overall temperature perturbation increases with time.

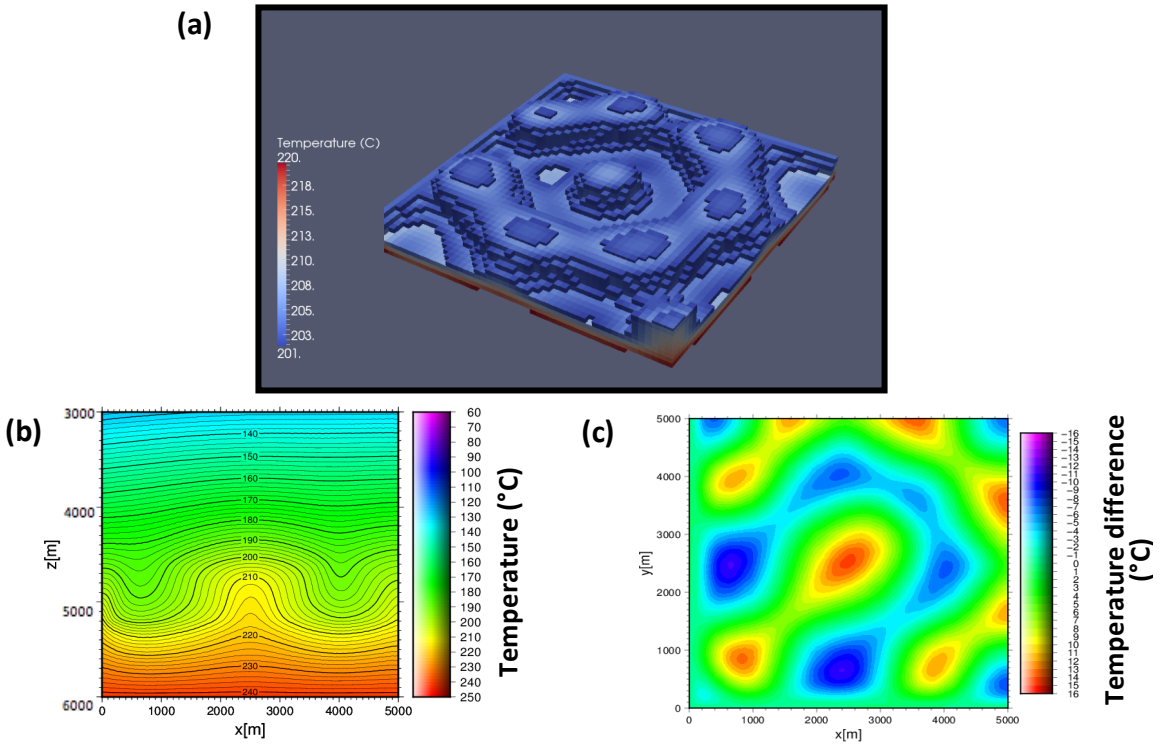

Figure 5.9: Results for 80 mD at the end of simulation (t=200,000 years). **(a)** Temperature distribution in 3D **(b)** Temperature slice of the vertical plane at coordinate y=2500 m **(c)** Temperature difference at mid-depth of the permeable layer (z=4800 m).

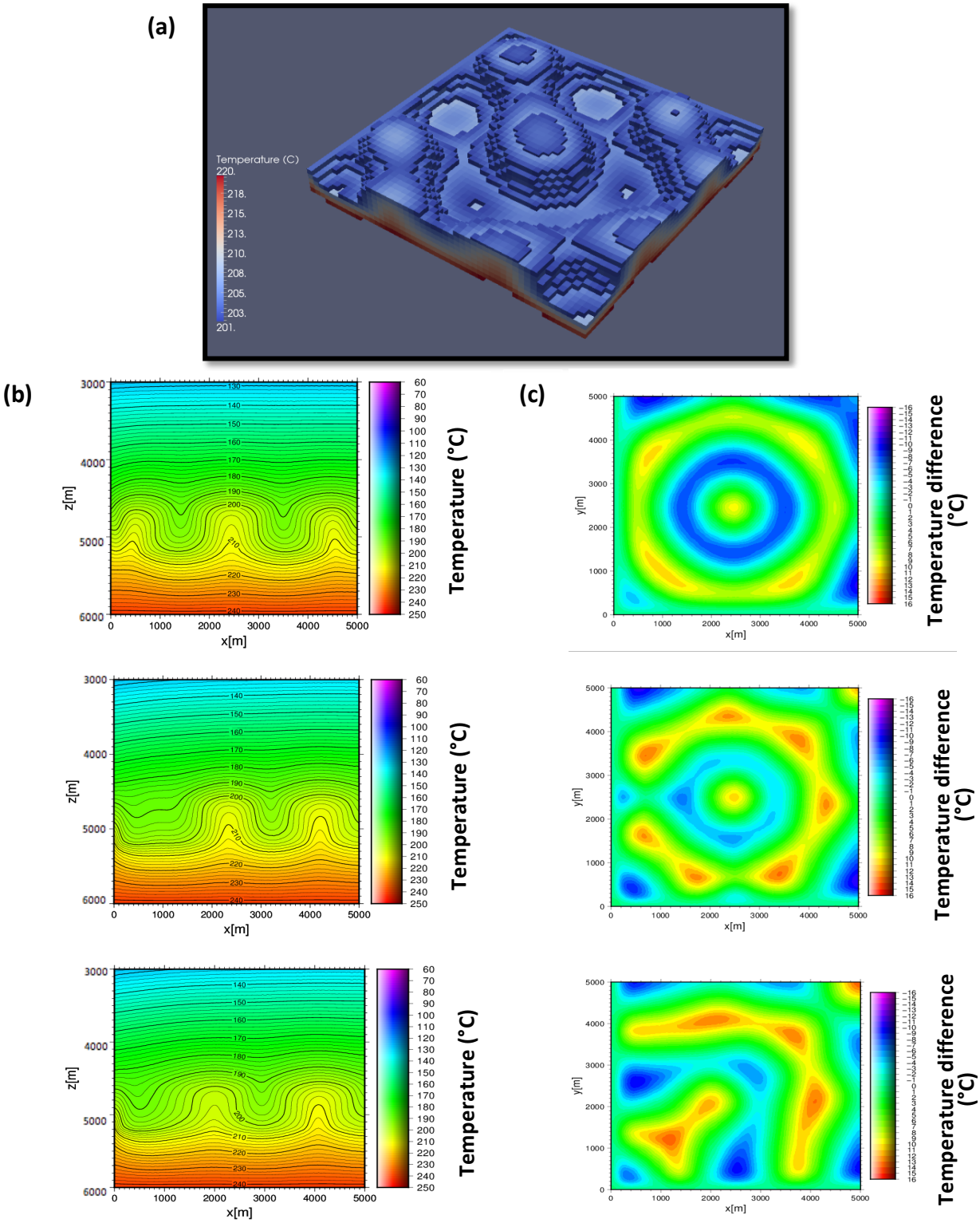

Figure 5.10: Results for 100 mD **(a)** Temperature distribution in 3D at the end of simulation (t=200,000 years) **(b)** Temperature slice of the vertical plane at coordinate y=2500 m at t=50,000 years (top), t=100,000 years (middle) and t=200,000 years (bottom) **(c)** Temperature difference at mid-depth of the permeable layer (z=4800 m) at t=50,000 years (top), t=100,000 years (middle) and t=200,000 years (bottom).

As with the previous case, the temperature gradient has been determined for the modelled temperatures for each permeability. The results are shown in figure 5.11. For a permeability of 80 and 100 mD, the gradient increases slightly at 3000 m, with 100 mD experiencing the greatest deviation of the line slope. At the top of the permeable layer, deviations of +5.07°C +6.95°C (80 mD) and +8.41°C (100 mD) are observed. At the base of the layer, deviations of -3.7°C (80 mD) and -3.8°C (100 mD) are seen.

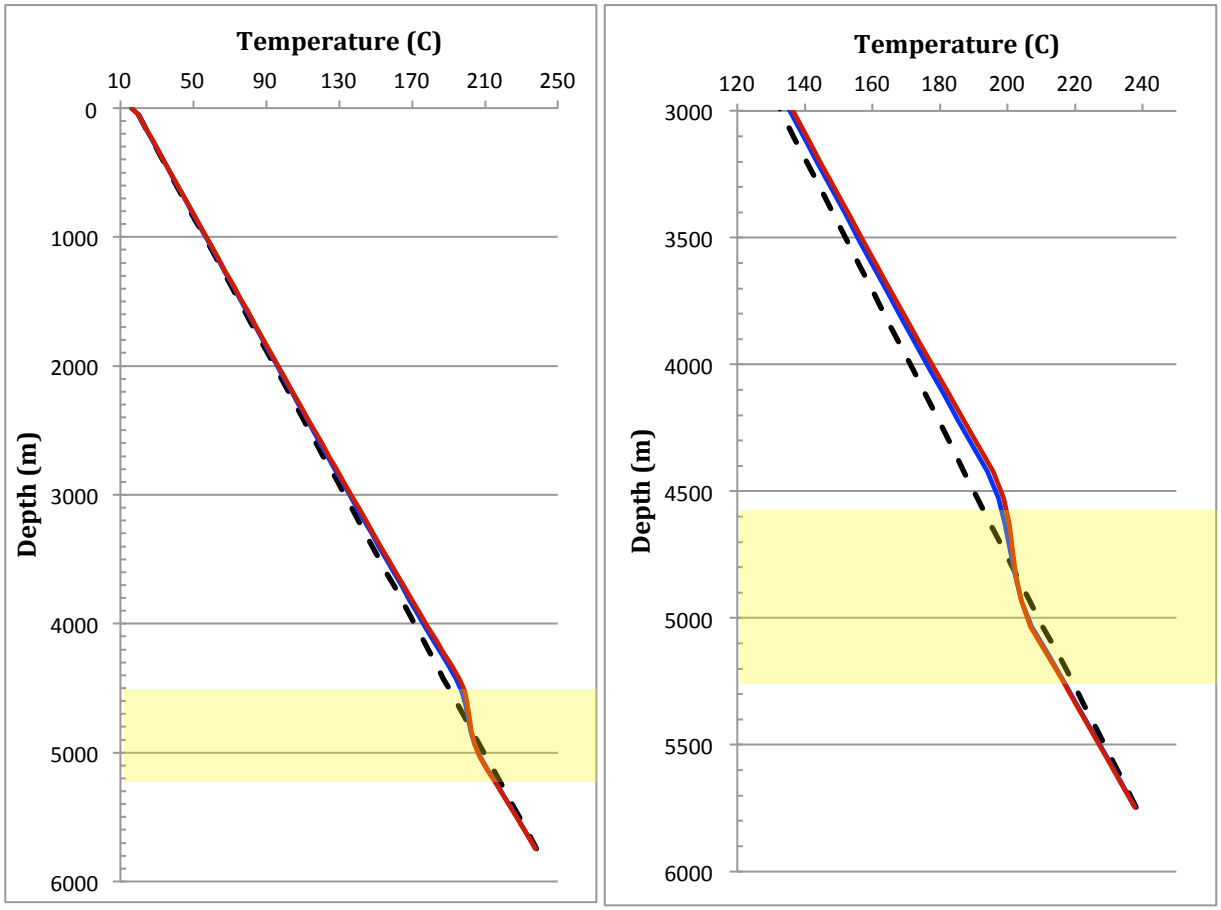

Figure 5.11: Temperature vs. depth for modelled temperature in the cases of 80 mD (blue line) and 100 mD (red line) permeability. The linear gradient has been added for comparison (black dashed line).

Table 5.5 lists the temperature change and resulting gradient for 60, 80, 100 and 200 mD. The linear unperturbed gradient is also included for comparison.

Table 5.5: Modelled temperature change and resulting geothermal gradient within the permeable layer for 60 – 100 mD permeability.

Permeability	Temperature change	Temperature gradient
Linear	23.4°C	39°C/km
60 mD	15.5 °C	26 °C/km
80 mD	12.7 °C	20°C/km
100 mD	11.6 °C	18 °C/km

5.3 Scenario 3 – the role of thickness increase

Scenario 3 addresses the thickness of the permeable layer its effect on the timing of convective onset, convection cell pattern development and modeled temperature distribution with depth. Both a thickness of 900 m and 1200 m are tested.

5.3.1 Rayleigh number analysis

An increase in layer thickness from 600m to 900m and 1200m will affect the geometry and spatial distribution of convection cells. For the new model dimensions, Ra^* is 40.75. The minimum permeability for the onset of convection is calculated for each layer thickness using the equation () and the parameters listed in table (). The resulting minimum permeability for H=900 m and H=1200 m is $2.21x10^{-14}$ (22mD) and $1.28x10^{-14}$ (17mD), respectively.

The same approach is used for scenario 3, wherein several simulations have been carried out with permeability varied between 10 mD and 200 mD. Convective fluid motion did not occur when permeability was below 28 mD ($3.0x10^{-14}$) for H=900 m and 20 mD ($2.5x10^{-14}$) for H=1200 m. The system Ra for each permeability case has been calculated and is listed in table 5.6.

Table 5.6: Modelled temperature change and resulting geothermal gradient within the permeable layer for 60 – 100 mD permeability.

Thickness – 1200 m			
k_{min} (theoretical)	**k_{min} (modelled)**	**Ra - 80 mD**	**Ra - 100 mD**
$1.29x10^{-14}$ (12mD)	$1.8x10^{-14}$ (18 mD)	290	363
Thickness – 900 m			
k_{min} (theoretical)	**k_{min} (modelled)**	**Ra - 80 mD**	**Ra - 100 mD**
$1.72x10^{-14}$ (17mD)	20 mD	184	230

5.3.2 H=900 m

Convection structure and pattern development

For a permeability of 80 mD, the system reaches steady state at t=160,000 years, which is the same as for 80 mD in Scenario 2. However this time a downwelling plume occupies the center of the domain. Figure 5.11 shows a vertical plane at coordinate y=2500, in which 2 fully-developed upwelling plumes are seen, corresponding to 6 cells of convective motion. The average width of the cells is 700m. For a permeability of 100 mD, an upwelling plume is appears in the middle of the domain again, once the system reaches steady state at t=158,000 years. For both 80 mD and 100 mD, the fluid velocity is between $5x10^{-7}$ and $1x10^{-6}$ ms^{-1}.

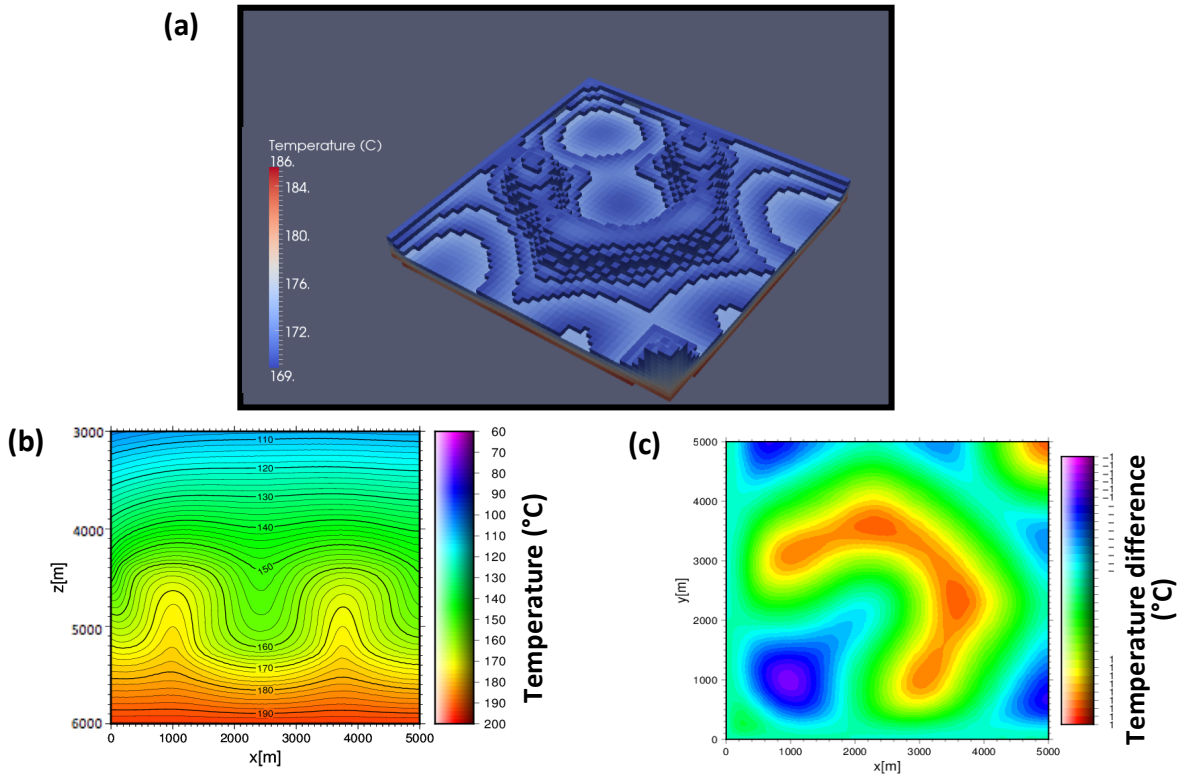

Figure 5.11: Results for 80 mD at the end of simulation (t=200,000 years). **(a)** Temperature distribution in 3D **(b)** Temperature slice of the vertical plane at coordinate y=2500 m **(c)** Temperature difference at mid-depth of the permeable layer (z=4800 m).

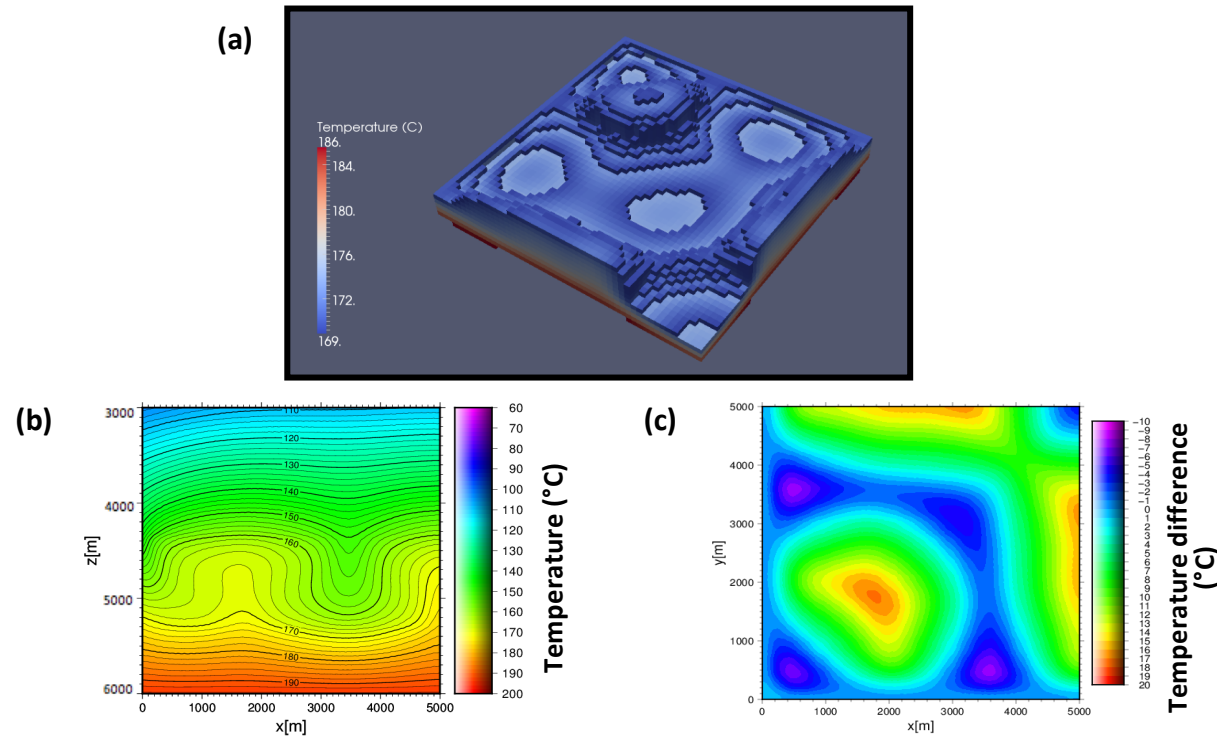

Figure 5.12: Results for 100mD at the end of simulation (t=200,000 years). **(a)** Temperature distribution in 3D **(b)** Temperature slice of the vertical plane at coordinate y=2500 m **(c)** Temperature difference at mid-depth of the permeable layer (z=4800 m).

5.3.3 H=1200 m

When the thickness of the permeable layer increases to 1200 m, the system becomes dominated by a single structure of a single upwelling plume, surrounded by downwelling plumes. Figures 5.13 and 5.14 show the results for a permeabilty of 80 mD and 100 mD, respectively. For 80 mD permeability, the convection cell shape is characterized by an elongate upwelling, with three downwellings surrounding it (Figure 5.13a). The elongate shape disappears when the permeability is increased to 100 mD, at which point the shape is characterized by 3D polyheral cells, rather than elongate cells. Steady state convection is reached t=110,000 years and t=105,000 years for 80 and 100 mD permeability, respectively. For both cases, fluid velocity is between $1x10^{-7}$ and $9x10^{-7}$ ms^{-1}.

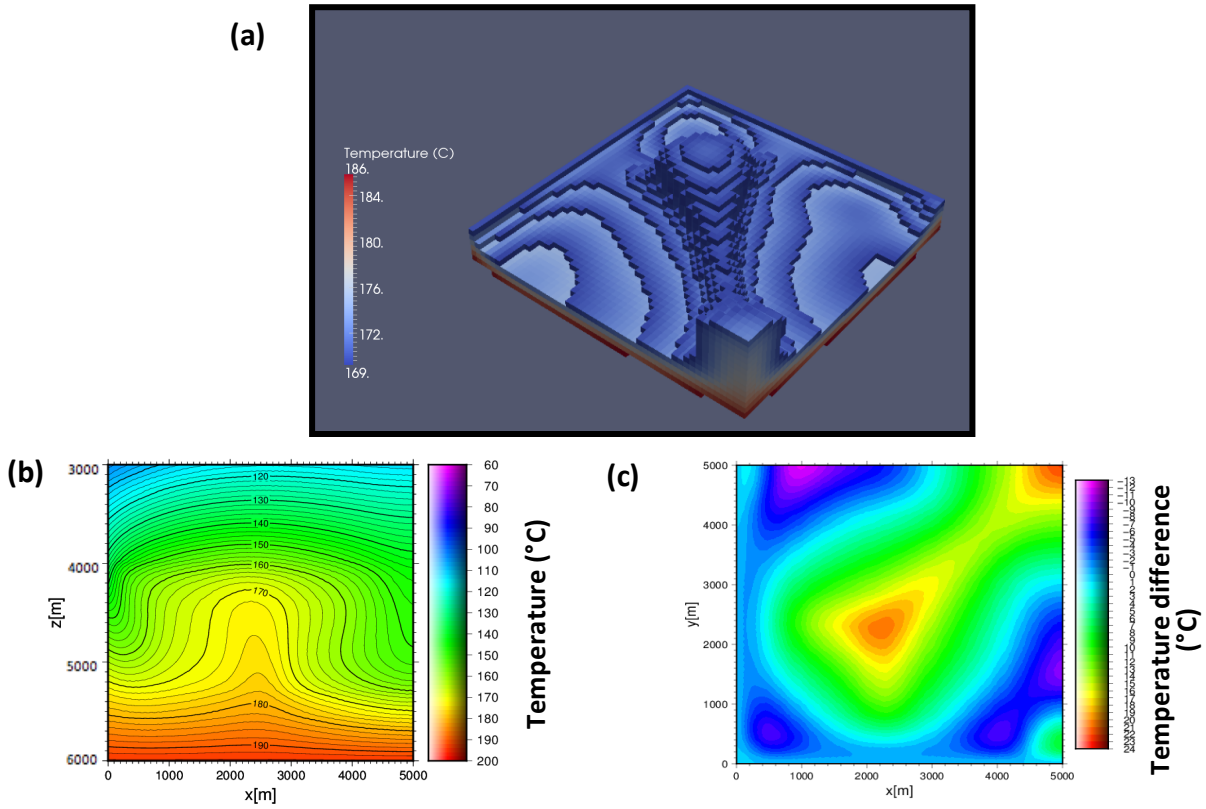

Figure 5.13: Results for 80 mD at the end of simulation (t=200,000 years). **(a)** Temperature distribution in 3D **(b)** Temperature slice of the vertical plane at coordinate y=2500 m **(c)** Temperature difference at mid-depth of the permeable layer (z=4800 m).

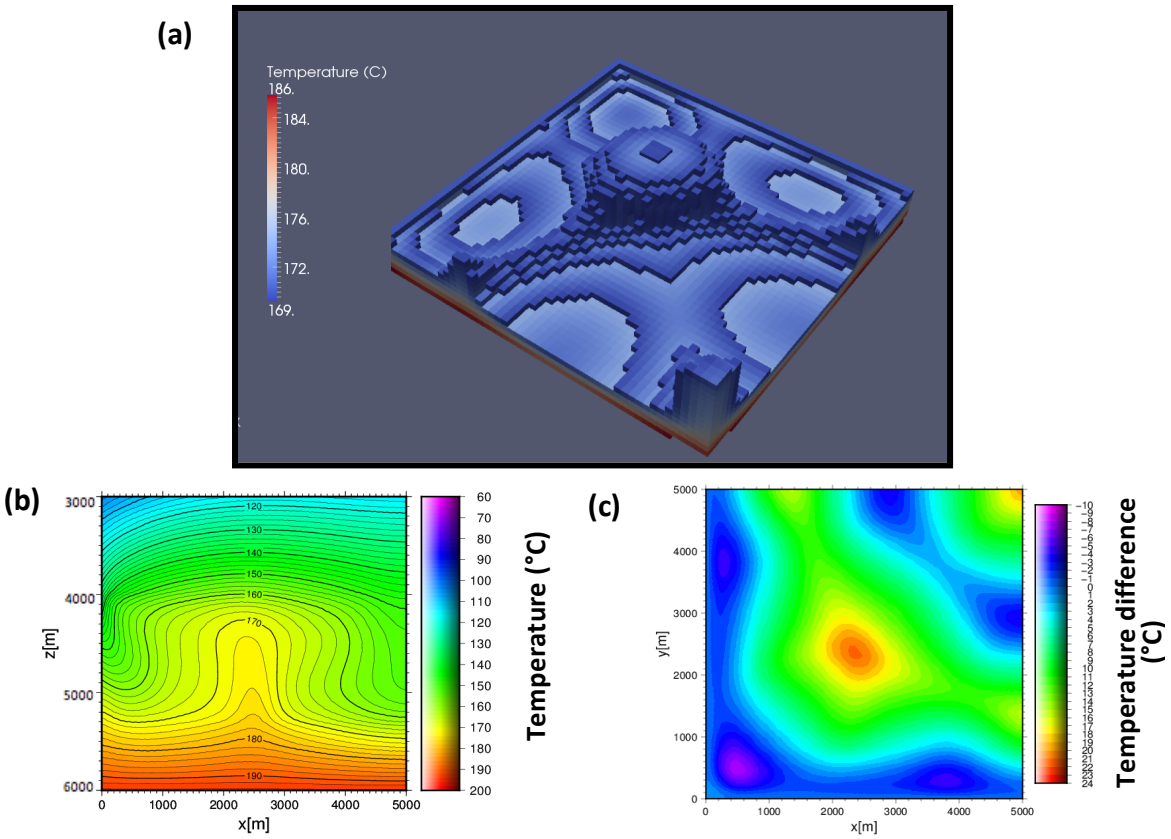

Figure 5.14: Results for 100 mD at the end of simulation (t=200,000 years). **(a)** Temperature distribution in 3D **(b)** Temperature slice of the vertical plane at coordinate y=2500 m **(c)** Temperature difference at mid-depth of the permeable layer (z=4800 m).

5.3.4 Temperature distribution for both H=900 m and H=1200 m

The geothermal gradient has been determined for each case of permeability and layer thickness. The results for 80 mD are compared in Figure 5.15a and 100 mD in Figure 5.15b. As one may predict, when the layer thickness is 1200 m, the maximum deviation of the slope from linear occurs at the shallowest depth. This occurs at the top of the layer at a depth of 4000 m (+15.0°C). For a layer thickness of 900 m, a maximum positive deviation of +12.0°C is observed at the top of the permeable layer at a depth of 4300 m. Increasing the layer thickness appears to effect the positive deviation above the permeable layer greater than the negative deviation observed at the base of the layer. A similar trend is seen when the permeability is 100 mD, where a positive deviation of +17.4°C is seen at 4000 m for H=1200m and a deviation of +13.4°C at 4300 m for H=900 m.

Tables 5.7 and 5.8 list the temperature change and resulting gradient for 80 mD and 100 mD, respectively.

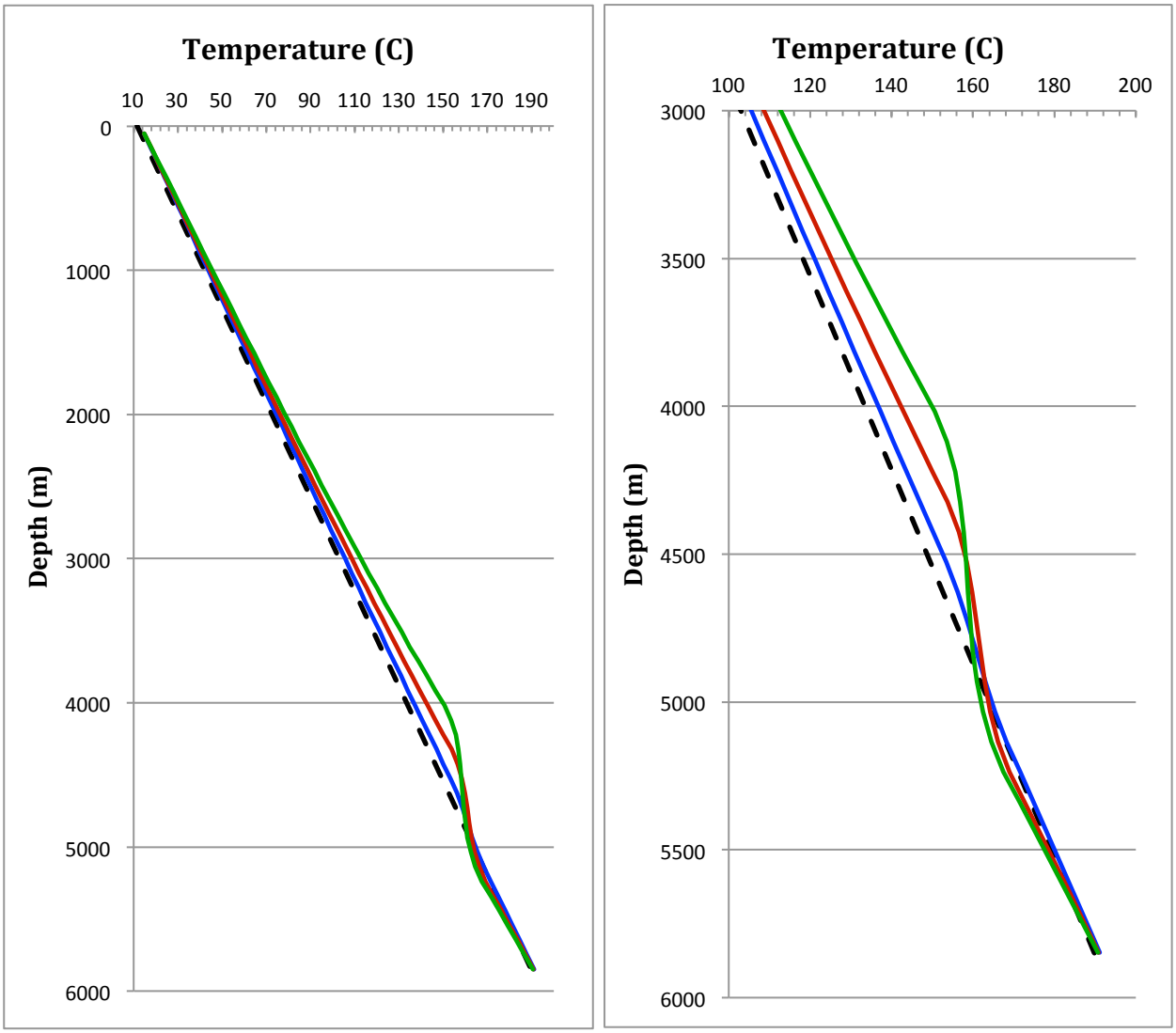

Figure 5.15: Temperature vs. depth for modelled temperature for 80 mD for H=600m (blue line), H=900m (red line) and H=1200m (green line). The linear gradient has been added for comparison (black dashed line).

Table 5.7: Modelled temperature change and resulting geothermal gradient within the permeable layer for 60 – 100 mD permeability.

Thickness	Temperature change	Temperature gradient
H=900	15 °C	16 °C/km
H=1200	16.7 °C	14 °C/km

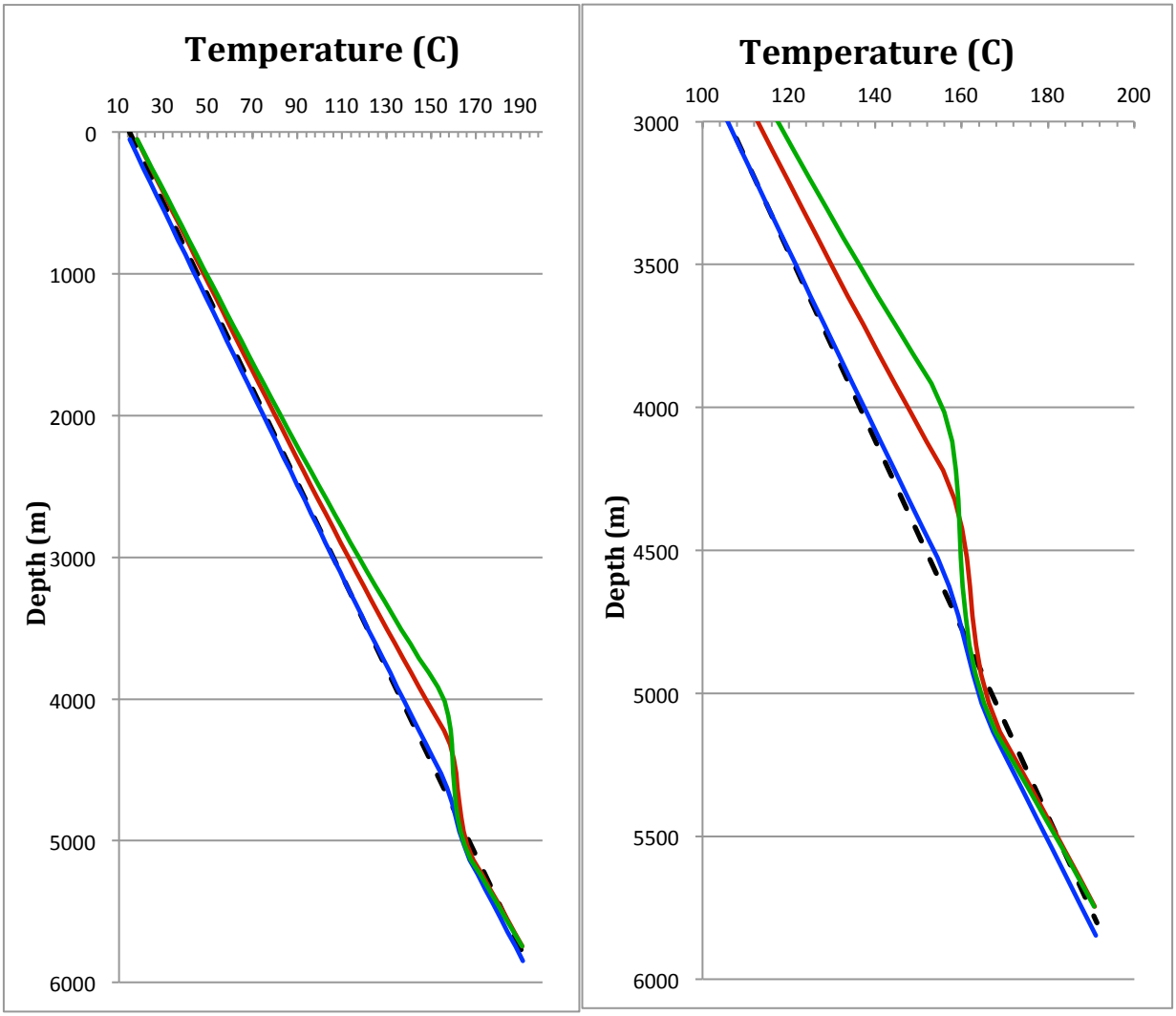

Figure 5.16: Temperature vs. depth for modelled temperature for 80 mD for H=600m (blue line), H=900m (red line) and H=1200m (green line). The linear gradient has been added for comparison (black dashed line).

Table 5.8: Modelled temperature change and resulting geothermal gradient within the permeable layer for 100 mD permeability.

Permeability	Temperature change	Temperature gradient
H=900	14.8 °C	12 °C/km
H=1200	13 °C	14 °C/km

5.4 Summary

- A range of permeability values corresponding to Rayleigh numbers ranging from $4\pi^2$ to 360, dependent on the specific scenario, were modelled. The theoretical Ra* for each scenario was shown to be an accurate approximation, as models agree with predicted conditions for the onset of convection.
- The maximum fluid velocity obtained determines if the convective system is stable. For all scenarios and permeabilities tested, the maximum fluid velocity obtained is on the order of 10^{-7} ms^{-1}.
- Increasing the geothermal gradient results in very similar convective cell patterns; however, higher temperatures are reached at shallower depths for higher geothermal gradients (i.e. when the gradient is equal to 39°C/km vs. 36°C/km).
- Comparing steady state isotherms for a range of permeability values, for example in scenario 1, it is seen that when Ra<Ra* isotherms remain straight and the system is stable with no convection cells present. When Ra=43 (k=60 mD), the system is unstable with isotherms of sinusoidal-like form. When Ra=71 (k=80 mD), the waves become flattened at the upper and lower boundaries. A further increase in the system Ra results in some isotherms that turn back upon themselves. Therefore, increasing the system Ra leads to increasing high concentration isotherms along some parts of the upper and lower boundaries.

6. DISCUSSION

This study focuses on thermal convection within deeply buried carbonates and the interplay between thermal anomalies, geological structures and convective fluid flow. This chapter combines the results from all model scenarios to assess the geothermal reservoir potential of the Luttelgeest carbonate platform.

6.1 Summary

First, this study highlights the thermal anomaly uncovered at the Luttelgeest-01 well by Bonté et al. (2012) and discusses subsequent studies by van Oversteeg (2013) who constrained the permeability of a 600 m interval of Dinantian carbonates encountered at a depth of 4500 m. Horner corrected temperatures determined by van Oversteeg (2013) reveals a 12°C temperature change (191 – 203°C) between the top and bottom of the 600 m interval (4550 – 5150 m) and a temperature gradient of 20°C/km across the permeable carbonate layer.

The numerical model results presented in the *Results* section highlight some important aspects of convection in the Dinantian carbonate platform encountered at Luttelgeest. First, the results confirm that analytical considerations provide a useful first approximation of the convection cell width as a function of thickness. Second, the temperature enhancement that occurs in convective upwellings is critically dependent on the aquifer thickness and geothermal gradient (Table 6.1). The model results indicate that at 4500 m, the temperature that can be attained in convective upwellings is much lower when the aquifer is thinner (see scenario 1 and scenario 3). Overall, a higher geothermal gradient results in a higher temperature at 4500 m, versus when the aquifer thickness is increased (see scenario 2 and 3). Convective fluid flow cannot raise the temperature within the aquifer above that at the base of the aquifer.

Table 6.1: Summary of numerical model results at the end of simulation. T_c is the temperature without convection.

Scenario	Permeability	Max T (°C) at 4500 m	T – T_c (°C) at 4500 m
1 (Gradient = 31°C/km) (Thickness = 600 m)	80 mD	158	11
	100 mD	160	13
2a (Gradient = 36°C/km)	80 mD	187	40
	100 mD	189	42
2b (Gradient = 39°C/km)	80 mD	200	53
	100 mD	203	56
3a (Thickness = 900 m)	80 mD	171	24
	100 mD	174	27
3b (Thickness = 1200 m)	80 mD	177	30
	100 mD	181	34

6.1.1 Effects of permeability

In general, as the permeability increases there is a decrease in lateral width of upwellings, thus they become more focused. Downwellings become more diffused, showing an increase in lateral width. Guillou-Frottier et al. (2013) show a similar result when incorporating a decreasing permeability with depth. They find that a greater decrease in permeability with depth results in a larger lateral width of downwellings and smaller lateral width of upwellings. In this study, it is found that a downwelling plume first appears at the point of perturbation, and continues to show a deeper overall penetration within the layer. Overall, upwellings become less numerous with increasing permeability, and downwellings contain the most volume (Guillou-Frottier et al., 2013).

More realistic conditions in the modeling could have involved (1) decreasing permeability with depth and (2) lateral variations of permeability over short distances. However, for a relatively thin layer of 600 m incorporating a decrease in permeability with depth should have a minimal affect on the convective cell structure in comparison to the models by Guillou-Frottier et al. (2013), which considered a much thicker aquifer (greater than 4000 m).

6.1.2 Rayleigh number analyses

The onset of convection can be expected to occur above some critical value of the Rayleigh number, however it can vary due to permeability, thickness and geothermal gradient of a layer. A main limitation of Rayleigh analyses is that natural systems have variable properties, both in space and time. Average or representative values for heterogeneous parameters in Rayleigh number calculations are commonly used, a sufficient estimation so long that the actual range does not exceed more than one order of magnitude (Nield, 1994).

Moreover, a critical Rayleigh number applies to a specific set of conditions, including initial and boundary conditions and the geometry of layer. This study assumes the carbonate platform is uniformly heated from below and is a perfect conductor. Changing the lower thermal boundary condition may result in smaller values for the critical Rayleigh number. The same applies if the upper thermal boundary is chosen to be a perfect insulator, which would result in a critical Rayleigh number of 27 as opposed to 40 (Bjorlkykke et al., 1988). Also, conductive heat transfer along the sides of the platform is likely to play a role in the overall physical state and stability of the convective system. Murphy (1979) highlighted on the fact that heat transfer between fluid in the permeable layer and surrounding rock is extremely stabilizing. Tournier et al. (2000) demonstrated that this blanketing effect of thermal gradients across vertical walls by conduction might result in delayed onset of convection. Though the suggestions of both Murphy (1979) and Tournier et al. (2000) were related to studies of the onset of convection in vertical fault planes, the concept can apply to any confined, fluid saturated medium where convective fluid flow is taking place. Thus, assuming that only convective heat transfer is occurring in the system is a significant simplification to the model. Yang et al. (1998) simulated hydrothermal circulation in discretely fractured

porous media and found that fractures can stimulate and maintain hydrothermal convection even if the Rayleigh number is less than its critical value.

Overall, the Rayleigh number analysis in this study ignored several important considerations, such as salinity effects on water density and viscosity. Furthermore, fluid parameters were determined based on the temperature of the layer at mid-depth, and therefore the Rayleigh number of the system as well as the minimum permeability required for the onset of convection should be considered an approximation. Considering the number of factors overlooked during the Rayleigh number analysis, numerical simulations were still able to come within 5-10 mD of the theoretical minimum permeability calculated for each scenario. Therefore, it is important to keep in mind that theoretical analyses of convection such as the use of the critical Rayleigh number comes with many assumptions, however it does provide useful information about the likelihood of convection in the Dinantian carbonates encountered at LTG-01.

6.1.3 Convection cell structure

The development and number of convection cells is very much a time dependent process. As shown by all model results, many convection cells may develop initially but gradually converge until steady state convection is reached. Three-dimensional convective patterns and preferred convective wavelengths are highly sensitive to lateral dimensions of the permeable zone. Three-dimensional modelling reveals new fluid patterns that are not observable in two dimensions, such as the occurrence of hexagonal type convection patterns and complex 3D polyhedral shapes. Furthermore, Harcouet-menou et al. (2009) and Zhao et al. (2003) demonstrate that the occurrence probability of two- and three- dimensional convective regimes is about the same.

Though this study does not focus on convection within vertical faults, it is still important to remember that the presence of fault zones can alter the convection cell geometry and flow rates by constraining the zones of upwellings and downwellings. Basal heat flow and the physical properties of fault zones largely control the pattern and sense of circulation of fault bounded convective flow. The direction of circulation of a convection cell bounded by two faults is determined whether the system is in a critical or sub-critical condition. Simms et al. (2004) investigated the effects of fault properties on convective flow, and concluded that longer flow paths and higher flow rates increase the effectiveness of convection as a mechanism of heat and mass transport. Yang et al. (1998) showed that the in a closed system, the overall vigor of convection and the cell pattern development is highly dependent on the placement of a single vertical fracture.

6.1.4 Temperature patterns

Horner corrected temperatures by van Oversteeg (2013) reveals a 12°C temperature change (191 – 203°C) between the top and bottom of the 600 m interval (4550 – 5150 m) and a

temperature gradient of 20°C/km across the permeable carbonate layer. In scenario 1 – wherein the geothermal gradient is 31°C/km and the thickness of the layer is 600 m – modeled temperatures show a best fit to Luttelgeest when the permeability is 100 mD. In this case, a temperature change of 12.9°C and a temperature gradient of 21°C/km is observed across the layer. However, modeled temperatures for 100 mD permeability are significantly lower than seen at Luttelgeest, only reaching a maximum temperature of 169°C at the base of the permeable layer (5150 m).

In scenario 2 for the case of 36°C/km, modeled temperatures for a permeability between 80 and 100 mD show the best fit to Luttelgeest. For 80 mD a temperature change of 13.4°C and temperature gradient across the layer of 22°C/km is observed, while for 100 mD a temperature change of 11.9°C and a gradient of 20°C/km is observed. Again, the modeled temperatures are lower than seen at Luttelgeest, but the maximum temperature at the base of the layer is closer to Luttelgeest, 195°C. For a gradient of 39°C/km, modeled temperatures have a best fit to Luttelgeest when the permeability is 80 mD, however the maximum temperature observed is slightly higher than seen at Luttelgeest, 206°C.

Going back to the Horner corrected temperatures by van Oversteeg (2013), if a thickness of 900 m is considered, the result is a 16°C temperature change (187 – 203°C) and a temperature gradient of 18°C/km across the 900 m interval. This best fits with modeled temperatures from the case of 80 mD permeability, however the maximum modeled temperature is significantly lower than seen at Luttelgeest. The same is the case for a layer with thickness of 1200m. Modeled temperatures still remain significantly lower than observed at Luttelgeest.

It is known that in upwelling regions the temperature gradient changes from steep to shallow with increasing depth, whereas in downwelling regions the gradient changes from shallow to steep. The impact of drilling into an upwelling or a downwelling is substantial – if the aim is to reach anomalously high temperatures at a relatively shallow depth, one would have to know the location of upwelling zones with respect to downwelling zones. Figures 6.1, 6.2 and 6.3 show the temperature vs. depth profiles taken above two points, A and B, in three different model scenarios. In each example point A is located along the axis of a hot upwelling plume and point C is located along the axis of a downwelling plume. Overall, the best fit of modeled temperatures to Luttelgeest occurs when a temperature gradient of 39°C/km, an aquifer thickness of 600 m and a permeability of 80 mD (7.89×10^{-14}) are applied. To exemplify this, Figure 6.4 shows the profiles for temperature versus depth taken above three points, where point A is located along the axis of a hot upwelling plume, point B is located at the vertical of the mixing zone between discharge and recharge flows and point C is located along the axis of downwelling plume. Comparison of the geothermal profiles A, B and C with the temperature observed at Luttelgeest (black dashed line in Figure 6.4) suggests that modeled temperatures could very well represent actual conditions at Luttelgeest, as LTG-01 well was drilled in one location and therefore only shows the profile of temperature versus depth at

one point within the Luttelgeest carbonate platform.

Referring back to Figure 3.7, which shows a seismic profile of the Luttelgeest carbonate platform, it is seen that the LTG-01 well is located at the edge of the platform. This study considers a rather simple model to represent the carbonate platform encountered at LTG-01. Rarely are sedimentary units perfectly horizontal. Zhao et al. (2003) investigated the convective instability in inclined fluid saturated 3D fault zones and found that the overall shape of the inclined 3D fault zone may affect convective instability of the system. Assuming the height of the fault zone as the characteristic length of the system, a decrease in the inclined angle will reduce the possibility of convective flow to take place. Therefore, it has a stabilizing effect. This is important to remember for the case of Luttelgeest, as the convective cell structure may also be affected by the inclined boundaries of the platform. That said, the models produced here are a good first approximation of what the structure would look like, given a specific thickness, permeability and geothermal gradient.

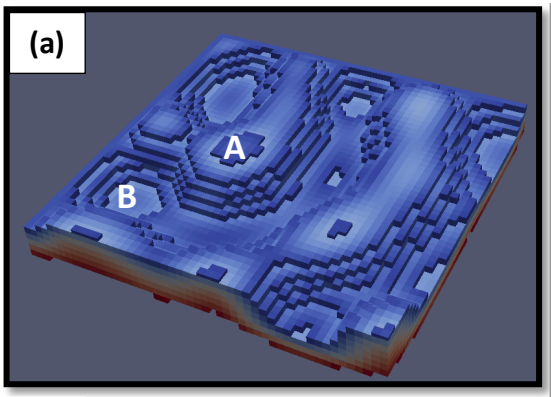

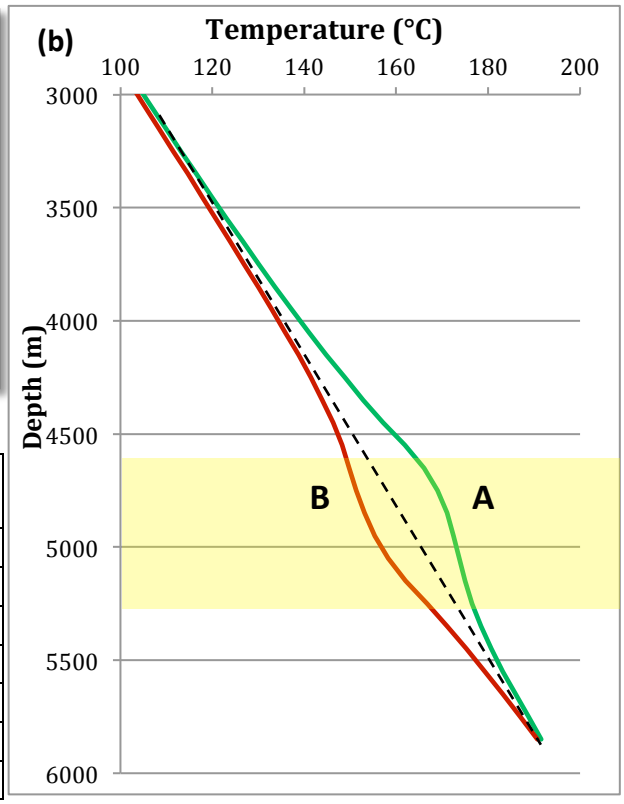

(c)

Depth (m)	Temp (°C) Point A	Temp (°C) Point B
4600	161	148
4700	165	149
4800	169	151
4900	171	153
5000	172	155
5100	173	158
5200	174	162

Figure 6.1: Scenario 1, where the permeability is 100 mD, geothermal gradient is 31°C/km and aquifer thickness is 600 m **(a)** Location of points A and B. **(b)** Profiles of temperature versus depth for each point. The black dashed line represents the linear gradient of 31°C/km for comparison **(c)** Modelled temperatures within the permeable layer for points A and B.

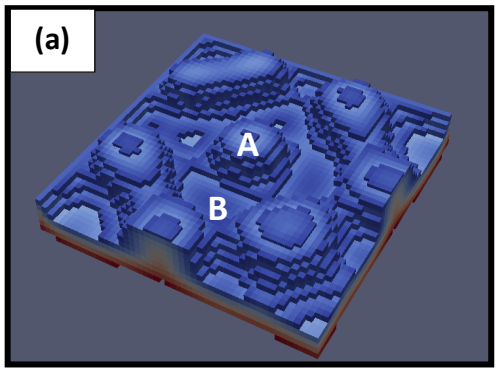

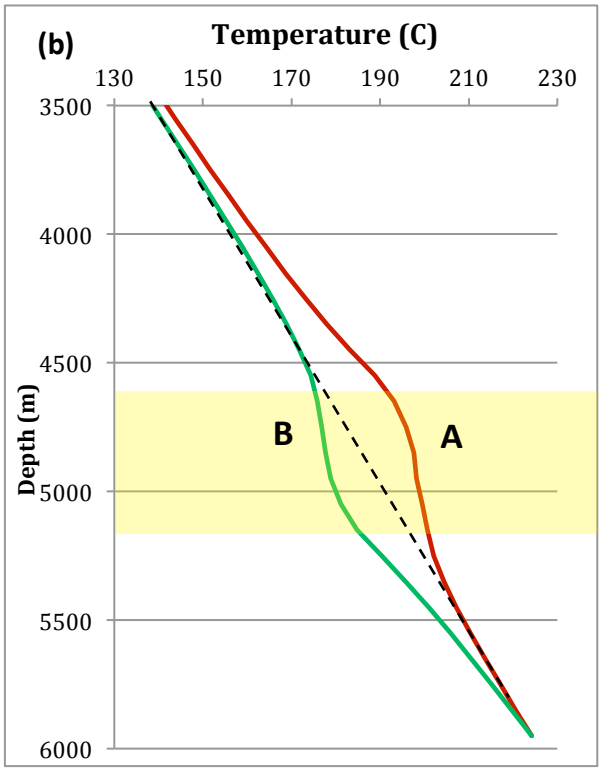

(c)

Depth (m)	Temp (°C) Point A	Temp (°C) Point B
4600	188	174
4700	193	175
4800	196	176
4900	197	177
5000	198	179
5100	199	181
5200	200	185

Figure 6.2: Scenario 2, where the permeability is 100 mD, geothermal gradient is 36°C/km and aquifer thickness is 600 m **(a)** Location of points A and B. **(b)** Profiles of temperature versus depth for each point. The black dashed line represents the linear gradient of 39°C/km for comparison **(c)** Modelled temperatures within the permeable layer for points A and B.

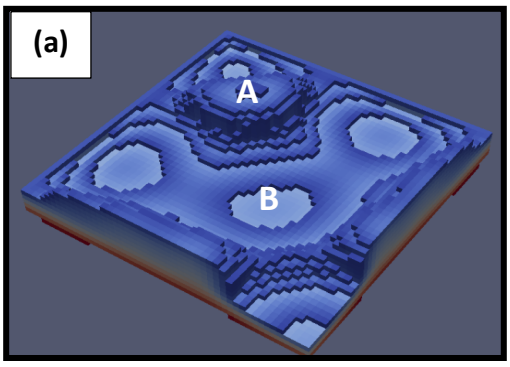

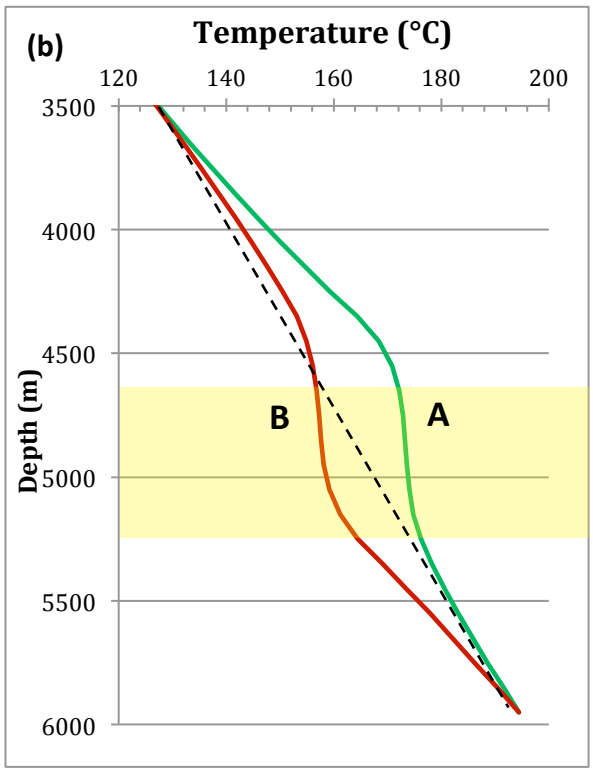

(c)

Depth (m)	Temp (°C) Point A	Temp (°C) Point B
4600	170	156
4700	172	156
4800	172	157
4900	173	157
5000	173	158
5100	174	159
5200	174	161

Figure 6.3: Scenario 3, where the permeability is 100 mD, geothermal gradient is 31°C/km and aquifer thickness is 900 m **(a)** Location of points A and B. **(b)** Profiles of temperature versus depth for each point. The black dashed line represents the linear gradient of 31°C/km for comparison **(c)** Modelled temperatures within the permeable layer for points A and B.

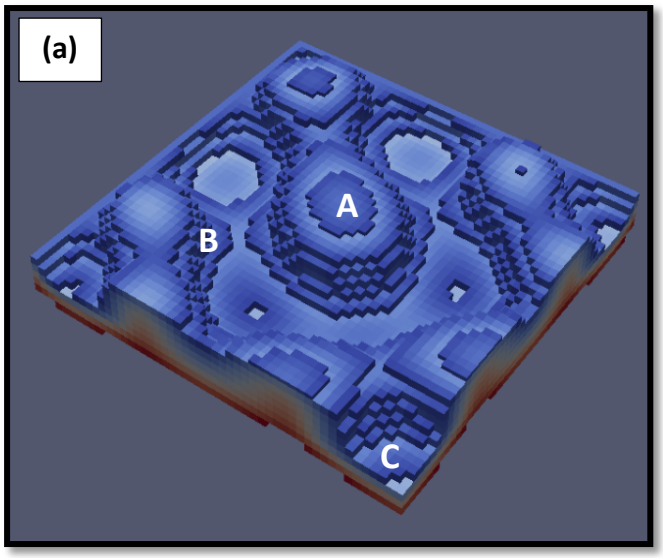

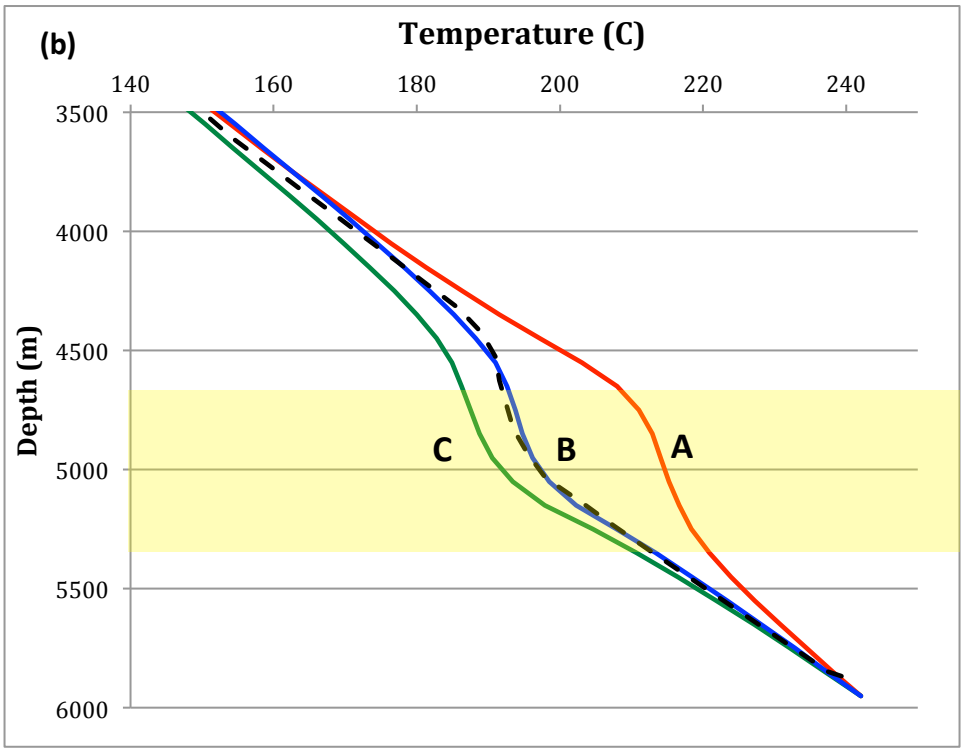

(c)

Depth (m)	Temperature (°C) Point A	Temperature (°C) Point B	Temperature (°C) Point C
4600	203	191	185
4700	208	193	186
4800	211	194	187
4900	213	195	189
5000	214	196	190
5100	215	198	193
5200	217	202	198

Figure 6.4: Scenario 2, where the permeability is 80 mD, geothermal gradient is 39°C/km and aquifer thickness is 600 m **(a)** Location of points A, B and C. **(b)** Profiles of temperature versus depth for each point. The black dashed line represents the actual conditions measured at Luttelgeest **(c)** Modelled temperatures within the permeable layer for points A, B and C.

6.2 Pseudo conductivity for the permeable layer

The estimated heat-flow value at the bottom of the formation and the thermal conductivities of the rock layers above and below the permeable layer can be used to determine a 'pseudo conductivity' for the 600 m permeable layer itself. Bonté et al. (2012) presents a temperature-depth profile for Luttelgeest-01 well using a heat flow of approximately 56 mW/m^2. This value can be used to determine 'pseudo-conductivity' for the 600 m permeable layer considered in this study. The best-fit model determined in the previous section (a geothermal gradient of 39°C/km and a thickness of 600 m) is used to determine the pseudo-conductivity. Using equation 3.1 in section 3.2, a heat flow of 56 mW/m^2 and a temperature change of 15°C within a 600 meter interval (gradient of 21.4°C/km) results in a pseudo-conductivity of 2.61 W/m/K. In Figure 6.3, black dashed lines indicate the convective segment for which this pseudo-conductivity relates to

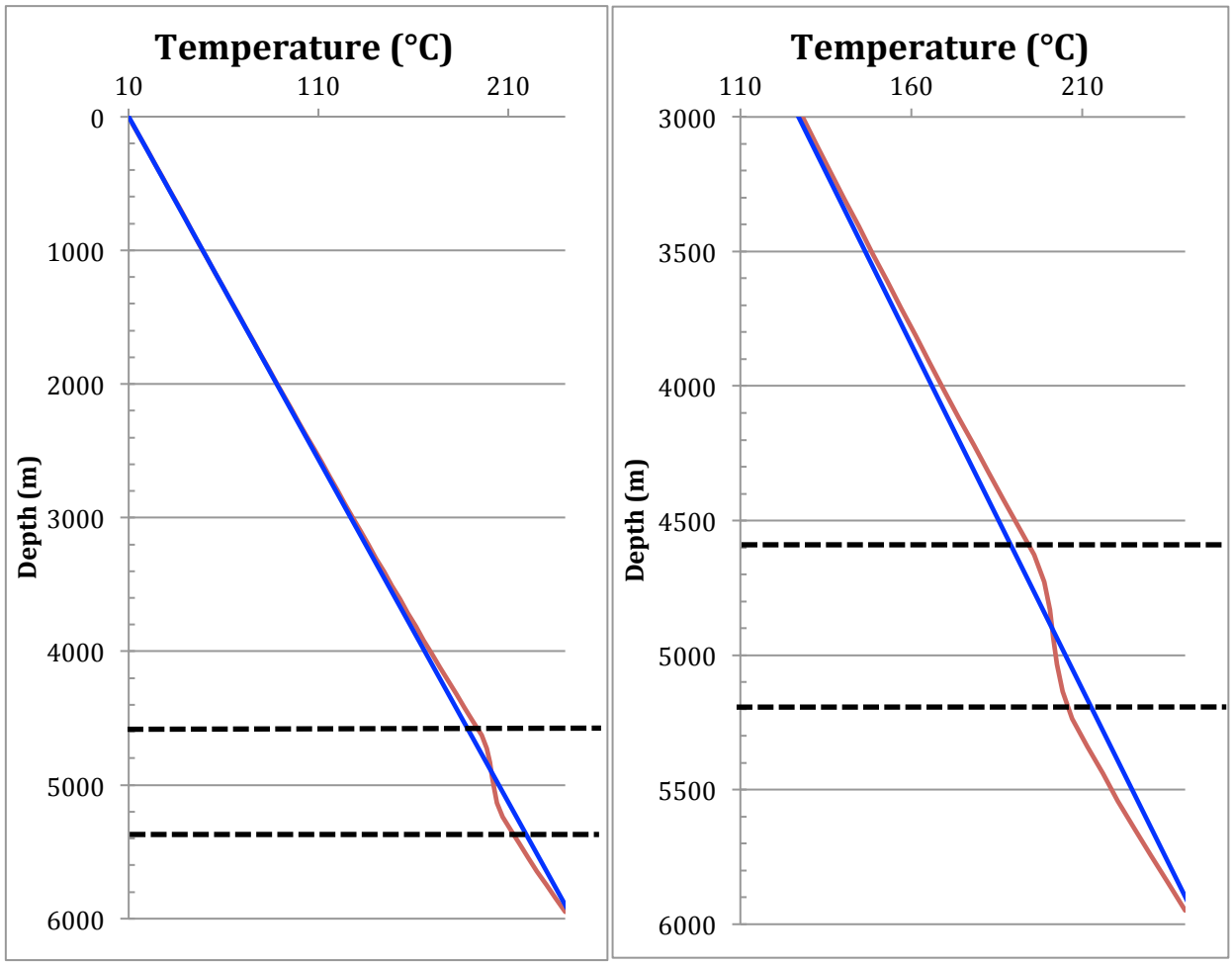

Figure 6.3: Pseudo-conductivity measured for the zone confined by the dashed black lines (the convecting layer).

6.3 Heat flow

A simulation was carried out for a thickness of 600 m for t=1,000,000 years. This was done in order to (1) determine whether convection cells remain stationary once the system has reached steady state and (2) assess the propagation of heat flow from the top of the central upwelling plume to determine the distance travelled over a characteristic time (i.e. 1,000,000 years). Results reveal that once cells have been built they remain stationary for the remainder of simulation time. To assess the propagation of heat, thermal diffusivity must first be defined. Thermal diffusivity is calculated using the following equation:

$$\kappa = \frac{\lambda}{\rho C_p}$$

where λ is the thermal conductivity, ρ is the density and C_p is the specific heat capacity. Dimensional analysis of the diffusion equation shows that the diffusivity κ has the dimension of length^2 x time^{-1}. The diffusion length L can be defined as:

$$L = \sqrt{\kappa\tau}$$

If the temperature change occurs at some time t_0, then after a characteristic time interval τ it will have propagated over a distance $L = \sqrt{\kappa\tau}$ through the medium with diffusivity κ. Similarly, it takes τ^2/κ for a temperature change to propagate over a distance L.

Given a conductivity of 2.61 W/m/K, a density of 886 kg/m^3 and a specific heat capacity of 4497 J/kg/K, the resulting thermal diffusivity is 6.7x10^{-7} m^2/s. Over a time of 1 million years, the heat propagates upwards from the top of the upwelling plumes over a distance of 4594 meters. In 2 million years, this distance increases to 6507 meters.

7. CONCLUSION

The Dinantian carbonates encountered at the Luttelgeest-01 Well in the Noordoostpolder contains intervals of relatively high fracture permeability showing potential as a geothermal reservoir for electricity production in the Netherlands. Temperature measurements indicate variations in subsurface temperature that could be indicative of convection. This is important, as convection creates areas where the temperature is anomalously high at shallow depths.

This study has focused on assessing the potential for convection within a 600 m fractured interval within the Luttelgeest carbonate platform, by calculating the minimum permeability required for convection based on Rayleigh number analysis, and performing numerical simulations based on representative parameter values for this particular fractured interval. Numerical experiments presented in section 5 give insights on the possible flow and thermal structures within this 600 m fractured interval. Models show that the spacing of convective upwellings, and therefore the spacing of thermal anomalies, can be predicted theoretically by knowing the aquifer thickness and the permeability. It is important to remember that in natural systems, the shape and location of upwellings is likely to be controlled by the geometric aspects of the carbonate platform itself, as well as the fracture network geometry within the aquifer.

Thermal anomalies due to convection can be significant. Given a geothermal gradient of 39°C/km and an aquifer thickness of 600 m, a temperature of 203°C can be obtained at a depth of 4500 m above upwelling zones. Contrarily, downwelling zones result in a temperature of 185°C at the same depth. Hence, locating convective upwellings is a potentially good strategy for geothermal exploration (Sheldon et al., 2012). The economic viability of exploiting an upwelling is dependent on its size as well as several other factors. The temperature that can be obtained in an upwelling zone is limited by the temperature at the bottom of the aquifer, and thus by its depth. Constraining the precise thickness of the fractured interval within the carbonate platform that is host to convective fluid flow is critical.

Further work is required to test the validity of the assumptions that the behaviour a heterogeneous aquifer is adequately represented by treating it as a homogeneous layer with constant horizontal and vertical values of permeability. Future numerical models could consider a more detailed permeability structure to simulate convection.

ACKNOWLEDGEMENTS

First and foremost, I would like to thank Jan-Diederik for giving me the opportunity to be part of such an exceptional and dedicated team of geo-scientists at TNO. Thank you for your supervision and your enthusiasm. I would like to give a special thanks to Maarten for his willingness to help me with all things Java and Eclipse. Maarten, you have definitely played the role of a supervisor during this last year and for that I thank you! I would also like to thank Sierd and Chris for their guidance during my two years at Utrecht University.

Of the 24 months I have lived in the Netherlands, I am lucky enough to get to say that I have spent 18 of those months at TNO. Not only have I met so many incredible people, but I have also been fortunate enough to develop valuable friendships. There is one person in particular who has made my time at TNO exceptionally memorable: my life coach, Mart Zijp. Mart – thank you for putting up with my nonsense, for always encouraging me to keep going and for always putting a smile on my face. You are a great friend, and I will miss seeing you around the office every day. I would also like to give a very special thanks to my wonderful geochem ladies (and Jens!) of room 2.053. Mariella, Laura, Svenja, Tanya and Jens – you all have been my support, especially during these last few months. No matter how tough things got I could always count on you all to make me laugh. And you did. Thank you for making each and every day great. Finally, I would like to thank Wendy and Sacha for always helping me out at TNO (not to mention for always providing chocolate at the most crucial times!)

There are also a number of important people outside of TNO and Utrecht University who have made my two years in the Netherlands unforgettable. Lisanne, Marjan, Jan and Paddy – thank you for the great times we've had. I would like to thank my lovely parents for their support from half way around the world! I can't thank you enough for all the hours and hours you've spent on Skype with me. I love you both dearly! Last but not least, I would like to thank my Dutch family, Casa Normandie, for helping me settle into my new life here in the Netherlands. I am the luckiest person in the world to have such an amazing group of housemates that I can call family. Daan, Jorien, Koos and Martijn – I love you all!

REFERENCES

Agosta, F., Alessandroni, M., Antonellini, M., Tondi, E. & Giorgioni, M., 2010. From fractures to flow: A field-based quantitative analysis of an outcropping carbonate reservoir. *Tectonophysics* 490: 197-213.

Bächler, D., Kohl, T. & Rybach, L., 2003. Impact of graben-parallel faults on hydrothermal convection – Rhine Graben case study. *Physics and Chemistry of the Earth* 28: 431-441.

Baillieuz, P., Schill, E. & Dezayes, C., 2011. 3D Structural regional model of the EGS Soultz site (Northern Upper Rhine Graben, France): Insights and perspectives. *Proceedings: Thirty-sixth Workshop on Geothermal Reservoir Engineering*, January 31 – February 2, 2011, Stanford University, Stanford, California.

Bataille, A., Genthon, P., Rabinowicz, M. & Fritz, B., 2006. Modeling the coupling between free and forced convection in a vertical permeable slot: Implications for heat production of an Enhanced Geothermal System. *Geothermics* 35: 654-682.

Bense, V.F., Gleeson, T., Loveless, S.E., Bour, O. & Scibek, J., 2013. Fault zone hydrogeology. *Earth-Science Reviews* 127: 171-192.

Berkowitz, B., 2002. Characterizing flow and transport in fractured geological media: A review. *Advances in Water Resources* 25: 861-884.

Bjørlykke, K., Mo, A. & Palm, E., 1988. Modelling of thermal convection in sedimentary basins and its relevance to diagenetic reactions. *Marine and Petroleum Geology* 5: 338-351.

Bonté, D., Van Wees, J.D. & Verweij, J.M.: Subsurface temperatures of the onshore Netherlands: new temperature dataset and modelling, *Netherlands Journal of Geosciences-Geologie en Mijnbouw,* 91(4), (2012), 491-515.

Cacace, M., Blocher, G., Watanabe, N., Moeck, I., Borsing, N., Scheck-Wenderoth, M., Kolditz, O., Huenges, E., 2013. Modelling of fractured carbonate reservoirs: outline of a novel technique via a case study from the Molasse Basin, southern Bavaria, Germany. *Enviornmental Earth Science* 70 (8): 3585-3602.

Caine, J.S, Evans, J.P. & Forster, C.B., 1996. Fault zone architecture and permeability structure. *Geology* 24: 1025-1028.

De Dreuzy, J.R., Davy, P. & Bour, O., 2001. Hydraulic properties of two-dimensional random fracture networks following a power law length distribution 1. Effective connectivity. *Water Resources Research* 37 (8): 2065-2078.

DiPippo, R., 2012. Geothermal power plants: principles, applications, case studies and

environmental impact. 600 pp. , Butterworth-Heinemann, Amsterdam.

EBN, 2013. Exploring Dinantian carbonates in the Dutch subsurface – from tombstone to cave, presented by B. Jaarsma at PGK meeting 18 September, available online at: http://www.ebn.nl/Actueel/Documents/130918_Dinantian_carbonates_play_review_presentation.pdf

Evans, J.P., Forster, C.B. & Goddard, J.V., 1997. Permeability of fault-related rocks, and implications for hydraulic structure of fault zones.

Faulkner, D.R., Lewis, A.C. & Rutter, E.H., 2003. On the internal structure and mechanics of large strike-slip fault zones: field observations of the Carboneras fault in south-eastern Spain. *Tectonophysics* 367: 235-251.

Faulkner, D. R., Jackson, C. A. L., Lunn R. J., Schlische, R. W., Shipton, Z. K, Wibberley, C. A. J. & Withjack M. O., 2010. A review of recent developments concerning the structure, mechanics and fluid flow properties of fault zones. *Journal of Structural Geology* 32: 1557-1575.

Garibaldi, C., Guillou-Frottier, L., Lardeaux, J.M. & Bouchot, V., 2010. Combination of Numerical Tools to Link Deep Temperatures, Geological Structures and Fluid Flow in Sedimentary Basins: Application to the Thermal Anomalies of the Provence Basin (South-East France). *Proceedings*, World Geothermal Congress 2010, Bali, Indonesia.

Guillou-Frottier, L., Carre, C., Bourgine, B., Bouchot, V. & Genter, A., 2013. Structure of hydrothermal convection in the Upper Rhine Graben as inferred from corrected temperature data and basin-scale numerical models. *Journal of Volcanology and Geothermal Research* 256: 29-49.

Haffen, S., Geraud, Y., Diraison, M. & Dezayes, C., 2013. Fluid-flow zones in a geothermal sandstone reservoir: localization from thermal conductivity and temperature logs, borehole EPS1 (Soultz-sous-forets, France) and 3D models. *Proceedings: Thirty-Eighth Workshop on Geothermal Reservoir Engineering*, February 11-13, Stanford University, Stanford, California.

Harcouët-Menou, V., Guillou-Frottier, L., Bonneville, A., Adler, P.M. & Mourzenko, V., 2009. Hydrothermal convection in and around mineralized fault zones: insights from two- and three-dimensional numerical modeling applied to the Ashanti belt, Ghana. *Geofluids* 9: 116-137.

Holzbecher, E. O., 1998. Modelling density-driven flow in porous media: principles, numerics, and software. Springer: Berlin, New York.

Kaiser, B.O., Cacase, M. & Scheck-Wenderoth, M., 2013. 3D coupled fluid and heat transport simulations of the Northeast German Basin and their sensitivity to the spatial

discretization: different sensitivities for different mechanisms of heat transport. *Environmental Earth Sciences* 70 (8): 3643-3659.

Kombrink, H., Leever, K. A., Van Wees, J. D., Van Bergen, F., David, P. & Wong, T. E., 2008. Late carboniferous foreland basin formation and Early Carboniferous stretching in North-western Europe: Inferences from quantitative subsidence analyses in the Netherlands. *Basin Research* 20(3): 377-395.

Lapwood, E., 1948. Convection of a fluid in a porous medium. *Proceedings of the Cambridge Philosophical Society* 44: 508-521.

Nick, H.M., Paluszny, A., Blunt, M.J. & Matthai, S.K., 2011. Role of geomechanically grown fractures on dispersive transport in heterogeneous geological formations. *Physical Review* 84: 056301.

Noack, V., Scheck-Wenderoth, M. & Cacace, M., 2012. Sensitivity of 3D thermal models to the choice of boundary conditions and thermal properties: a case study for the area of Brandenburg (NE German Basin). *Environmental Earth Science* 67 (6): 1695-1711.

Noack, V., Scheck-Wenderoth, M., Cacace, M., Schneider, M., 2013. Influence of fluid flow on the regional thermal field: results from 3D numerical modelling for the area of Brandenburg (North German Basin). *Environmental Earth Science* 70 (8): 3523-3544.

Magri, F., Akar, T., Gemici, U. & Pekdeger, A., 2010. Deep geothermal groundwater flow in the Seferihisar-Balçova area, Turkey: results from transient numerical simulations of coupled fluid flow and heat transport processes. *Geofluids* 10: 388-405.

McKibbin, R., 1986. Heat transfer in a vertically-layered porous medium heated from below. *Transport in Porous Media* 1: 361-370.

Murphy, H.D., 1979. Convective Instabilities in Vertical Fractures and Faults. *Journal of Geophysical Research* 84 (B11): 6121–6130.

Paluszny, A. & Matthai, S.K., 2010. Impact of fracture development on the effective permeability of porous rocks as determined by 2D discrete fracture growth modeling. *Journal of Geophysical Research* 115:

Pasquale, V., Chiozzi, P. & Verdoya, M., 2013. Evidence for thermal convection in the deep carbonate aquifer of the eastern sector of the Po Plain, Italy, *Tectonophysics* 594: 1-12.

Rabinowicz, M., Boulegue, J., Genthon, P., 1998. Two- and three-dimensional modelling of hydrothermal convection in the sedimented Middle Valley segment, Juan de Fuca Ridge. *Journal of Geophysical Research* 103 (B10): 24,045-24,065.

Rayleigh, L., 1916. LIX. On convection currents in a horizontal layer of fluid, when the higher

temperature is on the under side, *The London, Edinburgh and Dublin Philosophical Magazine and Journal of Science* 32(192): 529-546.

Saar, M.O., 2011 Review: Geothermal heat as a tracer of large-scale groundwater flow and as a means to determine permeability fields. *Hydrology Journal* 19: 31-52.

Sharp Jr., J.M. & Shi, M., 2009. Heterogeneity effects on possible salinity-driven free convection in low-permeability strata. *Geofluids* 9: 263-274.

Sheldon, H.A., Reid, L.B., Florio, B. & Kirkby, A.L., 2011. Convection or conduction? Interpreting temperature data from sedimentary basins. Proceedings: Australian Geothermal Energy Conference.

Sheldon, H.A., Florio, B., Trefry, M.G., Reid, L.B., Ricard, L.P, Ameed, K. & Ghori, R., 2012. The potential for convection and implications for geothermal energy in the Perth Basin, Western Australia. *hydrogeology Journal* 20: 1251-1268.

Siffert, D., Haffen, S., Garcia, M.H., Geraud, Y., 2013. Phenomenological study of temperature gradient anomalies in the Buntsandstein formation, above the Soultz geothermal reservoir, using TOUGH2 simulations. *Proceedings: Thirty-Eighth Workshop on Geothermal Reservoir Engineering*, February 11-13, Stanford University, Stanford, California.

Simms, M.A. & Garven, G., 2004. Thermal convection in faulted extensional sedimentary basins: theoretical results from finite-element modeling. *Geofluids* 2004: 109-130.

Souche, A., Dabrowski, M. & Andersen, T.B., 2014. Modeling thermal convection in supradetachment basins: example from western Norway. *Geofluids* 14: 58-74.

Tan, K.K. & Torng, S., 1999. Simulations of the onset of transient convection in porous media under fixed surface temperature boundary conditions. Proceedings: Second International Conference on CFD in the Mineral sand Process Industries: CSIRO, Melbourne, Australia.

Tester, J.W., Anderson, B.J., Batchelor, A.S., Blackwell, D.D., DiPippo, R., Drake, E.M., Garnish, J., Livesay, B., Moore, M.C., Nichols, K., Petty, S., Toksoz, M.N., Veatch, R.W., Baria, R., Augustine, C., Murphy, E., Negraru, P., Richards, M., 2007. Impact of enhanced geothermal systems on the US energy supply in the twenty first century. Philosophical Transactions of the Royal Society A, 365: 1057-1094.

Tournier, C., Genthon, P. & Rabinowicz, M., 2000. The onset of natural convection in vertical fault planes: consequences for the thermal regime in crystalline basements and for heat recovery experiments. *Geophys. J. Int* 140: 500-508.

Turcotte, D.L. & Schubert, G., 2002. Geodynamics, 456 pp., Cambridge University Press, Cambridge, New York.

Van Hulten F.F.N., 2012. Devono-carboniferous carbonate platform systems of The Netherlands. *Geologica Belgica* 15(4): 284-296.

Van Oversteeg, J.K., 2013. Thermal Convection Related to Fracture Permeability in a Dinantian Carbonate Platform Encountered at the Luttelgeest-01 Well, Noordoostpolder, The Netherlands. *Master of Science Thesis,* Utrecht University: 74.

Van Oversteeg, K., Lipsey, L.C., Pluymaekers, M., van Wees, J.D., Fokker, P.A. & Spiers, C.J., 2014. Fracture Permeability Assessment in Deeply Buried Carbonates and Implications for Enhanced Geothermal Systems: Inferences from a Detailed Well Study at Luttelgeest-01, The Netherlands. *Proceedings: Thirty-Eighth Workshop on Geothermal Reservoir Engineering*, February 24-26, Stanford University, Stanford, California.

Voss, C.I., Simmons, C.T. & Robinson, N.I., 2010. Three-dimensional benchmark for variable-density flow and transport simulation: matching semi-analytic stability modes for steady unstable convection in an inclined porous box. *Hydrogeology Journal* 18: 5-23.

Weatherill, D., Simmons, C.T., Voss, C.I. & Robinson, N.I., 2004. Testing density-dependent groundwater models: two0dimensional steady state unstable convection in infinite, finite and inclined porous layers. *Advanced in Water Resources* 27: 547-562.

Wibberley, C. A., Yielding, G. & Di Toro, G., 2008. Recent advances in the understanding of fault zone internal structure: a review. *Geological Society of London*, *Special Publications* 299: 5-33.

Yang, J., Latychev, K. and Edwards, R.N., 1998. Numerical computation of hydrothermal fluid convection in fractured Earth Structures. *Geophys. J. Int.* 135: 627-649.

Zhao, C., Hobbs, B.E., Peng, S., Muhlhaus, Ord, A. and Lin, G., 2003. Convective instability of 3-D fluid saturated geological fault zones heated from below. *Geophys. J. Int.* 155: 213-220.

Zhao, C., Hobbs, B.E., Peng, S., Muhlhaus, H.B., Liu, L., 2004. Theoretical investigation of convective instability in inclined and fluid-saturated three-dimensional fault zones. *Tectonophysics* 387: 47-64.

Zhao, C., Hobbs, B.E., Ord, A., Kuhn, M., Muhlhaus, H.B., Peng, S., 2006. Numerical simulation of double-diffusion driven convective flow and rock alteration in three-dimensional fluid saturated geological fault zones. *Comput. Methods Appl. Mech. Engrg.* 195: 2816-2840.

APPENDIX I – SYMBOLS USED

Symbol	Name	Unit
Ra	Rayleigh number	----
Ra*	Critical Rayleigh number	----
k	Permeability	m^2 or mD
ξ	Permeability anisotropy ratio	----
k^v	Vertical permeability	m^2 or mD
k^h	Horizontal permeability	m^2 or mD
α	Volumetric thermal expansion coefficient	$°C^{-1}$
ρ	Density	kg m^{-3}
C_p	Specific heat capacity	J kg^{-1} K^{-1}
g	Gravitational acceleration	m s^{-1}
H	Total thickness of the aquifer	m
ΔT	Temperature difference between top and bottom of layer	°C or K
μ	Dynamic viscosity	kg m^{-1} s^{-1}
λ	Conductivity	W m^{-1} K
a	Aspect ratio	----
L	Convection cell width	m
q	Heat flow	W m^{-2}
$λ_e$	Effective conductivity	W m^{-1} K
$λ_L$	Conductivity of pore fluid	W m^{-1} K
$λ_S$	Conductivity of rock mass	W m^{-1} K
u	Fluid velocity	m s^{-1}
P	Pressure	Pa
ϕ	Porosity	----
k_{min}	Minimum permeability for convection	m^2 or mD
t	Simulation time	yrs
κ	Diffusivity	m^2 s^{-1}
L	Diffusion length	m
τ	Characteristic time interval	s